Metabolic and non-metabolic roles of PHGDH and their impact on T cell function

Inauguraldissertation

zur

Erlangung der Würde eines Doktors der Philosophie

vorgelegt der

Philosophisch-Naturwissenschaftlichen Fakultät

der Universität Basel

von

Jordan Löliger

aus Riehen, Basel-Stadt

Basel, 2020

Genehmigt von der Philosophisch-Naturwissenschaftlichen Fakultät

auf Antrag von

Prof. Dr. Christoph Hess

Prof. Dr. Stephan Krähenbühl

Prof. Dr. Oliver Mühlemann

Basel, den 13. Oktober 2020

Prof. Dr. Martin Spiess
Dekan

Table of Contents

1. ABSTRACT

Cell-intrinsic metabolism underpins T cell differentiation and function. Metabolic enzymes can, however, also engage in non-metabolic (moonlighting) roles – which creates potential for functional incompatibilities. For the rate limiting enzyme in serine synthesis, PHGDH, we here describe a paradigm of such an incompatibility, demonstrating how, and at what price, metabolic function is traded off to block moonlighting during CD8⁺ T cell differentiation.

Complete serine restriction of CD8⁺ T cells triggered an extensive stress response orchestrated by a coordination of p53 and Myc – highlighting the importance of serine for T cells. Surprisingly therefore, PHGDH was only expressed in naïve but not memory CD8⁺ T cells, causing memory-selective serine auxotrophy and immunodeficiency in serine deplete hosts. Silencing of PHGDH was, however, a requirement for a normal naïve to memory transition to occur and, more broadly, a hallmark of differentiation across immune and non-immune cell lineages. Specific mutations in PHGDH, such as R163Q, are linked to differentiation-abnormalities and yet the R163Q variant showed near-normal enzymatic activity. This triggered a search for PHGDH moonlighting features, which identified PHGDH as RNA-binding protein (RBP) with affinity for cell-fate determining transcripts.

Our data establish a trade-off between metabolic activity and moonlighting of PHGDH in differentiating T cells, highlighting the integrated evolution of complex cellular processes and expanding the conceptual framework when interpreting cellular metabolic phenotypes.

Graphical abstract

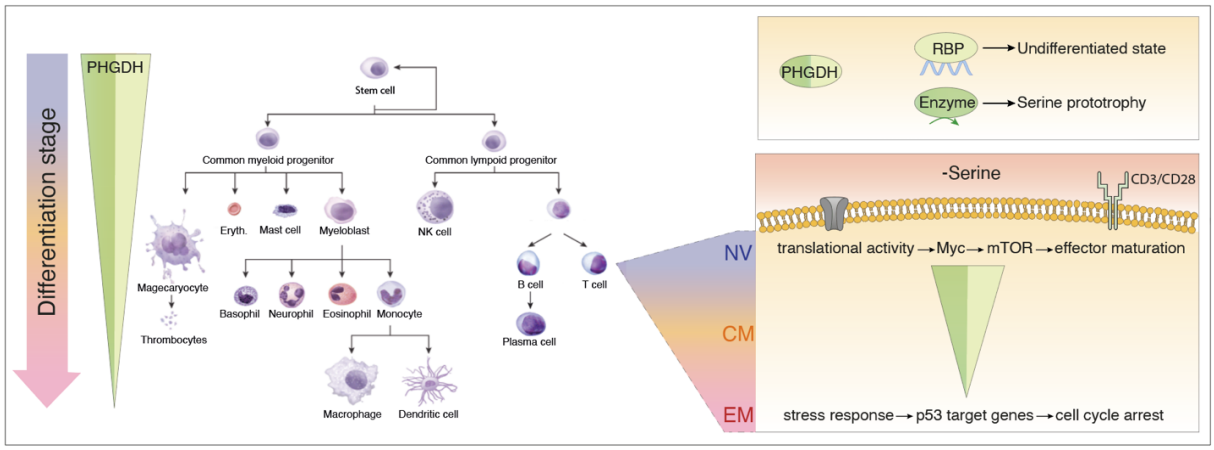

2. ABBREVIATIONS

Abbreviation	Full name
3PG	3-Phosphoglycerate
αKG	α-Ketoglutarate
AA	Amino acid
ANOVA	Analysis of variance
ARE	Adenine-uridine-rich elements
ARE-BPs	ARE binding protein
ATACseq	Assay for Transposase-Accessible Chromatin using sequencing
ATP	Adenosine tri-phosphate
ATRA	All-trans-retinoic acid
C13-glucose	Uniformly labeled carbon 13 glucose
Cas9	CRISPR associated protein 9
CD	Cluster of differentiation
CFSE	Carboxyfluorescein succinimidyl ester
ChIPseq	Chromatin immunoprecipitation followed by sequencing
CHX	Cycloheximide
CIRSPR	Clustered regularly interspaced short palindromic repeats
CpG	Cytosine-phosphate-guanine
DAPI	4′,6-Diamidino-2-phenylindole
DEGs	Differentially expressed genes
DEPCs	Double-positive effector cells
dpi	Days post-infection
DREAM	Dimerization partner, RB-like, E2F and MYBL2 complex
DSB	Double-strand break
ECAR	Extracellular acidification rate
EECs	Early effector cells
EMSA	Electrophoretic mobility shift assay
ENCODE	Encyclopedia of DNA Elements
EV	Empty vector
FACS	Fluorescence activated cell sorting
FAM	Fluorescein amidites
FBS	Fetal bovine serum
FC	Fold change
FCCP	Carbonyl cyanide 4-(trifluoromethoxy)phenylhydrazone
FITC	Fluorescein isothiocyanate
FP	Fluorescent polarization
FSC	Forward scatter
GAPDH	Glyeraldehyde-3-phophate dehydrogenase
GFP	Green fluorescent protein
Glu, E	Glutamate
GLUT1	Glucose transporter 1
Gly, G	Glycine
GO	Gene ontology
gRNA	Guide RNA
GZMB	Granzyme B
HL-60 cells	Human Leukemia 60 cells
IFNγ	Interferon γ
IGV	Integrative Genomics Viewer
IL	Interleukin
ImmGen	Immunological Genome Project
Indel	Insertion and deletions
IP	Immunoprecipitation
KO	Knock-out
LC-MS/MS	Liquid chromatography with tandem mass spectrometry
LCMV	Lymphocytic choriomeningitis virus

LmOVA	Listeria monocytogenes strain expressing OVA
mAb	Monoclonal antibody
MACS	Magnetically assisted cell sorting
MFI	Mean fluorescence intensity
MID	Mean isotope distribution
MPEC	Memory precursor effector cells
mTHF	Methylated tetrahydrofolate
mTOR	Mammalian target of rapamycin
NAD^+	oxidized NADH
NADH	Dihydronicotinamide adenine dinucleotide
NBDG	[N-(7-nitrobenz-2-oxa-1,3-diazol-4-yl) amino]-2-deoxy-D-glucose
NLS	Neu-Laxova syndrome
OCR	Oxygen consumption rate
OE	Overexpression
OVA	Ovalbumin
OVA-TET	OVA-tetramer
P	Phosphate
P-Pyr	Phosphohydroxypyruvate
P-Serine	Phosphoserine
PAM	Protospacer adjacent motif
PBMC	Peripheral blood mononuclear cells
PBS	Phosphate buffered saline
PHGDH	Phosphoglycerate dehydrogenase
PMA	Phorbol 12-myristate 13-acetate
PSAT1	Phosphoserine aminotransferase 1
PSPH	Phosphoserine phosphatase
PTC	Premature termination codon
PTM	Post-translational modifications
RBP	RNA-binding protein
RIP	RNA immunoprecipitation
RIPseq	RNA immunoprecipitation sequencing
RIPA buffer	Radioimmunoprecipitation assay buffer
RNAseq	RNA sequencing
RNP	Ribonucleoprotein
RPMI	Roswell Park Memorial Institute media
RT	Room temperature
SD	Standard deviation
SEM	Standard error of the mean
Ser, S	Serine
SHMT1/2	Serine hydroxymethyltransferase 1/2
SLC1A4/5	Solute carrier family 1 member 4/5
SLEC	Short-lived effector cell
SPF	Specific pathogen free
SSC	Side scatter
SSP	Serine synthesis pathway
T_{CM}, CM	Central memory $CD8^+$ T cells
T_{EM}, EM	Effector-memory $CD8^+$ T cells
T_{NV}, NV	Naïve $CD8^+$ T cells
T_{RM}, RM	Tissue-resident memory
T_{SCM}, SCM	Stem cell memory $CD8^+$ T cells
TCR	T cell receptor
THF	Tetrahydrofolate
THP-1 cells	Tohoku Hospital Pediatrics-1 cells
TNF	Tumor necrosis factor
UTR	Untranslated region
UV	Ultraviolet
WT	Wildtype

3. INTRODUCTION

3.1 T cell immunology

During T cell development in the thymus, genetic recombination of the T cell receptor (TCR) gene generates an incredibly diverse T cell repertoire (Qi et al., 2014). As a consequence, the frequencies and absolute numbers of T cells specific for an individual antigen are low, but the diversity of the TCR repertoire allows recognition of approximately 10^7 epitopes (Arstila et al., 1999). Traditionally, the course of a T cell response induced by antigen recognition is divided into the three discrete phases – expansion, contraction, and subsequent memory formation (Sallusto et al., 2010). In brief, during acute infection, a small amount of naïve pathogen-specific $CD8^+$ T (T_{NV}) cells are primed in lymph nodes, expand clonally, and differentiate into primary effector cells (Harty and Badovinac, 2008; Zhang and Bevan, 2011). These effector cells then leave the lymph node, enter the bloodstream and migrate to sites of inflammation, where they secrete cytokines and kill infected cells. Once the pathogen is cleared, the majority of effector cells undergoes apoptosis during contraction, whereas a small proportion of pathogen-specific $CD8^+$ T cells differentiates to form the memory population (Farber et al., 2014; Obar and Lefrançois, 2010). A defining feature of memory T cells is their longevity and their capacity to re-expand the pool of effector cells (secondary effector cells) more rapidly than their naïve counterparts – enabling them to contain re-infection with increased efficacy (Weng et al., 2012). Reflecting the organization of the recall response, various subsets of memory T cells exist, which differ in regard to migration pattern and tissue distribution, phenotype and functional properties. Human central memory (T_{CM}) $CD8^+$ T cells re-circulate between the blood stream and lymph nodes, whereas effector memory (T_{EM}) $CD8^+$ T cells home into distinct peripheral tissue sites from peripheral blood (Chang et al., 2014; Farber et al., 2014; Jameson and Masopust, 2018). Since both memory subsets are circulating and thereby readily accessible from peripheral blood donations, these are the most studied human memory subsets and were also the focus of my thesis. Still, it is important to appreciate that these two memory subsets only represent a small fraction of all memory T cells distributed throughout the body. In the last years, new memory subsets have been described and delineated, including stem cell memory T (T_{SCM}) cells and tissue-resident memory T (T_{RM}) cells (Jameson and Masopust, 2018; Lugli et al., 2011). Due to technical challenges in determining relationships amongst human T cell subsets, a number of lineage relationship models have been proposed. One of the most widely accepted models, the linear differentiation model, places T_{NV}, T_{SCM}, T_{CM} and T_{EM} cells in a differentiation hierarchy, in which these cells function as precursors for effector T cells (Figure I1A). According to this model, gene expression and

epigenetic patterns show gradual alterations from one subset to the next in a hierarchal manner (Farber et al., 2014). Through exposition to diverse pathogens and commensal microorganisms via the skin, aerodigestive tract and genital mucosa, the frequency of memory T cells increases as a function of age (Figure I1B). A fascinating aspect of the immune system is the ability of lymphocytes to sense and maintain their numbers in a certain range (Takada and Jameson, 2009). Therefore, it is assumed that the percental increase of memory T cells during ageing is due to a loss of T_{NV} cells as a result of decreased thymic output (Sallusto et al., 2010). On the other hand, it is not known whether the immune system senses total numbers of T cells or whether naïve and memory T cell numbers are regulated independently. The majority of our current understanding of memory T cell generation, function and maintenance is based on results from mouse models (Farber et al., 2014). These animal models have various advantages, such as the additional accessibility of tissue resident memory T cell subsets, the possibility of genetic manipulations, adoptive transfer models etc. However, since the lifespan of a laboratory mouse is restricted to 2-3 years, most immunological mouse memory studies are in a timeframe of several months, including rarely more than two infections. Therefore, mouse models cannot recapitulate multiple pathogen exposures over an extended period of time. Additionally, most experimental mice are maintained in specific pathogen-free (SPF) conditions further limiting the breadth of their commensal diversity. Therefore, the generation and maintenance of human memory T cells differs significantly from mouse memory T cells. Due to these potential discrepancies, one of the aims of my host laboratory is to start projects based on findings in human T cells and eventually translate them into an *in vivo* setting, an approach also taken for this project.

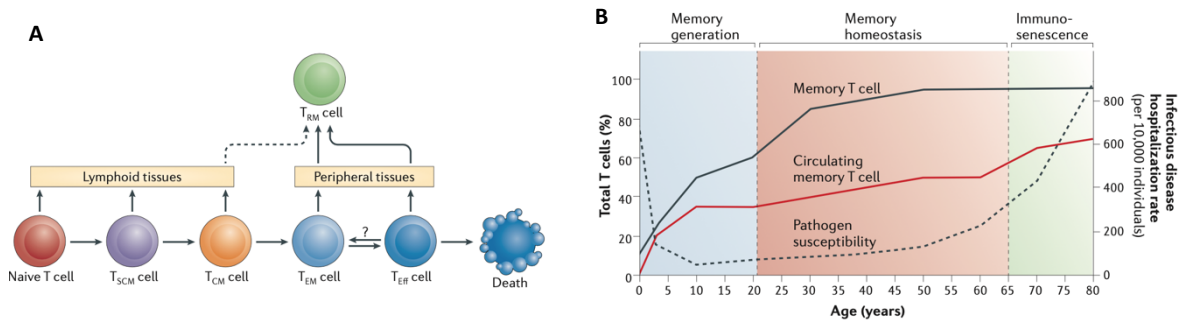

Figure I1. T cell differentiation and generation of human memory T cell subsets.
(**A**) The linear differentiation model: The progressive differentiation from naïve T cells (T_{NV}) into stem cell memory T (T_{SCM}) cells, central memory T (T_{CM}) cells, effector memory T (T_{EM}) and resident memory T (T_{RM}) cells is illustrated. (**B**) Memory T cell frequency, pathogen susceptibility and mortality throughout human life. The frequency of overall memory T cells inversely correlates with susceptibility to pathogen infection. Reprinted from Farber et al., 2014.

3.2 The gene expression pathway in T cells

Phenotypic and functional properties of T cell subsets are ultimately determined by the abundance and composition of proteins, the final products of gene expression (Figure I2). Since neither mRNAs nor proteins are really 'expressed' but rather represent intermediates of a 'gene expression pathway', I adapted this term from a recent review article (Buccitelli and Selbach, 2020). At the beginning of the gene expression pathway is the genotype, the complement of DNA possessed by an organism, where every gene is saved as two copies (two alleles) in the nucleus. Transcription of a specific gene depends on the accessibility to, and the availability of, transcription factors and results in the formation of mRNA transcripts. Then, translation of mRNAs into proteins by ribosomes results in a vast amount of protein molecules exceeding the dynamic range of mRNA by several orders of magnitude. As an example relevant for immunologists, quiescent human T_{NV} cells contain around 77'000 mRNA molecules but up to 410 million proteins, resulting in an average mRNA to protein ratio of 1 to 5'400 (Wolf et al., 2020). Therefore, one of the results of the gene expression pathway is a remarkable amplification of a signal from two copies of a gene to several thousand transcripts to several million copies of a specific protein. Additionally, the signal is diversified by alternative splicing creating a range of unique proteins from the same mRNA (Fu and Ares, 2014). Unsurprisingly, this hierarchical pathway is a very complex process that is regulated at various levels (illustrated in the boxes at the bottom of Figure I2). In particular, regulation at the post-transactional level can lead to surprising relationships between mRNA and protein abundance. With the rise of the 'omics' technologies, various genome wide studies, including our initial RNA-sequencing (RNAseq) and proteomics experiments, revealed that mRNA and protein abundance do not always follow a linear correlation. Such findings are subject to intense discussions and advanced our understanding of gene expression control and the 'central dogma of molecular biology'. One such published example of diverging mRNA-protein abundance, stems from experiments performed in human T_{NV} cells (Wolf et al., 2020). By

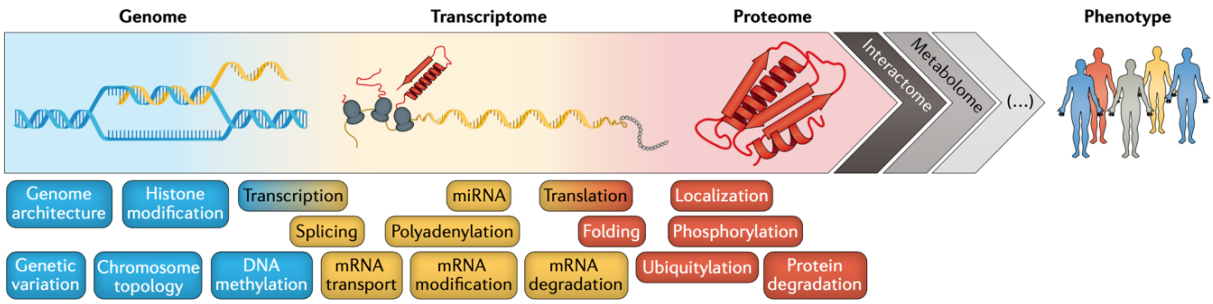

Figure I2. Overview of the gene expression pathway.
Overview of the steps of the gene expression pathway connecting phenotype to genotype. Key regulatory nodes are indicated at the bottom. Reprinted from Buccitelli and Selbach, 2020.

performing RNAseq, a specific set of 242 mRNA species was found to be substantially expressed, while proteomics of the same cells did not reveal any protein derived from these mRNAs. Interestingly, upon T cell activation, the translational repression of these mRNA molecules was alleviated leading to a rapid increase of respective proteins. Another intriguing observation of this study was the overall dynamics of protein synthesis upon activation. Whereas quiescent T_{NV} cells synthesized ~60'000 proteins per min, 6h activated cells produced ~300'000 proteins per min, representing a 5-fold increase in ribosomal output. Intriguingly, the total number of mRNAs only increased 1.4-fold from 77'000 to 105'000 transcripts. This indicates that post-transcriptional regulation plays a major role in driving the increase of overall protein output upon T cell activation. Such post-transcriptional processes include changes in mRNA stability, translation efficiency and protein stability (the factors dictating protein abundance are summarized in Figure I3).

Proteins, their interaction with other proteins and/or other biomolecules (such as RNA) and in the case of metabolic enzymes, their catalytic activity, give rise to phenotypes, also of T cells. Since proteins are the final result of the gene expression pathway, any changes along the way ultimately are responsible for differences in phenotype and function of T cell subsets, with post-transcriptional events emerging as key regulators of T cell biology.

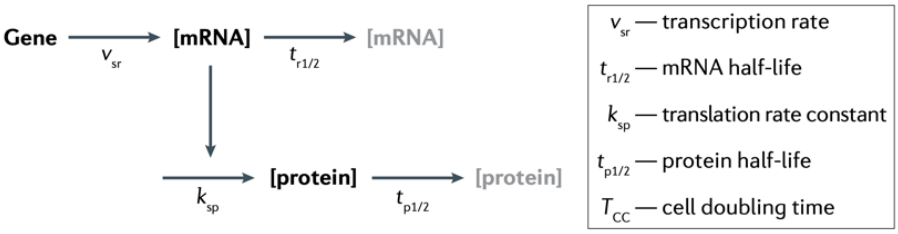

Figure I3. Determinants of protein abundance.
Protein abundance depends on four factors: Transcription rate (v_{sr}), mRNA half-live ($t_{r1/2}$), translation rate (k_{sp}) and protein half-live ($t_{p1/2}$). The first two factors jointly define mRNA levels. Post-transcriptional mechanisms can impact several factors. In dividing cells the cell cycle time (T_{cc}) is also an important factor influencing protein abundance, in particular for long-lived proteins. Reprinted from Buccitelli and Selbach, 2020.

3.3 RNA-binding proteins regulating the gene expression pathway

RNA-binding proteins (RBPs) play an important role in post-transcriptional regulation by determining various aspects of the life of an RNA molecule (Hentze et al., 2018). RBPs constantly decorate mRNA molecules and thereby control processes such as splicing, cleavage and polyadenylation, as well as editing, localization, stability and translation of mRNAs. Additionally, some recent findings also indicate the surprising association of specific RBPs with DNA (Nostrand et al., 2020). The interaction between RBPs and RNA can occur via several binding modes and can lead to various consequences for the RNA (summarized in Figure I4). Furthermore, these interactions undergo signal-dependent alterations, which allow a flexible regulation and make them responsive to external stimuli (Salerno et al., 2020). Such signals can lead to dynamic remodeling of RBP-RNA complexes by affecting post-translational modifications (PTMs) of RBPs, biochemical modifications of RNA (defining the epitranscriptome) or by influencing the activity of ATP-dependent RNA helicases (Kilchert et al., 2019; Salerno et al., 2020). For T_{EM} cells it has been shown, that RBPs preserve a quiescent state by preventing the production of effector proteins via post-transcriptional regulation (Salerno et al., 2018). However, upon TCR ligation and hence T cell activation, the RNA-interactome remodels and certain RBPs mediate stabilization and promote translation of cytokine mRNAs, thereby impacting the magnitude and kinetics of an effector response. Methods to identify the repertoires of RBPs are rapidly evolving, but are mainly based on the first two RNA-interactome capture studies published (Baltz et al., 2012; Castello et al., 2012). These proteome-wide approaches are based on ultraviolet (UV) light induced crosslinking of RNA and protein, combined with mass spectrometric analyses to identify the RBP repertoire. Interestingly, in these screens, metabolic enzymes have been recurrently found to bind RNA and have been validated by orthogonal approaches (Figure I4H shows a prominent example). A recent meta-analysis reports 71 metabolic enzymes binding RNA in humans, 104 in mouse and 132 in yeast RNA-interactomes (Hentze et al., 2018). Interestingly, although these enzymes belong to different metabolic pathways and catalyze distinct reactions, many of them bind either mono- or dinucleotides as co-factors (Castello et al., 2015). These metabolic enzyme, which have an alternative function – a moonlighting activity – as RBPs, seem to be a relatively frequent phenomenon, which is also widely conserved. However, the consequences of these interactions are only beginning to be elucidated. For a laboratory studying immunometabolism, such novel roles of metabolic enzymes open new roads, with the possibility of feedback loops and connections between metabolism, control of gene expression and ultimately immune function (Hentze and Preiss, 2010).

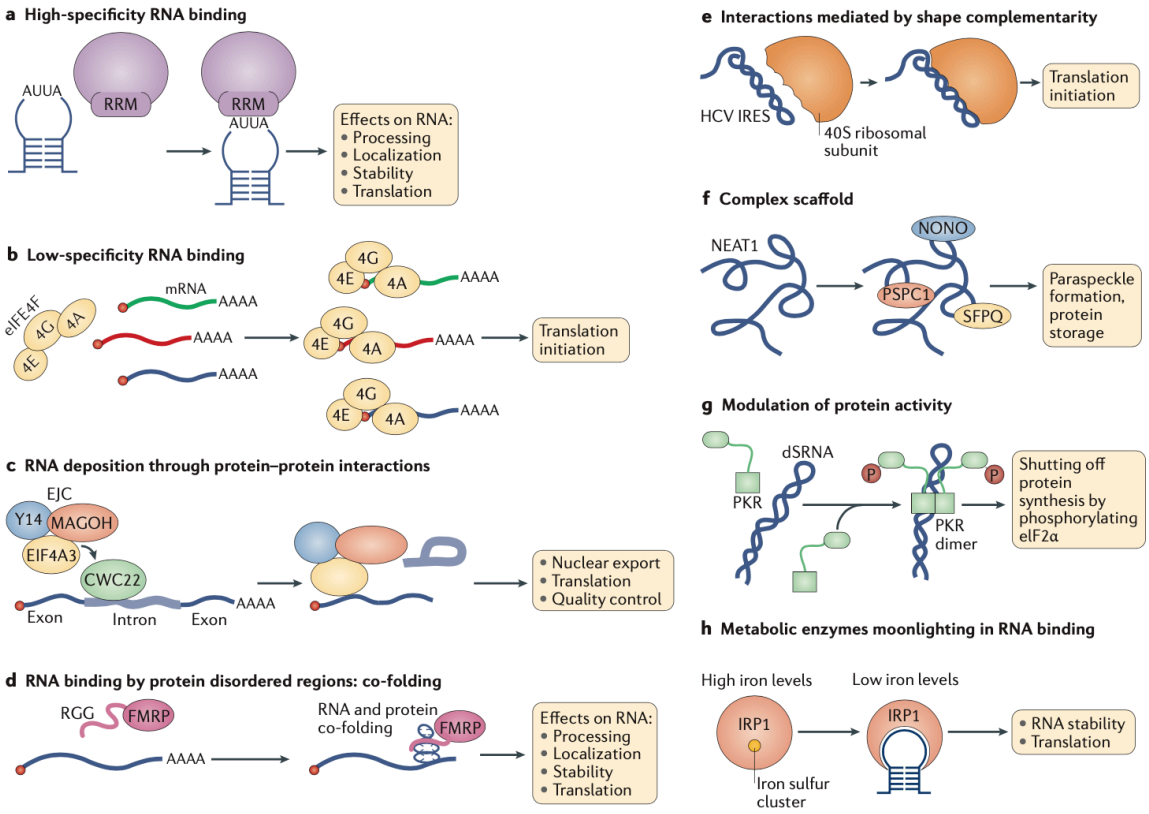

Figure I4. Modes and effects of RNA binding by RBPs.
(**A**) An RNA-binding protein (RBP) harboring a classic RNA-binding domain such as the RNA recognition motif (RRM) can interact with high specificity to specific RNA sequences in the context of a stem–loop. (**B**) The eukaryotic translation initiation factor 4F (eIF4F) complex is composed of the cap-binding proteins eIF4E (4E) and eIF4G (4G) and the helicase eIF4A (4A). This complex associates with capped RNA in a sequence-independent manner to enable translation initiation. (**C**) The exon junction complex (EJC) is deposited nonselectively on nascent transcripts by its interaction with the splicing factor CWC22 about 20 nucleotides upstream of the exon-exon junction, immediately following intron removal. (**D**) The intrinsically disordered Arg-Gly-Gly (RGG) repeat motif of fragile X mental retardation protein (FMRP) co-folds with its target RNA, forming a tight electrostatic and shape-complementation-driven interaction. (**E**) The internal ribosome entry site (IRES) of hepatitis C virus (HCV) interacts directly with the ribosome through a complex interaction mode that involves shape complementarity between the IRES and the 40S ribosome subunit. (**F**) The long non-coding RNA NEAT1 sequesters the RBPs NONO, PSPC1 and SFPQ to form paraspeckles. (**G**) Interferon-induced, double-stranded RNA-activated protein kinase (PKR) binds to double-stranded RNA (dsRNA) derived from viral replication. Binding RNA promotes PKR dimerization, autophosphorylation and activation. Active PKR phosphorylates eIF2α to block protein synthesis in infected cells. (**H**) Iron-regulatory protein 1 (IRP1) associates with an iron-sulfur cluster to catalyze the interconversion between citrate and isocitrate. In conditions of low iron levels, the iron–sulfur cluster is no longer synthesized and IRP1 binds mRNAs that encode cellular factors involved in iron homeostasis, thereby regulating their fate. Reprinted figure and adapted figure-ledged from Hentze et al., 2018.

3.4 Metabolism regulating the gene expression pathway

Activation, proliferation and differentiation of T cells is accompanied by changes in cellular metabolism. This so called metabolic reprogramming, is thought to be an adaptation to changing metabolic demands allowing T cells to meet their bioenergetic and biosynthetic needs (Maciver et al., 2013; Olenchock et al., 2017). However, over the last decade, our understanding of intermediary metabolism has advanced significantly. Initially considered to be restricted to these 'housekeeping' functions (supply of energy and molecular building blocks), growing evidence indicates close connections between metabolism and the regulation of the gene expression pathway and signaling pathways. Specifically in T cells, metabolic and non-metabolic functions of enzymes are becoming increasingly apparent, as their involvement has been shown in chromatin remodeling, modulation of TCR-signaling and regulation of mRNA translation (Chang et al., 2013; Chapman et al., 2019; Gubser et al., 2013; Phan et al., 2017). Therefore, intermediary metabolism emerges as a *bona fide* regulatory system influencing immune cell functionality and cell fate (Jung et al., 2019; Man and Kallies, 2015) (summarized in Figure I5). Additionally, this leaves room for discussions about the purpose of activation induced metabolic reprogramming – especially if enzymes are involved, which engage in metabolic as well as non-metabolic roles.

When differentiating from a naïve to a memory state, T cells engage in distinct metabolic pathways (Buck et al., 2016; Gubser et al., 2013; O'Sullivan et al., 2014; van der Windt et al., 2012). Given the fundamental role of metabolism in governing immune cell functionality and fate, we set out to investigate human $CD8^+$ T_{NV} and T_{EM} cells at the transcriptome and proteome level focusing on intermediary metabolism. This approach identified metabolic restriction as unexpected signature of memory cell differentiation. As part of this signature, silencing of phosphoglycerate dehydrogenase (PHGDH), the rate limiting enzyme of the serine synthesis pathway, represented the most profound memory-specific pruning event. Loss of PHGDH emerged as trade-off between priorities of metabolic and non-metabolic roles of the enzyme in memory T cells, and as a hallmark of differentiation across immune- as well as non-immune cell lineages.

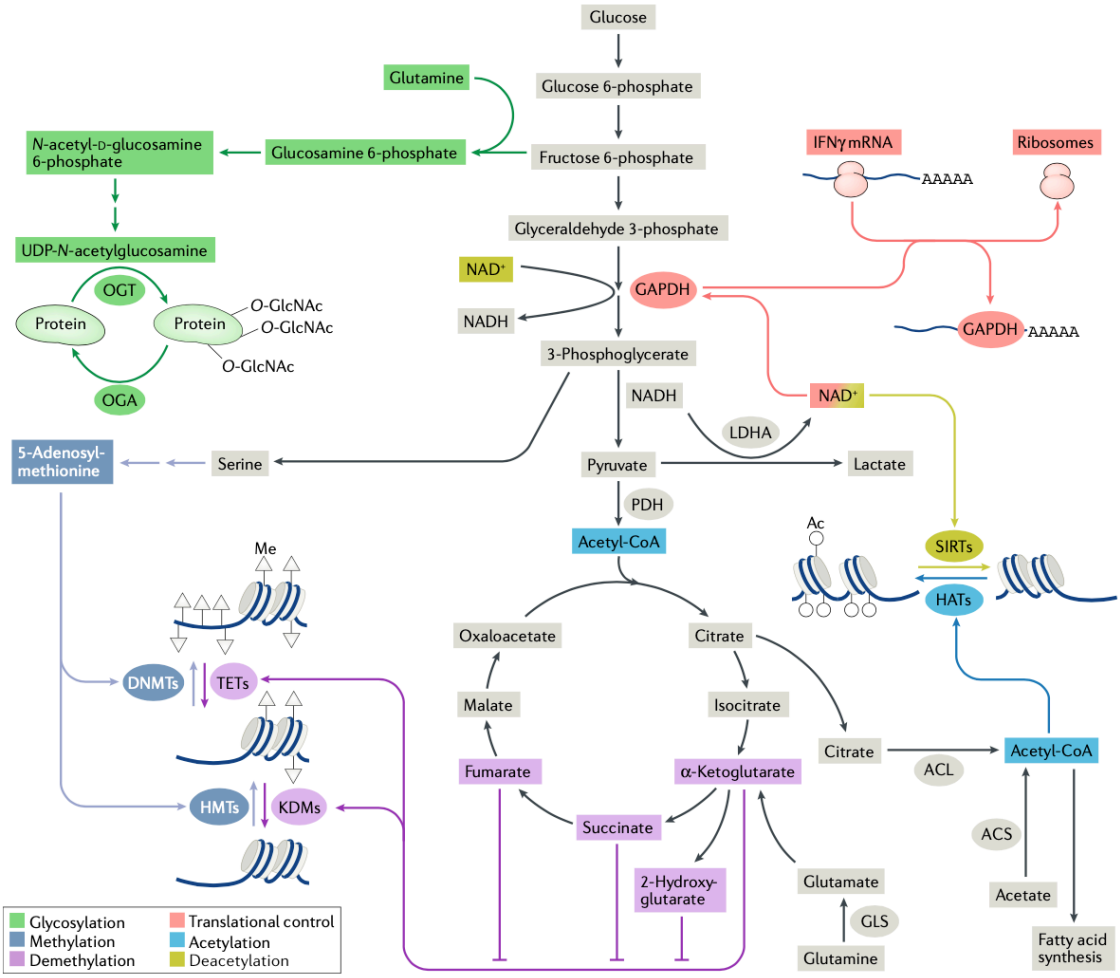

Figure I5. Metabolic determinants of immune cell differentiation and function.
Metabolites can have profound effects on the transcription, translation, and function of proteins in immune cells. Post-translational glycosylation of cellular proteins alters protein function and is dependent on metabolites from the hexosamine pathway (upper left). The availability of metabolites that are used as substrates for enzymes such as glyceraldehyde 3-phosphate dehydrogenase (GAPDH) or l-lactate dehydrogenase A chain (LDHA) can dictate the extent to which these enzymes can control key translation events involved in immune cell function (upper right). Metabolites related to α-ketoglutarate are important in the function of demethylases that target either histones (lysine demethylases (KDMs)) or DNA (ten-eleven translocation family members (TETs)); these demethylases oppose the actions of histone methyltransferases (HMTs) and DNA methyltransferases (DNMTs), which are themselves regulated by metabolites of the one-carbon pathway (lower left). Acetylation of cellular proteins - especially histones - is dependent on NAD^+ availability for the deacetylase function of the sirtuin (SIRT) family enzymes, whereas acetylation reactions themselves are dependent on intracellular supply of acetyl-CoA generated through a range of distinct pathways (lower right). ACL, ATP citrate lyase; ACS, acetyl-CoA synthetase; GlcNAc, *N*-acetylglucosamine; GLS, glutaminase; HATs, histone acetyltransferases; IFNγ, interferon-γ; Me, methyl; OGA, protein *O*-GlcNAcase; OGT, UDP-*N*-acetylglucosamine-peptide *N*-acetylglucosaminyltransferase; PDH, pyruvate dehydrogenase. Reprinted figure including figure ledged from Patel et al., 2019.

4. RESULTS

4.1 Reduced metabolic breadth distinguishes memory from naïve CD8+ T cells at the transcriptome and proteome level

In order to broadly compare metabolic programs between CD8+ T_{NV} and T_{EM} cells, differential abundance of gene transcripts and proteins was analyzed by RNAseq and proteomics, using sorted human T cells as input material (Figure 1A,B). Gene ontology (GO) terms overrepresented in the analysis of proteins differentially upregulated in CD8+ T_{EM} included 'antigen processing and presentation', 'T cell mediated cytotoxicity' and 'cell activation' – aligning with features associated with CD8+ T_{EM} cells (Figure S1A). Unexpectedly, many variants of the term containing 'metabolic process' were driven by proteins downregulated in T_{EM} cells. 'Cellular metabolic process' was also the most significantly enriched term when performing GO term analysis on transcripts significantly reduced in CD8+ T_{EM} *vs.* T_{NV} cells. Inspecting individual transcripts and proteins, PHGDH was one of the most profoundly downregulated metabolic transcripts in T_{EM} cells, and one of the most differentially expressed proteins overall (Figure 1A,B). Differential expression of PHGDH between CD8+ T_{EM} and T_{NV} was confirmed by Western blotting, which in addition established low abundance of PHGDH also in T_{CM} cells (Figure 1C). Of the other two enzymes of the serine synthesis pathway (SSP) (illustrated in Figure 1D), PSAT1 was differentially expressed on RNA and protein level (proteomics) as well, whereas comparable transcript abundance of PSPH was observed. In agreement with our data, transcriptome and proteome data from the public domain also listed PHGDH as 'downregulated in memory T cells' (van Aalderen et al., 2017; Yang et al., 2016). Thus, contrary to our hypothesis, metabolic pruning rather than increased metabolic flexibility, was the transcriptional/proteomic signature distinguishing CD8+ T_{EM} from T_{NV} cells, with reduced abundance of PHGDH emerging as one of the most profound metabolic restrictions among CD8+ T_{EM} cells.

Naïve murine T cells induce the components of the SSP upon activation, *i.e.* among primary effector cells (Ma et al., 2017). This led us to test whether also in secondary effector cells, *i.e.* those derived from CD8+ T_{CM} and T_{EM} cells, expression of PHGDH, PSAT1 and PSPH was increased upon activation. Following stimulation with anti-CD3/CD28 monoclonal antibodies (mAb), only a slight induction of PHGDH was detected in T_{EM} cells (Figure 1E). In T_{NV} cells, abundance of PHGDH increased further – as previously shown in their murine counterparts (Ma et al., 2017) – while in T_{CM} cells PHGDH reached levels in between T_{NV} and T_{EM} cells (Figure 1E). PSAT1 and PSPH were similarly induced in all three T cell subsets. Of interest, an inverse pattern of protein expression was detected for the two major serine transporters –

SLC1A4 and SLC1A5 – with strong induction in CD8⁺ T_{CM} and T_{EM} cells and only moderate upregulation in T_{NV} cells. Notably, SLC1A4 and SLC1A5 transcripts were more abundant in CD8⁺ T_{EM} than in T_{NV} cells also under non-activated conditions (Figure 1A), whereas no protein was detected by Western blotting as well as by proteomics in these quiescent cells – suggesting regulation at the post-transcriptional, translational or post-translational level. No subset specific differences were observed for the serine catabolizing enzyme SHMT, while an increase in the abundance of mitochondrial localized SHMT2 was accompanied by a decrease in the cytosolic isoform SHMT1 – pointing towards compartmentalization of the one carbon cycle in human CD8⁺ T cells, as has previously been described for murine CD4⁺ T cells (Ron-Harel et al., 2016).

To functionally test the SSP in CD8⁺ T cells, metabolic tracing was utilized. In T_{EM} cells, no heavy serine nor glycine derived from C13-glucose was detected, while in T_{CM} cells no serine was derived from heavy glucose, but 1-2% of the total glycine pool (Figure 1F). This data aligned with the expression pattern of PHGDH identified in these cells and suggest their dependency on extracellular serine. In activated T_{NV} cells, m+3 labeled serine from C13-glucose was detected, albeit fueling only around 3.5% of their total serine pool (Figure 1F) – despite abundant expression of the SSP enzymes (Figure 1E). Of note, PHGDH protein expression did steadily increase in T_{NV} cells after activation, whereas longitudinal tracing demonstrated steady-state labeling already at 6h post-activation (Figure S1B). This suggested that induction of PHGDH in activated CD8⁺ T_{NV} cells was not driven by the requirement to produce more serine from glucose. Comparable consumption of serine in the culture media of activated, expanding CD8⁺ T_{NV} and T_{EM} cells further supported the notion of a bias towards uptake of free serine over *de novo* synthesis by T_{NV} cells (Figure 1G and Figure S1C). Indeed, after glutamine, serine was the second-most highly consumed amino acid (AA) in both subsets, also highlighting its importance as an anabolic substrate (Figure S1D). In general, AA consumption and excretion patterns were similar in CD8⁺ T_{NV} and T_{EM} cells, closely mirroring AA requirements published for other proliferating cells (Hosios et al., 2016). The SSP is induced by the transcription factor Myc in other cell systems (Sun et al., 2015), and Interleukin-15 (IL-15) is known to drive Myc expression in T cells (Preston et al., 2015). We therefore tested whether also in CD8⁺ T_{EM} cells combining anti-CD3/CD28 mAb and cytokine stimulation is capable of inducing Myc and the SSP. While addition of IL-15 did result in an increase of Myc protein in effector cells derived from both T_{NV} and T_{EM} cells, only in primary effector cells (*i.e.* those derived from T_{NV} cells) concomitant SSP induction was observed (Figure S1E). Together, these biochemical and functional data established a selective and stable inability of CD8⁺ T_{EM} cells to generate serine, prompting us to investigate the epigenetic

landscape of PHGDH in T cells. In a genome wide analysis of histone methylation marks in human CD8$^+$ T cells, *PHGDH* is listed among the 'repressed genes' in T_{EM} cells compared to T_{NV}, decorated with low amounts of activating H3K4me3 and high amounts of silencing H3K27me3 (Araki et al., 2009). Assessing the open access Blueprint Epigenome database (blueprint-epigenome.eu) revealed a similar pattern with less activating and more repressing histone marks along the *PHGDH* gene of T_{EM} compared to T_{NV} cells (Figure S1F). We further explored public domain whole-genome bisulfite sequencing data from sorted human T cells (Abdelsamed et al., 2017). These analyses demonstrated an increased percentage of silencing methylated cytosines in the CpG island around the first intron of *PHGDH* (Figure S1G). Of note, when overlaying chromatin immunoprecipitation sequencing (ChIP-seq) clusters from the Encyclopedia of DNA Elements (ENCODE) project, several transcription factors – including Myc – were predicted to bind in the region with increased methylation in CD8$^+$ T_{EM} cells.

Together, these results identified selective silencing of the PHGDH protein expression in CD8$^+$ T_{EM} cells. This trait was maintained when re-stimulated to form secondary effectors, despite a high demand for serine upon activation. In CD8$^+$ T_{NV} cells PHGDH was expressed and involved in serine synthesis, however with a dissociation between PHGDH protein abundance and functional engagement in the SSP when extracellular serine was available.

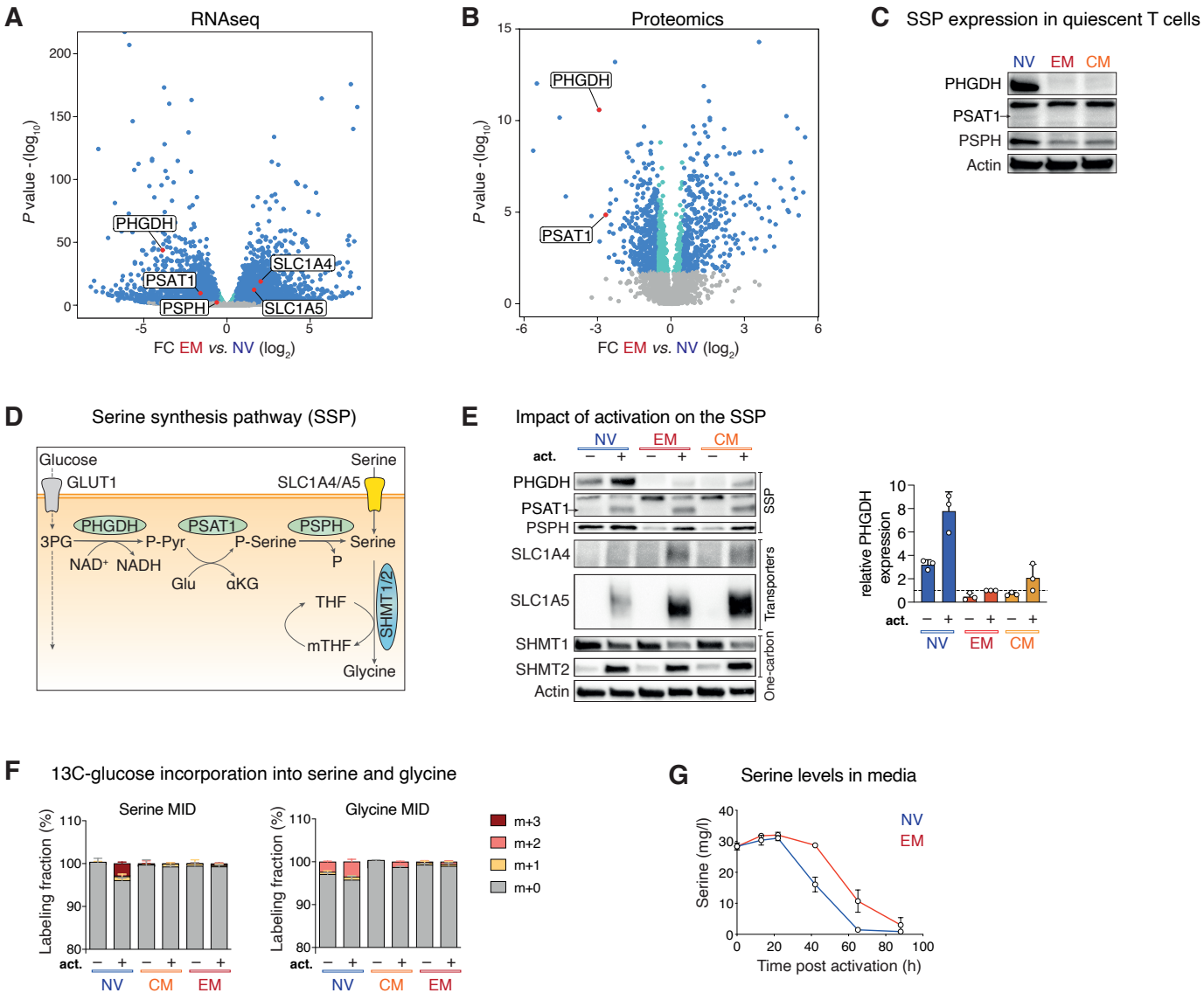

Figure 1. Silencing of PHGDH is a major metabolic restriction of memory CD8⁺ T cells.

Figure 1. Silencing of PHGDH is a major metabolic restriction of memory CD8+ T cells.

(**A** and **B**) Volcano plot of RNAseq- (A) and proteomics (B) analysis comparing T_{NV} and T_{EM} cells from healthy human donors (n=4 for each experiment). Genes/proteins related to serine metabolism are shown in red, if detected. Hits with $p_{adj}<0.05$ are marked in dark blue if $log_2FC>0.5$ or turquoise if $log_2FC<0.5$.

(**C**) Western blot depicting enzymes of the SSP in freshly sorted T_{NV}, T_{EM} and T_{CM} cells. Actin was used as a loading control. Data are representative of n=2 independent experiments.

(**D**) Schematic illustration of the SSP enzymes (green), serine permeable amino acid transporters (yellow) and enzymes representing the connection to one carbon metabolism (blue).

(**E**) Left: Representative Western blot visualization of proteins involved in serine metabolism among T_{NV}, T_{EM} and T_{CM} cells. T cells were left unstimulated (–) or activated with anti-CD3/CD28 mAb (+) coated beads for 24h prior to protein extraction. Right: Quantification of PHGDH protein abundance by densitometry, normalized against actin and represented relative to PHGDH abundance in activated T_{EM} cells of each respective donor (n=3 independent experiments).

(**F**) Mass isotopomer distribution (MID) of 13C-glucose derived serine and glycine in non-activated (–) and activated (+)T cell subsets (n=4 donors). C13-glucose was added to the cell culture media for a period of 6h. Fractional enrichment of m+1, m+2 and m+3 isotoplogues are shown for their respective metabolite pool. Data are normalized to cell number and corrected for natural abundance of carbon 13. The y-axis is cropped.

(**G**) Serine concentration in media measured by LC-MS/MS at different timepoints post-activation of T_{NV} and T_{EM} cells (n=4 donors).

All experiments were done with human primary cells. Data are represented as mean ± SD (**E**, **G**) or mean ± SEM (**F**). See also Figure S1.

3PG, 3-phophoglyerate; act., anti-CD3/CD28 mediated activation; αKG, α-ketoglutarate; anti-CD3/CD28 mediated activation; C13-glucose, uniformly labeled carbon 13 glucose; FC, fold change; Glu, Glutamate; GLUT1, glucose transporter 1; LC-MS/MS, liquid chromatography with tandem mass spectrometry; mAb, monoclonal antibody; MID, mass isotopomer distribution; mTHF, methylated tetrahydrofolate; NAD^+, oxidized NADH; NADH, dihydronicotinamide adenine dinucleotide; P, phosphate; p_{adj}, adjusted p-value; P-Pyr, phosphohydroxypyruvate; P-Serine, phosphoserine; PHGDH, phosphoglycerate dehydrogenase; PSAT1, phosphoserine aminotransferase 1; PSPH, phosphoserine phosphatase; RNAseq, RNA-sequencing; SEM, standard error of the mean; SD, standard deviation; SHMT1/2, serine hydroxymethyltransferase1/2; SLC1A4/5, solute carrier family 1 member 4/5; SSP, serine synthesis pathway; THF, tetrahydrofolate; T_{NV}/NV, naïve CD8+ T cells; T_{CM}/CM, central memory CD8+ T cells; T_{EM}/EM, effector memory CD8+ T cells.

4.2 Serine is essential for CD8$^+$ T cells to properly activate and proliferate

As CD8$^+$ T_{EM} cells lacked the capacity to generate endogenous serine, we went on to explore how availability of exogenous serine impacted T cell function. To do so, human CD8$^+$ T cells were sorted and activated in media containing 10% dialyzed fetal bovine serum (dFBS) ± serine, ± a small molecule inhibitor of PHGDH (schematically summarized in Figure 2A). In absence of serine, activated T_{NV} cells tended to further increase SSP expression, whereas T_{EM} cells did not adapt (Figure 2B,C). SHMT2 and SLC1A5 also failed to increase in T_{EM}, but not in T_{NV} cells, when no serine was available in the culture media (Figure 2B). Suggesting a broad deficit imposed by lack of exogenous serine, activated T_{EM} cells failed to blast, upregulate activation and metabolic markers (CD25, CD71, CD98), increase expression of glucose transporter 1 (GLUT1) and enhance glycolysis (Figure 2D, S2A-D). T_{NV} cells, on the other hand, were better able to grow and upregulate activation markers, as well as glycolysis, in absence of exogenous serine (Figure 2D, S2A-D). As expected, pharmacological inhibition of PHGDH had no effect on T_{EM} cells. Similarly, inhibition of PHGDH in T_{NV} cells in the presence of exogenous serine did not affect any of the above described features, further suggesting that human T_{NV} cells did not substantially engage in or depend on serine *de novo* synthesis when extracellular serine was available. Combining serine deprivation with pharmacological inhibition of PHGDH, however, blunted activation and metabolic reprogramming also in T_{NV} cells. At 5 days post-activation, changes in media color – *i.e.* acidification – aligned with the activation pattern described above (Figure 2E). Fitting their PHGDH expression status, T_{CM} cells showed a phenotype intermediate between T_{NV} and T_{EM} cells (Figure 2B-E and Figure S2A-D). Given that CD8$^+$ T_{CM} and T_{EM} cells required extracellular serine for metabolic reprogramming upon activation, we reasoned that serine might also selectively affect their capacity to proliferate. Indeed, in absence of serine both activated T_{CM} and T_{EM} failed to proliferate, whereas proliferation of T_{NV} cells was only moderately affected (Figure 2F). Additionally, surface expression of CD107a – a marker of degranulation – was significantly lower in T_{EM} cells activated under serine depleted *vs.* replete conditions (Figure S2E). Secretion of various cytokines was likewise reduced when memory T cells were activated in absence of exogenous serine (data not shown). Importantly, none of the culture conditions used in these series of experiments affected cell viability at the 24h post-activation timepoint (Figure S2F).

In all, these data identified (i) serine as an indispensable AA for CD8$^+$ T cell activation, metabolic reprogramming and proliferation, and (ii) strict dependency of T_{EM} cells on exogenous serine – establishing these cells as being serine auxotroph.

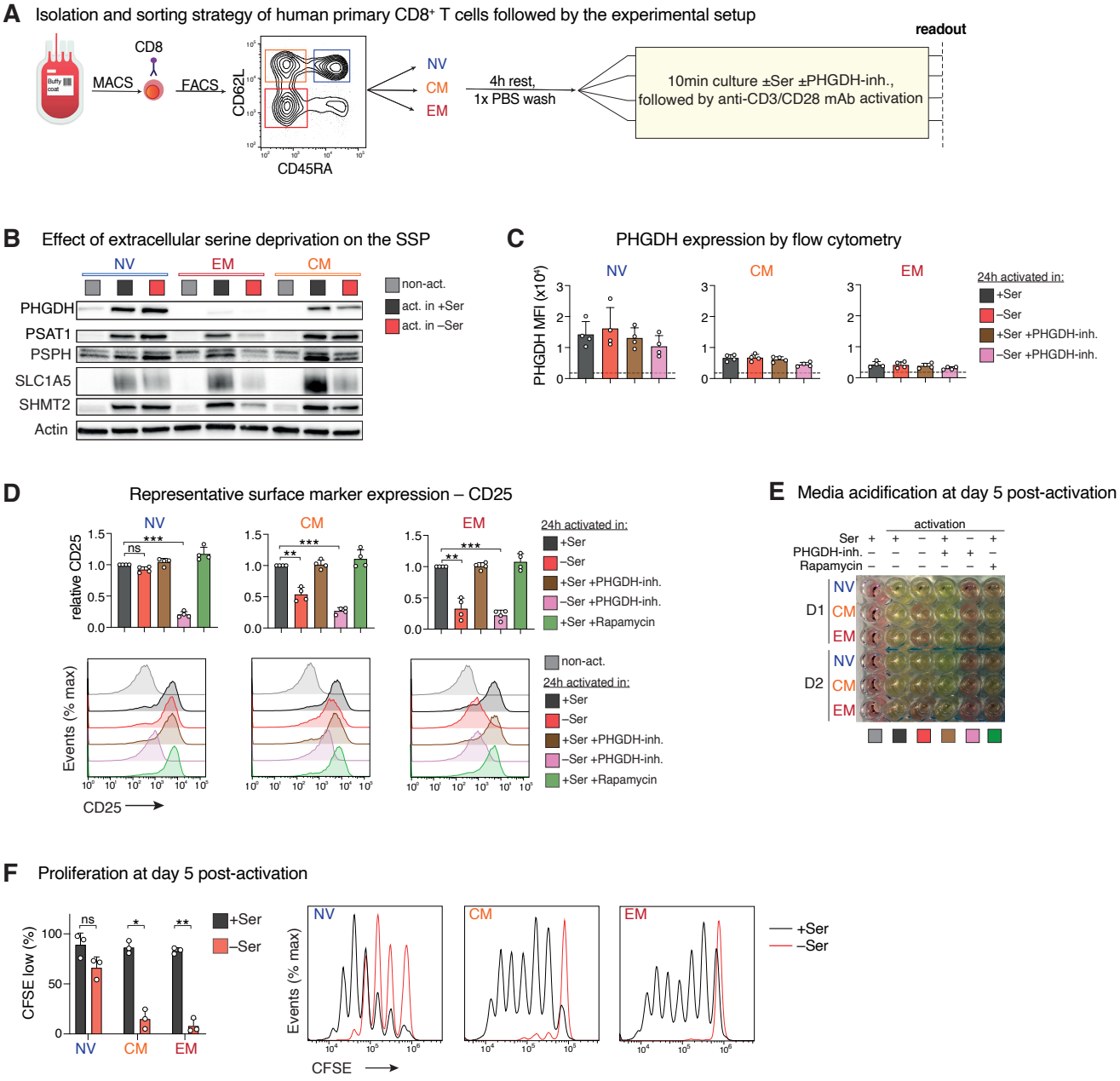

Figure 2. Memory CD8⁺ T cells are serine auxotroph.

Figure 2. Memory CD8+ T cells are serine auxotroph.

(**A**) Schematic of T cell isolation and experimental design. Human CD8+ T cells were MACS-isolated from buffy coats and FACS-sorted based on CD62L and CD45RA expression. After a 4h resting period in the incubator, cells were washed with PBS and resuspended in media ±serine (Ser, 285µM) ±PHGDH-inhibitor (PHGDH-inh., 5µM) for 10min bevor anti-CD3/CD28 mAb activation (act.). Where indicated, non-activated (non-act.) cells were left unstimulated in presence of serine. All conditions contained 10% dialyzed FBS (dFBS).

(**B**) Western blot for serine-metabolism related proteins in human T cell subsets cultured in indicated conditions for 24h. Data are representative of n=2 independent experiments.

(**C**) Intracellular PHGDH staining and flow cytometry of T cell subsets from healthy donors (n=4) upon activation as indicated. The dashed line indicates the mean fluorescent intensity (MFI) obtained with isotype control- and secondary antibody staining.

(**D**) Top: Bar graph summarizing MFIs of CD25 expression on the surface of T cell subsets activated as indicated for 24h, relative to +Ser condition (n=4 donors). Bottom: Representative histogram of CD25 expression of T_{NV}, T_{CM} and T_{EM} cells from one human donor cultured as indicated.

(**E**) Photograph of cell culture plate at 120h post-activation of T cell subsets. Media color indicates differential capacity to acidify the media by T_{NV}, T_{CM} and T_{EM} cells in absence of extracellular serine. Shown are T cells form two human donors (D1 and D2).

(**F**) Assessment of proliferation by CFSE dye dilution at 120h post-activation. Left: Bar graph summary indicating the percentage of cells, which have diluted the dye at least by one cell division (n=3 donors). Right: Representative histogram of CFSE dilution by T_{NV}, T_{CM} and T_{EM} cells from one human donor.

All experiments were done with human primary cells. Data are represented as mean ± SD. Statistical significance was assessed by one-way analysis of variance (ANOVA) (**D**), or two-sided paired Student's *t*-test (**F**). $*P < 0.05$, $**P < 0.01$, $***P < 0.001$; ns, not significant. See also Figure S2.

Act., activation by anti-CD3/CD28 mAb; CFSE, carboxyfluorescein succinimidyl ester; dFBS, dialyzed fetal bovine serum; FACS, fluorescence activated cell sorting; mAb, monoclonal antibody; MACS, magnetic-activated cell sorting; MFI, mean fluorescent intensity; PBS, phosphate buffered saline; PHGDH-inh., PHGDH-inhibitor; SD, standard deviation; Ser, serine; T_{NV}/NV, naïve CD8+ T cells; T_{CM}/CM, central memory CD8+ T cells; T_{EM}/EM, effector memory CD8+ T cells.

4.3 Serine starvation induces cell cycle arrest and p53 target gene upregulation

To explore the transcriptional networks underpinning the serine starvation response of $CD8^+$ T cells, RNA sequencing was performed – comparing resting T_{NV} and T_{EM} cells with their counterparts activated as above, *i.e.* for 24h in ± serine and ± PHGDH-inhibitor. Using unsupervised hierarchical clustering analyses, resting and activated T_{NV} and T_{EM} cells each grouped together (Figure 3A). More importantly, availability of serine separated sub-clusters among activated T_{EM} but not T_{NV} cells. Expectedly, presence of PHGDH inhibitor did not affect clustering of T_{EM} cells, irrespective of serine availability. By contrast, in absence of serine, inhibition of PHGDH did drive separation of T_{NV} cells. The number of differentially expressed genes (DEGs) between conditions mirrored the cluster analysis and revealed that inhibition of PHGDH in presence of extracellular serine did not cause any significant DEGs (Figure 3B). Clustering thus aligned with the PHGDH dependent metabolic and functional analyses of $CD8^+$ T_{NV} and T_{EM} cells described above. To begin exploring the biologic processes triggered in T_{EM} cells in absence of serine, GO term analysis was performed on DEGs in presence *vs.* absence of serine (Figure S3A). From these analyses an enrichment of GO process-networks centering around 'cell cycle' and the interlinked 'DNA damage' theme emerged. The tumor suppressor protein, p53, plays a pivotal role in the ability of cells to sense and respond to stress, including metabolic stress such as glucose- or glutamine starvation (Jones et al., 2005; Lowman et al., 2019). Interestingly, also serine starvation has been proposed to activate p53 in cancer cells (Maddocks et al., 2013). We therefore reasoned that p53 might serve as an unrecognized metabolic checkpoint in immune cells, driving the 'cell cycle' and 'DNA damage' GO terms captured in our analysis. Indeed, serine starvation of $CD8^+$ T_{EM} cells induced expression of numerous direct p53 target genes and decreased expression of DREAM-complex associated genes, which are known to be downregulated by p53 (Figure 3C,D) (Fischer et al., 2016). In fact, classical p53 targets – such as PHLDA3, BBC3, EDA2R, TP53INP1, TNFRSF10D, TRIM22, ATF3, and ACTA2 – were among the most highly upregulated genes in serine starved T_{EM} cells, whereas DREAM targets represented major downregulated transcripts (Figure 3E). Among $CD8^+$ T_{NV} cells, removal of serine from the culture media led to reduced expression of cell cycle genes, consistent with their somewhat decreased proliferation in absence of extracellular serine (Figure 3D). However, the upregulation of p53 target genes as found in serine deprived T_{EM} cells was only induced in T_{NV} cells when combining serine starvation with inhibition of PHGDH (Figure 3C). As a functional correlate consistent with the transcriptome signature of p53 activation, cell cycle analysis of these cells revealed a failure to pass the G1/S checkpoint (Figure S3B). Together, these data

established p53 as a novel metabolic checkpoint – induced by serine starvation – in primary human CD8+ T cells.

A broad arrest of normal cellular processes combined with specific activation of pathways required to reinstate homeostasis and ensure cell survival is the prototypic pattern of cellular stress responses (Pakos Zebrucka et al., 2016). Repression of Myc can induce such a general inhibition by dampening overall transcription, leading to decreased total RNA abundance (Lin et al., 2012; Nie et al., 2012). p53 has been shown to transcriptionally inhibit Myc in response to DNA damage. Through this cooperation with Myc, overall transcription shuts down – allowing p53 target genes to be efficiently transcribed and restore homeostasis (Porter et al., 2017). This prompted us to explore whether induction of p53 in serine starved CD8+ T_{EM} cells was associated with changes in Myc transcript or protein levels, as well as overall cellular RNA abundance. Indeed, in serine starved T_{EM} cells, Myc protein was lacking and RNA levels globally reduced (Figure 3F and Figure S3C). Intriguingly, transcripts of Myc in serine starved T_{EM} cells were not decreased (Figure S3D). Global translational activity of serine starved T_{EM} cells was, however, reduced – more profoundly even than when treating these cells with rapamycin (Figure 3G and Figure S3E). This suggested that, in CD8+ T_{EM} cells, Myc coordinated with p53 through post-transcriptional regulation. To explore the idea that in CD8+ T_{EM} cells serine availability directly affected Myc protein abundance – and thus the p53-Myc balance – acute serine withdrawal experiments (1h) were performed. In this context it was important to consider that activity of mTOR complex 1 (mTORC1) – the prototypic AA sensor, which has been proposed to be sensitive to serine as well (Goberdhan et al., 2016) – was also diminished in serine starved T_{EM} cells, and responded like Myc in a serine dose-dependent manner (Figure S3F,G). By studying mTORC1 and Myc in parallel we aimed to disentangle direct effects of serine availability on Myc protein abundance from indirect, mTORC1 mediated ones. Specifically, activated primary and secondary effector CD8+ T cells, characterized by high Myc and mTORC1 signaling activity, were assessed. PHGDH remained differentially expressed also in these highly activated cells at 36h post-activation (Figure S3H). Primary effector T cells, *i.e.* effector cells expressing PHGDH, were able to sustain Myc levels under acutely serine-deprived conditions, unless PHGDH was blocked pharmacologically (Figure S3I). In secondary effector cells, *i.e.* effector cells lacking PHGDH, Myc levels dropped upon short term serine starvation, without further impact of the PHGDH-inhibitor. Myc protein was thus highly sensitive to serine availability. Phosphorylation of the mTORC1 target, p70S6K, by contrast, did not significantly change upon acute serine starvation and, inversely, short term as well as long-term mTORC1 inhibition with rapamycin resulted in an only slight reduction of Myc protein (1h treatment in Figure S3I, 24h treatment in Figure 3F). Together, these data

demonstrated that lack of serine was rapidly reducing Myc levels independently of changes in mTORC1 activity. Additional evidence that mTOR signaling was not directly impacted by serine availability was obtained from add back experiments, where serine alone was not sufficient to trigger phosphorylation of mTORC1 targets in AA starved cells, while e.g. leucine was (Appendix A1D). Myc protein abundance was thus directly regulated by serine availability, plausibly due to the very short half-life of Myc (Preston et al., 2015), and likely emphasized by serine being the most abundant AA of the Myc protein (Figure S3J). Further, albeit indirect, support for the importance of p53 in orchestrating the serine-starvation stress response in T cells came from experiments interrogating CIRSPR-Cas9 generated PHGDH-knockout ($PHGDH^{KO}$) Jurkat T cell clones (Figure S3K,L). Through transcriptome analysis, we detected intron retention and formation of a premature termination codon, caused by a synonymous mutation located in the related donor splice-site of the *TP53* gene of Jurkat T cells (Figure S3M) (Jung et al., 2015). These $PHGDH^{KO}$ cells thus offered an opportunity to study the impact of serine starvation in a p53 deficient system. Short term (1h) serine starvation of p53 deficient $PHGDH^{KO}$ cells induced rapid loss of Myc protein, analogous to primary $CD8^+$ T_{EM} cells, whereas in $PHGDH^{WT}$ cells Myc protein remained stable unless PHGDH was inhibited pharmacologically (Figure S3N). However, unlike serine auxotroph (but p53 competent) primary T_{EM} cells, viability of $PHGDH^{KO}$ clones was sharply reduced when cultured in absence of extracellular serine (Figure S3O) – compatible with failure to mount a viability-promoting p53 response (Maddocks et al., 2013). Cell cycle profiles of serine starved $PHGDH^{KO}$ cells revealed the appearance of a peak in S phase (Figure S3P). This suggested bypassing of the G1/S checkpoint, likely as a result of p53 deficiency and subsequent arrest in S phase due to metabolic collapse – reflected by an rapidly increasing sub-G1 population, *i.e.* accumulation of apoptotic cells.

In all, these experiments identified p53 as a metabolic checkpoint of human $CD8^+$ T cells and uncovered a post-transcriptional mode of cooperation between p53 and Myc in serine starved cells (Figure 3H). Given the profound impact cellular serine depletion had in T cells, the key question that arose from these data was how silencing PHGDH in memory T cells, and thus compromising metabolic flexibility, was beneficial and thus selected for.

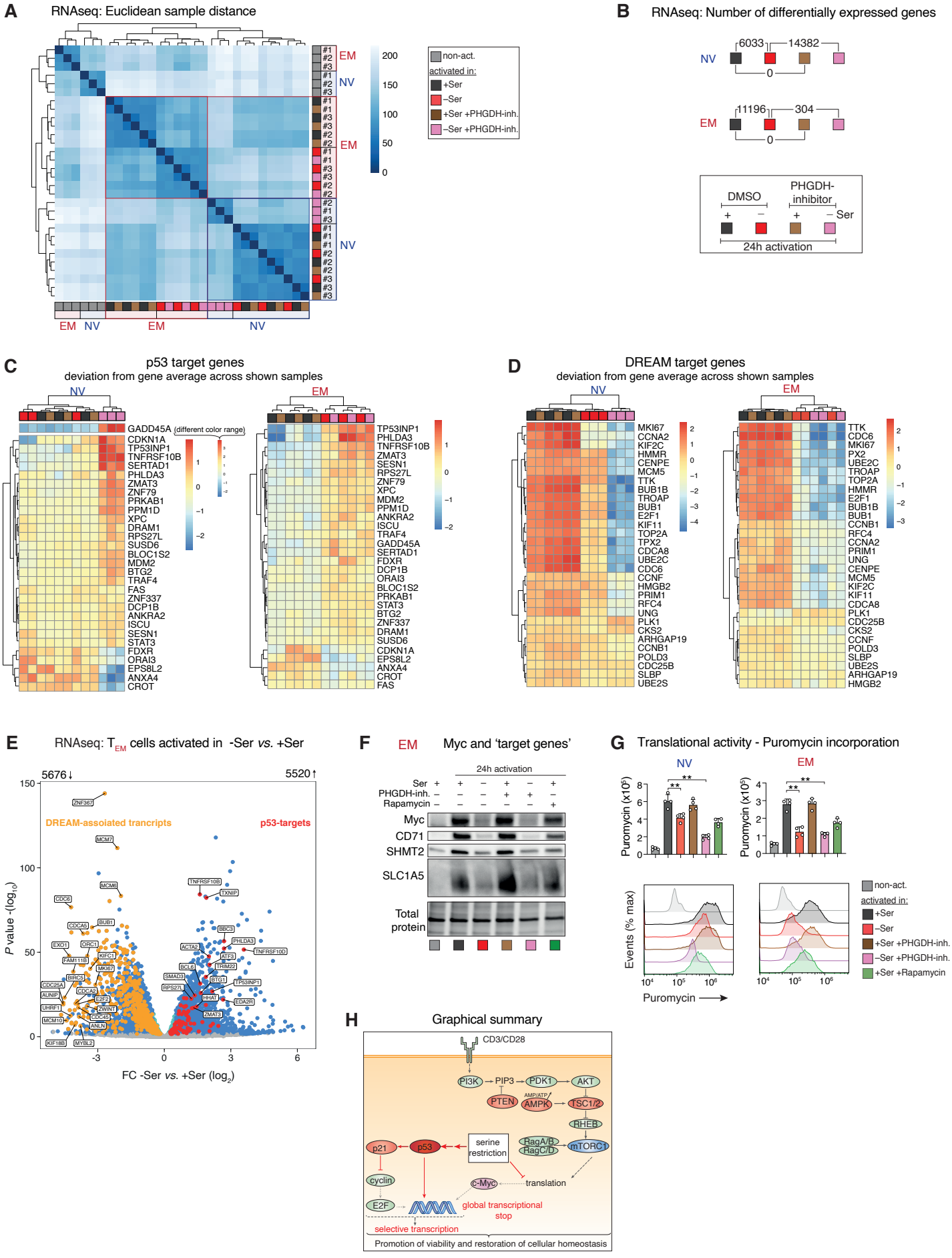

Figure 3. Serine starvation induces a p53 centered stress response.

Figure 3. Serine starvation induces a p53 centered stress response.

(**A**) Heatmap based on RNAseq experiment form T cell subsets activated for 24h under indicated conditions (visualized in the box and color-coded in the heatmap). Displayed is the euclidean distance between samples as calculated from regularized log transformed data. Darker color indicates higher similarity resp. smaller euclidean distance (n=3 donors, labeled as #1-3).

(**B**) Summary of the number of detected, differentially expressed genes with $p_{adj}<0.05$ between indicated conditions according to the RNAseq experiment.

(**C** and **D**) Heatmap displaying p53- (C) and DREAM- (D) target genes colored according to deviation from gene average across shown samples for T_{NV} and T_{EM} cells. GADD45A in T_{NV} cells is displayed on a separate scale, as it consumed the whole color range. Information on the selection of the genes lists can be found in the Methods Section.

(**E**) Volcano plot visualization of RNAseq data from T_{EM} cells activated in ±Ser. Among upregulated transcripts, p53 target genes are labeled in red, among downregulated transcripts, DREAM targets are labeled in yellow. Top differentially expressed genes are labelled.

(**F**) Representative Western blot showing Myc levels and selected 'Myc inducible proteins' (CD71, SHMT2 and SLC1A5) in T_{EM} cells activated for 24h under indicated conditions.

(**G**) T_{NV} (left panels) and T_{EM} cells (right panels) were activated for 24h in indicated conditions and puromycin was added to the media for the last 10min. As a tyrosyl-tRNA analogue, puromycin enters actively translating ribosomes and is incorporated into nascent polypeptide chains, which can be quantified with a fluorescent anti-puromycin antibody. Bar graphs represent a quantification of anti-puromycin mean fluorescence intensity (MFI; n=4 donors). The histograms show a representative flow cytometry plot for each, T_{NV} and T_{EM} cells.

(**H**) Graphical scheme of proposed coordination between p53 and Myc in serine starved T cells.

All experiments were done with human primary cells. Data are represented as mean ± SD. Statistical significance was assessed by one-way analysis of variance (ANOVA) (**G**). $^{**}P < 0.01$. See also Figure S3.

DREAM, dimerization partner, RB-like, E2F and MYBL2 complex; MFI, mean fluorescence intensity; p_{adj}, adjusted p-value; PHGDH-inh., PHGDH-inhibitor; SD, standard deviation; Ser, serine; T_{NV}/NV, naïve $CD8^+$ T cells; T_{EM}/EM, effector memory $CD8^+$ T cells.

4.4 Protection by CD8+ memory T cells depends on extracellular serine, effector T cell contraction on silencing of PHGDH

We reasoned that studying PHGDH *in vivo* during infection and memory CD8+ T cell formation might provide clues as to why the enzyme was silenced in memory cells. With the aim to establish a mouse infection model we first assessed how our human data translated to the murine setting. Inspection of RNAseq data from the ImmGen Consortium (immgen.org) suggested that the expression pattern of PHGDH between murine CD8+ naïve, central memory and effector memory T cells is similar to the one we identified in human cells (Figure 4A). Western blotting and flow cytometric analyses confirmed decreased PHGDH protein expression in murine memory as compared to naïve T cells (Figure 4B) – albeit differential expression being not as pronounced as in human T cells. As predicted, activating bulk CD8+ T cells from mice housed under SPF conditions – *i.e.* mostly naïve T cells – in the absence of serine, did no detectably impact Myc levels, nor CD71 expression (Figure 4C). Pharmacological inhibition of PHGDH in absence of serine, however, impaired activation induced blasting, Myc and CD71 expression, aligning with our human data. To test the immunologic relevance of PHGDH deficiency in memory CD8+ T cells *in vivo*, we examined functionality of memory CD8+ T cells in a serine/glycine low environment. Specifically, C57BL/6 mice were infected with an attenuated listeria monocytogenes strain expressing OVA (LmOVA) to induce OVA-specific memory T cells. Thirty days post infection (dpi), half of the colony was switched to a serine/glycine free diet for 2 weeks (Figure 4D). At 44 dpi – the day of reinfection – the percentage of OVA-tetramer positive memory and effector precursor T cells was similar in mice maintained on serine/glycine free- *vs.* serine/glycine-sufficient diets (Figure S4A,B). Mice not harboring LmOVA-specific memory (*i.e.* not previously infected with attenuated LmOVA) did not survive infection with virulent LmOVA (data not shown). By contrast, 'memory mice' – irrespective of diet – did survive, establishing the presence of some degree of protective memory in both cohorts. Importantly, however, a significant reduction both in percentage and absolute numbers of OVA-specific CD8+ T cells was observed in mice fed a serine/glycine-free diet (Figure 4E), whereas the relative composition of the effector populations did not change (Figure S4C). Furthermore, following *ex vivo* re-stimulation with OVA257 peptide (SIINFEKL), the number of CD8+ T cells producing IFNγ, TNF and granzyme B was also reduced (Figures S4D). Impaired memory T cell expansion and effector function translated into a decrease in bacterial clearance in mice maintained under serine/glycine-free diet (data not shown).

Given the price payed by shutting down the capacity for endogenous serine synthesis in memory cells, we reasoned that at some level silencing PHGDH had to be a requirement for

a normal naïve to memory transition to occur. Otherwise such an impactful metabolic pruning event would not have been evolutionary beneficial and thus selected for. To explore this notion, we generated ovalbumin (OVA) specific CD8+ OT-I T cells overexpressing PHGDH (OE-PHGDH) or harboring an empty vector (EV) (Figure 4F,G). These engineered T cells were then adoptively transferred and mice challenged with an LmOVA infection one day post transfer. At the peak of clonal expansion (7 dpi), numbers of antigen-specific effector CD8+ T cells containing EV compared to OE-PHGDH were similar, and percentages of IFNγ-positive cells comparable (Figure 4H, S4E). However, T cells genetically enforced to express PHGDH failed to undergo a normal contraction, resulting in higher numbers of antigen specific T cells at 14, 21, 28 and 35 dpi (Figure 4H) – up until at least 70 dpi (data not shown). We next examined the phenotype of adoptively transferred T cells at 7 dpi and 14 dpi, but did not find differences in CD127 (IL-7 receptor important for memory T cell maintenance) or KLRG1 (inversely correlated with long lived memory cells) expression compared to cells expressing the EV (Figure 4I).

These data established that silencing of PHGDH came at a cost, namely dependency on sufficient extracellular serine to mount an optimal CD8+ T cell recall response. At the same time, however, preventing shut down of PHGDH impacted a normal T cell response by hindered the process of effector T cell contraction.

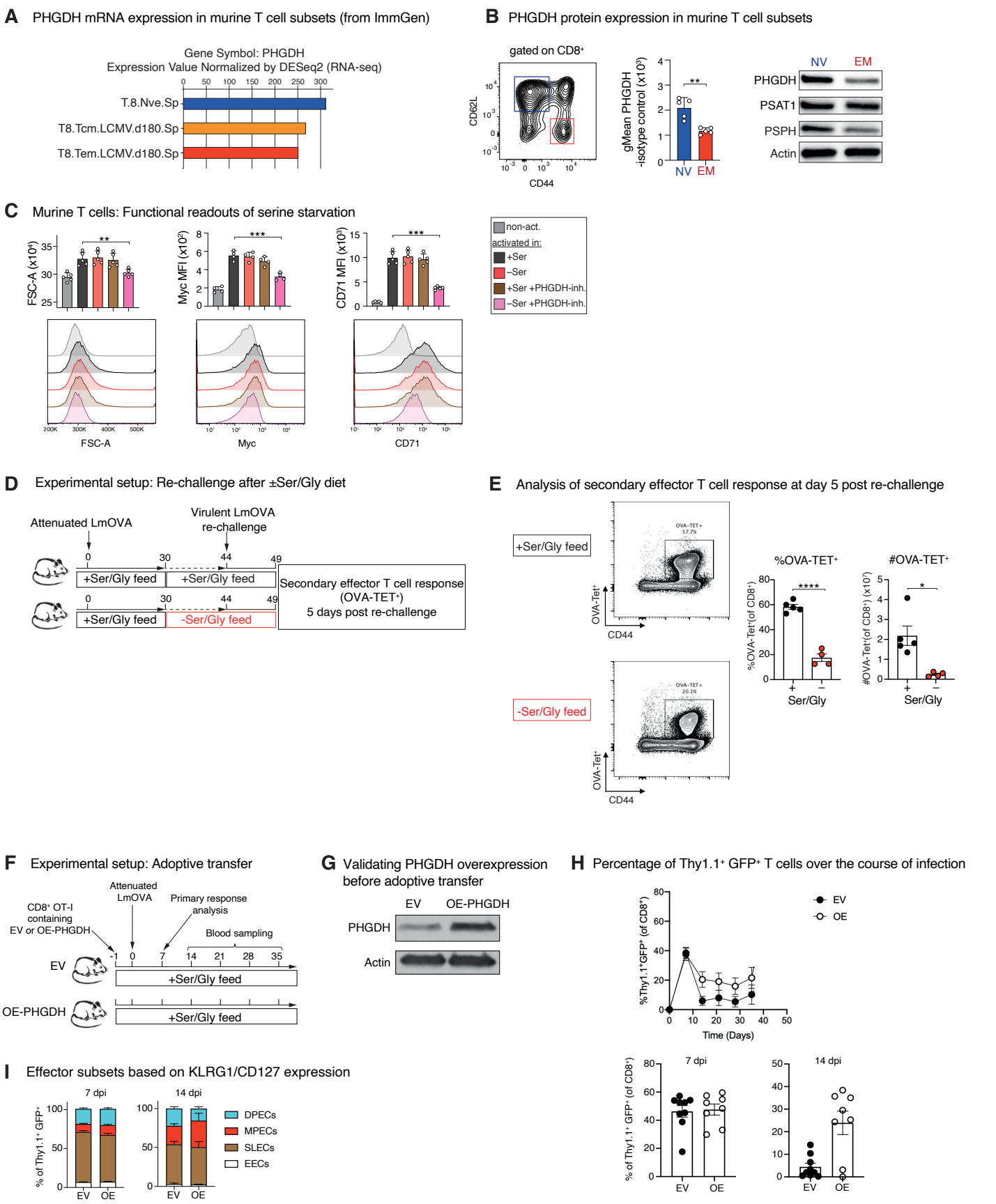

Figure 4. Memory T cells depend on extracellular serine; effector T cell contraction requires silencing of PHGDH.

Figure 4. Memory T cells depend on extracellular serine; effector T cell contraction requires silencing of PHGDH.

(**A**) PHGDH mRNA expression according to the ImmGen database among splenic (Sp) murine T cell subsets. Normalized expression values for naïve (T.8.Nve.Sp), LCMV specific central memory (T8.Tcm.LCMV.d180.Sp) and effector memory CD8$^+$ T cells (T8.Tem.LCMV.d180.Sp) are shown. Annotations are replicated from ImmGen.

(**B**) Left: Sorting strategy for murine CD8$^+$ T_{NV} and T_{EM} cells based on expression of CD62L and CD44. Bar graph depicts PHGDH levels quantified by intracellular flow cytometry among splenic T_{NV} and T_{EM} cells (n=5 mice). Right: Western blot of the SSP-enzymes in sorted, non-activated murine T_{NV} and T_{EM} cells (pooled cells of 5 mice).

(**C**) Flow cytometry assessment of murine CD8$^+$ T cells activated for 24h as indicated. Top: Bar graphs summarizing FSC-A, and MFIs of Myc and CD71 expression (n=5 mice). Bottom: Representative histograms related to the bar graphs obtained from T cells of one mouse.

(**D**) Schematic of the LmOVA re-challenge experiment. OVA-specific CD8$^+$ memory T cells were generated by a first infection with attenuated LmOVA. After memory formation, the feed was switched in half of the mice to a serine/glycine-free diet for two weeks in order to deplete circulating levels of these two amino acids (Ma et al., 2017). Then, a secondary effector response was induced by re-infecting the mice with virulent LmOVA.

(**E**) Left: Representative flow cytometry contour plots of OVA-specific secondary effector T cells (gated on CD8$^+$ T cells) from the spleen of mice fed the control (+) or serine/glycine-free (-) diet for two weeks before re-infection. Right: Percentage and total number of splenic OVA-specific CD8$^+$ secondary effector T cells 5 days post re-infection (n=5 mice per cohort).

(**F**) Schematic of the adoptive transfer experiment using OVA-specific OT-I T cells (Thy1.1$^+$) expressing either an empty vector (EV) or overexpressing PHGDH (OE-PHGDH), both containing GFP. One day after adoptive transfer, mice were challenged by an infection with attenuated LmOVA. Blood was sampled at indicated timepoints to determine the amount of adoptively transferred T cells at different days post-infection.

(**G**) Western blot for PHGDH comparing EV and OE-PHGDH OT-I T cells before adoptive transfer.

(**H**) Top: Percentage of Thy1.1$^+$ GFP$^+$ T cells containing EV or OE-PHGDH over the course of infection (n=5). Bottom: Bar graph representation of the same data, focusing on 7 dpi and 14 dpi readouts.

(**I**) Percentage of short-lived effector cells (SLECs; KLRG1^{hi}CD127^{lo}), memory precursor effector cells (MPECs; KLRG1^{lo}CD127^{hi}), early effector cells (EECs; KLRG1^{lo}CD127^{lo}) and double-positive effector cells (DPECs; KLRG1^{hi}CD127^{hi}) at 7 dpi and 14 dpi.

Data are represented as mean ± SD (**B**,**C**) or mean ± SEM (**E**). Statistical significance was assessed by one-way analysis of variance (ANOVA) (**C**), or two-sided unpaired Student's *t*-test (**B**, **E**). $^*P < 0.05$, $^{**}P < 0.01$, $^{***}P < 0.001$; ns, not significant. See also Figure S4.

D180, 180 days post-infection; Dpi, days post infection; EV, empty vector; FSC-A, forward scatter area; GFP, green fluorescent protein; Gly, glycine; ImmGen, Immunological Genome Project; LCMV, lymphocytic choriomeningitis virus; LmOVA, listeria monocytogenes strain expressing OVA; OE, overexpression (of PHGDH); OVA, ovalbumin; OVA-Tet, ovalbumin tetramer; SEM, standard error of the mean; Ser, serine; SD, standard deviation; Sp, Splenic; T8, CD8$^+$ murine T cells.

4.5 PHGDH is silenced with cell differentiation across various biologic systems

The finding that silencing PHGDH was a prerequisite for effector CD8$^+$ T cell contraction led us to investigate the association between expression of PHGDH and differentiation in other cell types. Human CD4$^+$ T cells also silenced PHGDH from naïve to memory transition (Figure S5A), and the ImmGen database listed the overall expression pattern of PHGDH as 'downregulated with differentiation' (Figure S5B). Fittingly, in the same data base thymocytes are described as expressing more PHGDH even than T_{NV} cells, and chromatin accessibility around the first intron of *PHGDH* decreases with increasing differentiation stage (Figure S5C,D). We thus went on and assessed how expression of PHGDH related with the differentiation state in THP-1 cells (monocytic) and HL-60 cells (granulocytic), which are routinely used to study cell differentiation, *in vitro*. In both cell lines expression of PHGDH was progressively downregulated with differentiation (Figure 5A,B). Intriguingly, also in non-hematologic systems PHGDH has been shown to be reduced with differentiation (e.g. neurons (Kinoshita et al., 2009), breast-, prostate- and colonic-epithelial tissues (Dotti et al., 2017; Gromova et al., 2015)) – a notion further supported by mining data from the human protein atlas (proteinatlas.org) (Figure S5E). Notably, knocking down PHGDH in cancer stem cells has been shown to lower expression of stemness-regulating factors and promote differentiation (Sharif et al., 2018). Inversely, in de-differentiated cancer cells, PHGDH is increasingly recognized as a tumor promoter (Locasale et al., 2011; Possemato et al., 2011; Rotondo et al., 2014; Zhang et al., 2017). While the current dogma largely maintains that PHGDH is fueling anabolic metabolism, it has been shown that knockdown of PHGDH inhibits proliferation even in the presence of abundant extracellular serine (Liu et al., 2013; Ma et al., 2019a; Mattaini et al., 2015; Possemato et al., 2011; Unterlass et al., 2017). Likewise, compounds disrupting oligomerization of PHGDH have anti-cancer activity also in presence of abundant serine and glycine (Ngo et al., 2020). Therefore, our experimental findings in conjuncture with data from the public domain suggested (i) that silencing PHGDH was broadly associated for differentiation and stable cell identity, and (ii) that additional, non-enzymatic roles of PHGDH had to be considered. Stable and limited engagement in enzymatic activity in activated T_{NV} cells despite increasing abundance of PHGDH was further supporting the latter idea (Figure S1B).

4.6 The R163Q PHGDH mutation, leading to Neu-Laxova syndrome, largely maintains enzymatic activity

The Neu-Laxova syndrome (NLS) is a lethal genetic disorder associated with mutations in enzymes of the SSP (Abdelfattah et al., 2020; Acuna-Hidalgo et al., 2014; de Koning, 2017; Shaheen et al., 2014). NLS often presents with features reminiscent of disruption of fundamental cellular processes, such as proliferation and differentiation (Shaheen et al., 2014). Mutations leading to NLS, including those in *PHGDH*, have been proposed to represent the severe end of the spectrum of serine deficiency (Figure 5C, Model 1). With the link between PHGDH and cell differentiation in mind, we decided to revisit this notion and compared the functional importance and enzymatic activity of wild type-, catalytic dead-, and a NLS mutation carrying PHGDH protein. Specifically, using lentiviral vectors we re-introduced the following PHGDH variants into $PHGDH^{KO}$ Jurkat T cells: wildtype ($PHGDH^{WT}$), catalytic dead (R236E; $PHGDH^{dead}$) (Mattaini et al., 2015), and a mutation known to cause NLS (R163Q; $PHGDH^{NLS}$) (Shaheen et al., 2014). Mutations were confirmed by sequencing the expression vectors, and translation of PHGDH protein was controlled for by Western blotting (Figure S5F, 5D). When cultured in absence of extracellular serine, cells containing $PHGDH^{WT}$ as well as $PHGDH^{NLS}$ were both able to similarly acidify the media, proliferate and survive – which was in contrast to $PHGDH^{dead}$ and $PHGDH^{KO}$ cells (Figure 5E). Furthermore, *in vitro* activity assays revealed that $PHGDH^{NLS}$ had catalytic activity of approximately 70% relative to that of $PHGDH^{WT}$ (Figure 5F). As residual enzyme activities in patients with nonlethal forms of PHGDH mutations range between 12% and 25% (Tabatabaie et al., 2009), this was challenging the idea that NLS necessarily represents a severe form of PHGDH enzymatic deficiency (Model 1 in Figure 5C). Rather, our data were compatible with the concept that certain pathogenic *PHGDH* variants impair serine synthesis, while others may contribute to NLS by affecting an unrecognized, non-enzymatic function of the protein (Model 2 in Figure 5C). Together, these clinically informed analyses thus further supported our hypothesis that a moonlighting role of PHGDH was critically involved in regulating cell differentiation.

4.7 PHGDH is an unrecognized RNA-binding protein

To explore possible moonlighting roles of PHGDH, we first investigated protein interaction partners of PHGDH using the STRING database (Szklarczyk et al., 2017). This interrogation returned several RNA-binding proteins (RBPs) (Figure S5G). Furthermore, PHGDH has been shown experimentally to interact with additional RBPs in cancer cells (Ma et al., 2019b), and RBPs have a propensity to interact with each other (Brannan et al., 2016). We therefore hypothesized that PHGDH could be an RBP itself. Indeed, while not annotated as such, PHGDH was found to interact with RNA in various RNA-interactome capture studies (Bao et al., 2018; Castello et al., 2016; Liao et al., 2016; Queiroz et al., 2019; Trendel et al., 2019; Urdaneta et al., 2019). One of the best characterized metabolic enzymes previously established to moonlight as an RBP is GAPDH, classified as a non-canonical one due to lack of a classical RNA-binding domain. For GAPDH, several regions have been proposed to bind RNA, including the Rossmann fold (a super-secondary structure responsible for interaction with the di-nucleotide NAD^+), the positively charged substrate binding groove, and the dimer interface (Figure 5G) (White and Garcin, 2015). Since PHGDH is also an NAD^+-dependent dehydrogenase, we compared structural properties of GAPDH and PHGDH, *in silico* (Figure 5G). Several similarities between the two enzymes were noted: beside the Rossmann fold, PHGDH also displayed a positively charged substrate groove and a dimer interface with basic and aromatic residues. Interestingly, for PHGDH all these putative RNA-binding surfaces are located in a defined region, where intriguingly, various AAs are located, which can cause NLS if mutated, including the R163 characterized above (labeled red in Figure 5G). Of note, mutations at the dimer interface of GAPDH have been shown to impair RNA-binding (White et al., 2015). Additionally, the R163Q variant is missing an arginine, the AA which – across all RNA-binding domains – is most frequently involved in hydrogen bond formation with RNA (Corley et al., 2020). Given the largely conserved catalytic activity of PHGDH R163Q, these *in silico* observations pointed at the possibility that NLS could be, at least in part, an RNA-binding pathology. Furthermore, these insights suggested that PHGDH could function as an RBP in human T cells as well.

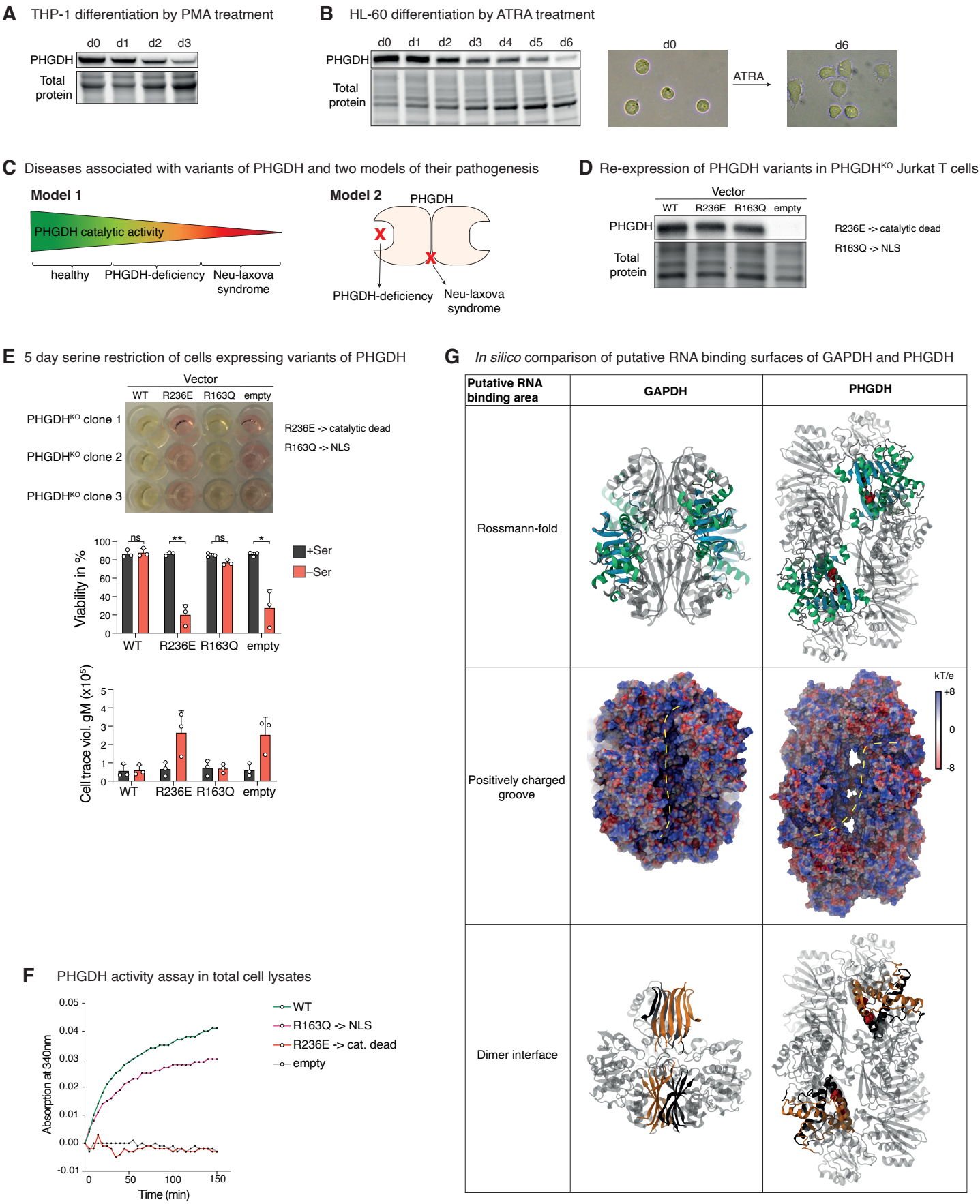

Figure 5. PHGDH is downregulated in various differentiating cells and is an unappreciated RNA-binding protein – a potentially relevant role for the pathogenesis of the NLS.

Figure 5. PHGDH is downregulated in various differentiating cells and is an unappreciated RNA-binding protein – a potentially relevant role for the pathogenesis of the NLS.

(**A**) Western blot of total cell lysates of THP-1 cells stained for PHGDH at indicated days (d) after PMA (50ng/ml) induced differentiation.

(**B**) Left: Western blot of total cell lysates of HL-60 cells stained for PHGDH at indicated days (d) after ATRA (1μM) induced differentiation. Right: Light microscopy image illustrating the morphological changes associated with ATRA induced differentiation from pro-myeloblastic to granulocytic cells.

(**C**) Gene variants of *PHGDH* are associated with a clinically broad spectrum of disorders. The illustration shows two models aiming to explain this phenotypic diversity. In Model 1, Neu-Laxova syndrome (NLS) has been proposed to represent the severe end on the scale of serine deficiency disorders (includes PHGDH-deficiency) with very low residual catalytic activity. Model 2 suggests that mutations which affect catalytic activity lead to the serine deficiency syndrome, while mutations affecting PHGDHs moonlighting function(s) lead to the NLS.

(**D**) Western blot of $PHGDH^{KO}$ Jurkat T cells, where indicated variants of PHGDH were re-introduced by using a lentivirus.

(**E**) $PHGDH^{KO}$ clones re-expressing PHGDH variants (as indicated) were cultured for 5 days in absence of extracellular serine. Top: The photograph shows differential acidification by cells containing PHGDH variants, when cultured in absence of extracellular serine. Middle: Viability was assessed with a cell permeable viability dye and flow cytometry (same cells as shown above). Bottom: Cell trace violet based proliferation assay gated on viable cells, which are reduced at this timepoint in cells transduced with $PHGDH^{dead}$ and empty lentiviruses. Higher geometric mean (gM) of cell fluorescence indicates less dilution of the dye by proliferation.

(**F**) Enzymatic activity of PHGDH in protein lysates from $PHGDH^{KO}$ Jurkat T cells re-expressing PHGDH variants as indicated. Catalytic activity was determined by measuring the PHGDH mediated production of NADH, which results from the reduction of 3-phosphoglycerate (3PG). By assessing the absorption of light with a wavelength of 340nm, NADH formation was measured over time – after addition of the substrate of PHGDH, *i.e.* 3PG. Displayed are absorption values in presence of 3PG subtracted by absorption values obtained in absence of 3PG. Curves are representative of two independent experiments.

(**G**) Comparison of putative RNA-binding sites in GAPDH (left) and PHGDH (right). Structural features of GAPDH involved in RNA-binding (White and Garcin, 2015) are highlighted and compared to PHGDH. Top: The Rossman fold domains of each two interacting subunits are shown in green (α-helices) and blue (β-sheets), whereas R163 is labeled in red. Middle: Electrostatic potential of surface residues. The yellow lines highlight regions of high positive potentials, possibly involved in electrostatic interactions with negatively charged RNA. Bottom: Dimer interface. For GAPDH, the two ensembles of five stranded β-sheets are shown in black and orange, one color per subunit – the rest of the protein is shown in pale grey ribbons. In the interface shown, one subunit has been removed for clarity – except residues of the interface. For PHGDH, the dimer interface is shown in black and orange, one color per subunit – the rest of the protein is shown in pale grey ribbons. Again, R163 is labeled in red.

Data are represented as mean ± SD. Statistical significance was assessed by two-sided paired Student's *t*-test (**E**). $^{*}P < 0.05$, $^{**}P < 0.01$; ns, not significant. See also Figure S5.

3PG, 3-phophoglyerate; ATRA, all-trans-retinoic acid; E, glutamate; GAPDH, glyeraldehyde-3-phophate dehydrogenase; NLS, Neu-Laxova syndrome; PHGDH, Phosphoglycerate dehydrogenase; PMA, Phorbol 12-myristate 13-acetate; Q, glutamine; R, arginine; SD, standard deviation; Ser, serine; WT, Wildtype.

4.8 PHGDH functions as an RNA-binding protein in primary T cells.

To explore a potential RNA-binding role of PHGDH in T cells experimentally, RNA immunoprecipitation sequencing (RIPseq) experiments with primary human effector T cells were performed (schematically illustrated in Figure 6A). Specificity of the PHGDH-immunoprecipitation (IP) antibody was validated on $PHGDH^{KO}$ lysates (Figure S6A), and successful IP of PHGDH confirmed for each sample before sequencing of co-precipitated RNA (Figure 6A). Negative control IPs were performed using isotype matched antibodies, and input samples were taken before the IPs to test for enrichment of transcripts over input. Compared to input samples, PHGDH-IP significantly enriched 4419 transcripts, whereas isotype-IP enriched 927 (Figure S6B). To visualize our filtering strategy, transcripts enriched by isotype-IP over input material were plotted against transcripts enriched in the PHGDH-IP over input material. RNA species that were (i) enriched >2 fold in the PHGDH-IP over input, and (ii) enriched 2-times more in the PHGDH-IP when compared to the isotype-IP, were considered to specifically interact with PHGDH. This filtering process selected for 1169 protein coding transcripts (Figure 6B), suggesting RNA-binding features of PHGDH in primary human T cells. Since expression of PHGDH was a hallmark of undifferentiated cells (Figure 5A,B and Figure S5A-E), and silencing of PHGDH was required for effector T cell contraction to occur (Figure 4H), we considered that PHGDH may contribute to maintaining stemness and survival through its RNA-binding properties. In support of this idea, GO term enrichment analysis identified transcripts of several key biologic pathways involved in regulating stemness, cell fate and viability as being bound by PHGDH, including 'transcription/epigenetic regulation of gene expression', 'WNT/beta-catenin signaling' and 'apoptosis/survival' (Figure S6C). To further explore this notion and test the functional relevance of these interactions, we designed PHGDH knockout experiments with sorted primary human T_{NV} cells. To ensure that loss of PHGDH predominantly affected the enzymes' RNA-binding properties, and to prevent a metabolic stress response, experiments were done in presence of abundant extracellular serine, where catalytic activity of PHGDH was found to be low (Figure 1F, S1B). Gene-editing was performed in non-activated T_{NV} cells, with the idea to inhibit the later on activation induced upregulation of PHGDH (experimental design summarized in Figure 6C). Based on recent literature, 24h after ribonucleoprotein (RNP) electroporation, Cas9 induced DNA double-strand break (DSB) formation and repair is resolved (Wang et al., 2019). Since cell-type- and loci specific effects might exist, we investigated the kinetics of DNA-DSB repair in our system by assessing the phosphorylation of H2AX (γH2AX), which is known to be induced around a DSB undergoing active repair (Mah et al., 2010). This analysis revealed that electroporation of Cas9 loaded with PHGDH-targeting guide RNA (gRNA) rapidly induced γH2AX formation,

which resolved 24h after electroporation (Figure S6D). After gene-editing and resting period of 24h post-electroporation, T cells were activated. One day after anti-CD3/CD28 mAb mediated activation of PHGDH-gRNA *vs.* negative-gRNA (non-targeting) RNP treated cells, PHGDH protein levels were not yet significantly different between conditions (data not shown). At this early timepoint, PHGDH mRNA was the most downregulated transcript among 60 DEGs (Figure S6E). Unsurprisingly after Cas9 nuclease mediated gene-editing, these DEGs were mainly p53 target genes (Figure S5E,F), whereas activation induced transcriptome rearrangement of around 17'300 genes was not affected by the gene-editing process (data not shown). By day 3 post-activation, Western blotting confirmed loss of PHGDH, whereas flow cytometry indicated no impact of the intervention on viability, blasting or CD71 upregulation (Figure 6D). At this timepoint, 1425 DEGs were detected (Figure 6E), their small fold-changes aligning with post-transcriptional interference of other RBPs (Díaz-Muñoz et al., 2015; Lu et al., 2014; Monzón-Casanova et al., 2020). Among these DEGs, roughly 10% (177) were specifically pulled-down also in the RIPseq experiment, including RNAs coding for epigenetic modifiers (KDM3A, DOT1L, KAT2A and KDM6B), components of WNT signaling (DVL1 and Jun) and transcripts impacting survival (NFKBIA and IRF1) (Figure 6F). To further substantiate the observation of PHGDH functioning as an RBP, we established fluorescent polarization (FP)- and electrophoretic mobility shift assays (EMSA) by using GAPDH and one of its published target RNA sequences (Figure S6G, H) (White et al., 2015). With this reductionist system, we aim to test the binding of purified PHGDH protein with some of our RNA hits.

Together, these data suggest that PHGDH is moonlighting as an RBP, and they were compatible with the notion that, through RNA-binding, PHGDH may contribute to regulating T cell differentiation or survival.

In all, a molecular framework thus emerged, where silencing of PHGDH was necessary to prevent PHGDH from moonlighting in order to replace the stemness-maintaining transcriptional network of naïve T cells with a differentiation-permissive cellular state. Silencing of PHGDH came, however, at the significant cost of inducing serine auxotrophy in the memory T cell compartment.

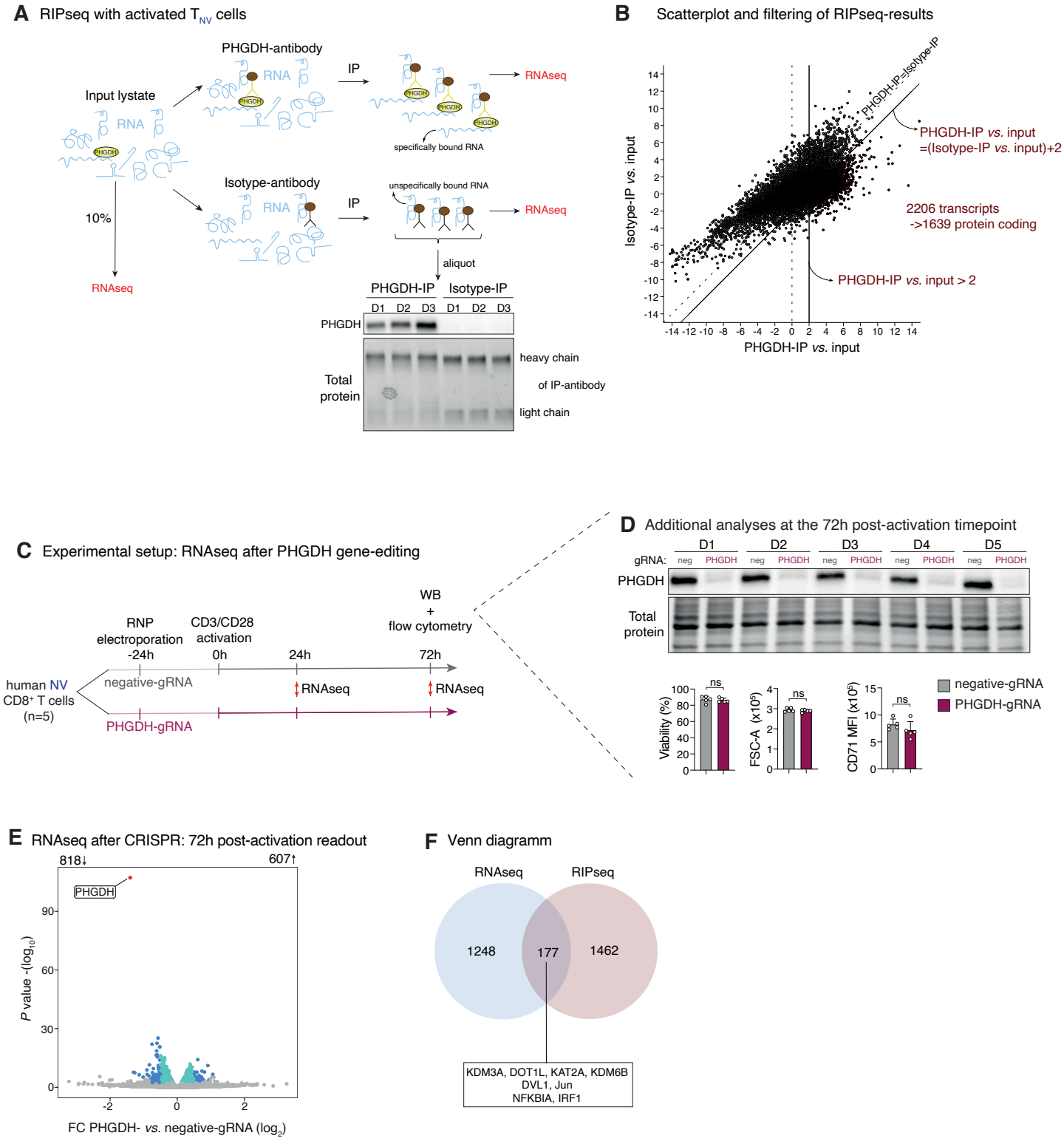

Figure 6. PHGDH functions as an RNA-binding protein in primary T cells.

Figure 6. PHGDH functions as an RNA-binding protein in primary T cells.

(**A**) Schematic of the RIPseq experiment. Sorted T_{NV} cells from three human donors were activated for 36h. After cell lysis, 10% of the lysate was put aside (input). Then, IP was performed for one half of the remaining lysate with a PHGDH-antibody and for the other half with an isotype-antibody. After the IP, which was verified by Wester blotting an aliquot of each sample, RNA was isolated and sequenced in parallel with the input sample.

(**B**) Scatterplot of RIPseq data showing for each transcript the enrichment over input achieved by PHGDH-IP (x-axis) *vs.* isotype-IP (y-axis). Pull-down was defined as specific when an RNA species was (i) enriched >2 fold in the PHGDH-IP over input, and (ii) enriched 2-times more in the PHGDH-IP compared to the isotype-IP.

(**C**) Schematic of the RNAseq experiment after CRISPR-Cas9 induced gene-editing of PHGDH. T_{NV} cells from five human donors were rested for 6h after the FACS-sort. For each donor, T_{NV} cells were either electroporated with negative-gRNA (non-targeting)- or PHGDH-gRNA (targeting) loaded Cas9 protein. After a resting and gene-editing period of 24h, cells were activated. RNA was isolated at the 24h and 72h post-activation timepoint and processed for sequencing.

(**D**) A fraction of the primary effector T cells (n=5 donors), which were used for RNA sequencing at the 72h post-activation timepoint, was subjected to further analysis: Western blotting for PHGDH confirmed depletion also at the protein level and flow cytometry was used to assess viability, blasting (FSC-A) and CD71 expression in negative-gRNA *vs.* PHGDH-gRNA treated cells.

(**E**) Volcano plot representation of differential transcript abundance in PHGDH containing *vs.* PHGDH depleted primary effector T cells at the 72h post-activation timepoint.

(**F**) Venn diagram of hits obtained by RNAseq- and RIPseq experiments. The overlap represents transcripts defined as PHGDH targets by RIPseq, which were also functionally responsive upon PHGDH depletion (RNAseq). Transcripts linked to the regulation of gene expression, development and survival are highlighted in the box.

All experiments were done with human primary cells. Data are represented as mean ± SD. Statistical significance was assessed by two-sided paired Student's *t*-test (**D**). See also Figure S6.

FC, fold change; FSC-A, forward scatter area; gRNA, guide RNA; IP, immunoprecipitation; KO, knock-out; ns, not significant; RIPseq, RNA immunoprecipitation followed by sequencing; RNAseq, RNA sequencing; RNP, ribonucleoprotein; SD, standard deviation; T_{NV}/NV, naïve $CD8^+$ T cells; WT, wildtype.

5. DISCUSSION

The opening finding of this study was that metabolic pruning, rather than metabolic flexibility, characterized human memory CD8$^+$ T cells at a transcript and proteome level, with loss of PHGDH being the most striking metabolic restriction. As a consequence of silencing PHGDH, memory T cells failed to acquire effector functions when extracellular serine was limiting, *in vitro* and *in vivo*. On a transcriptional level this functional paralysis was characterized by an upregulation of p53 target genes and a downregulation of cell cycle genes. Although metabolically disadvantageous for memory cells, silencing of PHGDH was a necessity for primary effector cells to properly contract and was found to be a hallmark of differentiated cells across various cell types and tissues. Aligning with the notion that PHGDH is involved in regulating differentiation, specific mutations in *PHGDH* cause severe differentiation problems leading to NLS – yet we demonstrate for one such mutation that enzymatic activity was largely unaffected. Together this led us to discover RNA-binding properties of PHGDH, and silencing of it emerged as a trade-off event, which had an impact on the abundance of transcripts implicated in determining cell fate.

CD8$^+$ T cells are required to function in heterogeneous and at times metabolically challenging microenvironments. To ensure optimal immune cell function, changes in nutrient availability need to be sensed and integrated with cellular processes, such as metabolic and transcriptional activity. Serine is a key anabolic AA serving as building block for protein synthesis and as a precursor for multiple molecules, including nucleic acids, lipids and glutathione (Newman and Maddocks, 2017; Yang and Vousden, 2016). Serine depletion had a profound impact on CD8$^+$ T cells, triggering a p53 centered stress response and cell cycle arrest. The molecular sensor of serine sufficiency remains to be identified. Studies in cancer cells suggest decreasing abundance of nucleotides, rather than direct sensing of serine, as a plausible driver of p53 activation (Maddocks et al., 2013; Pelletier et al., 2020). In cell lines, the p53-dependent DNA damage response represses transcription of Myc, thereby enabling rearrangement of the transcriptome away from anabolism towards restoration of homeostasis (Porter et al., 2017). We found that, in memory CD8$^+$ T cells, cooperation between p53 and Myc occurred through a post-transcriptional mechanism instead. It will be interesting to explore whether amplification of PHGDH, which is often observed in tumors (Locasale et al., 2011; Possemato et al., 2011; Rotondo et al., 2014; Zhang et al., 2017), is motivated by the need to maintain high Myc levels in serine low microenvironments.

In contrast to T_{EM} cells, Jurkat PHGDH^{KO} cells displayed reduced viability when cultured in absence of extracellular serine. Since p53 has been shown to promote viability under serine

starvation (Maddocks et al., 2013), this prompted us to assess p53 mutational status in our authenticated Jurkat T cell line. Surprisingly, none of the classical p53 missense mutations and only low abundance of the truncating nonsense mutation, which has been proposed to be responsible for p53 deficiency in Jurkat T cells was found (g.chr17:767495 C>A, p.R163*, Appendix A3B) (Gioia et al., 2018). However, by performing RNA- rather than whole-genome sequencing, we detected intron retention and premature termination codon formation caused by a synonymous mutation located in the related donor splice-site (g.chr17:7675994 C>G, p.T125T). Similar mutations of the last base of exons have emerged as functional hotspot causing aberrant splicing and p53 inactivation in cancerous cells from various origins (Jung et al., 2015). Despite a probable impact of nonsense mediate mRNA decay, this – for Jurkat T cells – undescribed mutation was detected at a higher frequency and lies upstream of the described heterozygous R163* mutation. We therefore suggest that the herein reported mutation is responsible for p53 deficiency of Jurkat T cells and underscore the possible impact a seemingly unimportant synonymous mutation can have.

Our adoptive transfer experiments revealed, that forced expression of PHGDH did not impact primary effector expansion, but prevented normal T cell contraction. This failure to undergo apoptosis and, probably, also normal differentiation, provided a new perspective on the NLS, which is characterized by features reminiscent of differentiation problems, such as facial dysmorphia, microcephaly and skeletal anomalies, as well as fetal growth restriction and ichthyosis. First described in 1971, only in 2014 the NLS has been linked to mutations in *PHGDH* – and proposed to represent the sever end of a spectrum of know serine-deficiency syndromes (Laxova et al., 1972; Neu et al., 1971; Shaheen et al., 2014). In favor of this proposition, mutations in other components of the serine synthesis pathway, *i.e.* PSAT1 and PSPH, have also been described to cause not only serine-deficiency, but in some instances phenotypes similar to NLS (Abdelfattah et al., 2020; Acuna-Hidalgo et al., 2014). However, neither serine levels nor enzymatic activity of PHGDH have been quantified in NLS-patients (de Koning, 2017) and, more importantly, our experiments demonstrate high residual catalytic activity and normal growth in absence of extracellular serine of cells containing an NLS causing mutation. The clinical features of NLS in conjuncture with our experimental data thus led us to discover PHGDH functioning as an RBP, plausibly contributing to normal and, when mutated at sites critical for RNA-binding, abnormal cell differentiation. NAD^+ abundance dictates PHGDH catalytic activity (Diehl et al., 2019), which in turn might be competing with its RNA-binding properties – as has been suggested for several metabolic enzymes moonlighting as RBPs (Kilchert et al., 2019). It is tempting to speculate that mutations in PSAT1 or PSPH may affect serine levels and NAD^+/NADH ratios such that PHGDH is forced

to be catalytically more active, which in turn may alter the enzymes RNA-binding properties. Understanding such potential regulatory circuits involving metabolic activities and moonlighting roles of enzymes affected by metabolic engagement, may eventually generate unifying models of diseases such as NLS. While basic principles of how RBPs impact specific cell functions have been derived from work in cell lines, this study provides evidence for a critical role of a non-canonical RNA–protein interaction in a primary human cell system – with conceptual relevance for enzymopathies more broadly. Detailed mechanistic interrogation of how specific RNA species that are bound by PHGDH impact and integrate with the overall, exceedingly complex, cellular network of RNA–protein interactions will rely on reductionist model systems. Our findings offer relevant clinical and biologic context for such studies.

GAPDH preferentially binds adenine-uridine-rich elements (AREs) (Nagy et al., 2000) and is thus classified as an adenine-uridine-binding protein (ARE-BP) (Garcin, 2019). Structural comparison of PHGDH with potential RNA-binding sites of GAPDH revealed notable similarities, indicating that PHGDH could be an ARE-BP as well. Binding of ARE containing RNA species to ARE-BPs determines stability of these transcripts (García-Mauriño et al., 2017; Roretz et al., 2011). Various stabilizing and destabilizing ARE-BPs have been described, and GAPDH, for example, can have opposite effects depending on the target RNA (White and Garcin, 2015). By cooperating or competing with other ARE-BPs, as well as microRNAs, a complex network determines the fate of an ARE containing transcript. Several cell-cycle genes, as well as immediate response genes, encode ARE containing transcripts (Roretz et al., 2011). By regulating stability of thousands of such RNAs, ARE-BPs represent key nodes in post-transcriptional gene regulation and allow coordination of functionally related RNAs – and therefore coordination of cellular processes such as cell fate transitions and development (Keene, 2007; Tan and Elowitz, 2014; Ye and Blelloch, 2014). While transcriptional and epigenetic regulation of T cell differentiation has been studied in much detail, the impact of post-transcriptional regulation by RBPs is less well understood, but its importance has been clearly demonstrated by genetic mouse models (Díaz-Muñoz and Turner, 2018; Salerno et al., 2020). Conditional deletion of the ARE-BP HuR (ELAV1) in thymocytes, for example, impairs T cell maturation, and whole-body inducible deletion causes rapid apoptosis selectively of hematopoietic progenitor cells, while sparing differentiated cells (Ghosh et al., 2009; Papadaki et al., 2009). Notably, both HuR and PHGDH deficient mice exhibit perinatal lethality, highlighting their role in embryonic development (Katsanou et al., 2009; Yoshida et al., 2004). Many mRNAs encoding proto-oncogenes or tumor-suppressor genes, such as Myc, Bcl2, VEGF or CCND1, are likewise subjected to ARE mediated RNA decay, and dysregulated expression and function of related ARE-BPs can promote tumor

progression (Hitti et al., 2016; Vlasova-St Louis and Bohjanen, 2017). Future work should explore the role of PHGDH also from the perspective of regulating these RNA species, as well as stemness related transcripts, in promoting malignant cell growth. Irrespective of PHGDH's precise role in the network of RBPs, our findings highlight the need to validate genetic hits in cancer screens with rescue experiments that not only are using the active enzyme, but also catalytic dead protein variants to probe for relevant moonlighting roles. It is interesting in this context to note that from the wealth of inhibitors of PHGDH enzymatic activity, none has progressed to advanced-stage clinical trials – likely due to lack of efficacy.

In summary, our unbiased screening approach identified serine auxotrophy of memory T cells and novel metabolic roles of p53 in primary human cells. We propose PHGDH to be an unrecognized RBP, reinforcing pathways known to be important for stemness, development and survival. Conceptually, our results reveal how different roles of PHGDH need to be balanced during T cell differentiation and highlight the intimate connection, including possible feedback loops, between intermediary metabolism and post-transcriptional gene regulation.

6. SUPPLEMENTARY INFORMATION

Inventory of Supplementary Information:

Figure S1. Related to Figure 1. Silencing of PHGDH is a major metabolic restriction of memory $CD8^+$ T cells.

Figure S2. Related to Figure 2. Memory $CD8^+$ T cells are serine auxotroph.

Figure S3. Related to Figure 3. Serine starvation induces a p53 centered stress response.

Figure S4. Related to Figure 4. Memory T cells depend on extracellular serine; effector T cell contraction requires silencing of PHGDH.

Figure S5. Related to Figure 5. PHGDH is downregulated in various differentiating cells and is an unappreciated RNA-binding protein – a potentially relevant role for the pathogenesis of the NLS.

Figure S6. Related to Figure 6. PHGDH functions as an RNA-binding protein in primary T cells.

A

RNAseq – comparing human CD8⁺ T_{EM} *vs.* T_{NV} cells

GO term enrichement analysis performed on:

(i) **all** differentially expressed transcripts: ↓↑

#	GO Processes	Enrichment p-value	# transcripts in category	# differentially expressed transcripts
1	positive regulation of biological process	6.8E-96	8426	2517
2	regulation of response to stimulus	1.3E-88	6076	1921
3	positive regulation of cellular process	9.8E-88	7388	2240
4	regulation of signaling	4.8E-78	4929	1595
5	negative regulation of biological process	6.0E-78	7384	2203
6	negative regulation of cellular process	6.7E-76	6624	2011
7	regulation of cell communication	8.6E-76	4885	1576
8	regulation of signal transduction	6.8E-73	4388	1438
9	regulation of intracellular signal transduction	4.2E-71	2551	938
10	cellular response to organic substance	1.8E-69	3824	1279
11	cellular process	7.6E-68	19158	4692
12	biological regulation	2.9E-67	16644	4200
13	response to organic substance	5.6E-66	4928	1552
14	regulation of cellular metabolic process	2.6E-65	8207	2348
15	cellular response to chemical stimulus	1.2E-64	4578	1458
16	regulation of metabolic process	1.6E-64	8863	2498
17	regulation of biological process	3.1E-64	15794	4015
18	regulation of cellular process	3.2E-64	14879	3825
19	cellular metabolic process	1.9E-63	9716	2690
20	response to stress	2.3E-63	5245	1622

(ii) transcripts with **decreased** abundance in T_{EM} cells: ↓

#	GO Processes	Enrichment p-value	# transcripts in category	# differentially expressed transcripts
1	cellular metabolic process	1.0E-31	9716	1163
2	regulation of metabolic process	3.1E-30	8863	1074
3	metabolic process	3.0E-29	10751	1250
4	nitrogen compound metabolic process	4.6E-29	8928	1075
5	organic substance metabolic process	7.2E-28	10026	1175
6	regulation of macromolecule metabolic process	2.2E-26	8177	989
7	primary metabolic process	2.5E-26	9559	1123
8	regulation of gene expression	3.4E-25	5957	760
9	negative regulation of biological process	7.6E-25	7384	903
10	regulation of primary metabolic process	1.4E-24	7952	958
11	cellular aromatic compound metabolic process	3.0E-24	3926	541
12	regulation of cellular metabolic process	6.0E-24	8207	980
13	cellular nitrogen compound metabolic process	1.3E-23	4479	598
14	heterocycle metabolic process	1.7E-23	3863	531
15	organic cyclic compound metabolic process	3.7E-23	4246	571
16	cellular component organization or biogenesis	8.8E-23	7729	927
17	macromolecule metabolic process	2.4E-22	7955	947
18	regulation of nitrogen compound metabolic process	7.9E-22	7698	919
19	cellular macromolecule metabolic process	4.5E-21	6575	803
20	nucleobase-containing compound metabolic process	6.6E-21	3615	493

(iii) transcripts with **increased** abundance in T_{EM} cells: ↑

#	GO Processes	Enrichment p-value	# transcripts in category	# differentially expressed transcripts
1	positive regulation of biological process	8.2E-91	8426	1627
2	regulation of response to stimulus	5.5E-88	6076	1273
3	positive regulation of cellular process	2.2E-79	7388	1443
4	regulation of signaling	3.0E-75	4929	1058
5	regulation of cell communication	7.5E-73	4885	1044
6	cellular response to organic substance	1.2E-72	3824	872
7	regulation of intracellular signal transduction	2.5E-71	2551	650
8	response to organic substance	2.8E-68	4928	1037
9	regulation of cellular component organization	3.9E-68	3502	806
10	response to stress	3.5E-67	5245	1083
11	regulation of signal transduction	3.9E-67	4388	948
12	cellular response to chemical stimulus	2.3E-66	4578	976
13	regulation of catalytic activity	4.7E-66	3227	754
14	regulation of molecular function	5.6E-66	4372	942
15	regulation of multicellular organismal process	2.6E-65	4592	975
16	positive regulation of molecular function	1.5E-64	2522	628
17	negative regulation of cellular process	7.5E-63	6624	1277
18	regulation of developmental process	8.1E-63	3879	853
19	positive regulation of response to stimulus	1.2E-61	3595	803
20	cell activation	1.7E-61	1595	450

Proteomics – comparing human CD8⁺ T_{EM} *vs.* T_{NV} cells

GO term enrichement analysis performed on:

(i) **all** differentially expressed proteins: ↓↑

#	GO Processes	Enrichment p-value	# proteins in category	# differentially expressed proteins
1	cellular process	2.4E-75	19158	1307
2	cellular metabolic process	1.5E-68	9716	855
3	cellular component biogenesis	7.7E-68	3864	469
4	cellular component organization or biogenesis	8.2E-65	7729	727
5	cellular nitrogen compound metabolic process	4.0E-64	4479	507
6	establishment of localization	3.0E-63	5979	610
7	metabolic process	7.4E-63	10751	900
8	mRNA metabolic process	1.3E-62	833	186
9	neutrophil degranulation	2.3E-62	626	160
10	cell activation	3.7E-62	1595	266
11	leukocyte degranulation	4.8E-62	660	164
12	neutrophil activation involved in immune response	6.2E-62	630	160
13	neutrophil activation	1.1E-61	640	161
14	neutrophil mediated immunity	2.7E-61	644	161
15	transport	3.0E-61	5812	594
16	granulocyte activation	3.5E-61	645	161
17	cellular aromatic compound metabolic process	6.1E-61	3926	459
18	heterocycle metabolic process	8.0E-61	3863	454
19	nucleobase-containing compound metabolic process	8.8E-61	3615	435
20	antigen processing and presentation of exogenous peptide antigen	1.2E-60	85	63

(ii) proteins with **decreased** abundance in T_{EM} cells: ↓

#	GO Processes	Enrichment p-value	# proteins in category	# differentially expressed proteins
1	cellular nitrogen compound metabolic process	1.8E-92	4479	408
2	heterocycle metabolic process	2.2E-92	3863	377
3	cellular aromatic compound metabolic process	3.2E-92	3926	380
4	nucleobase-containing compound metabolic process	1.1E-91	3615	363
5	organic cyclic compound metabolic process	1.5E-87	4246	389
6	nucleic acid metabolic process	2.6E-87	2946	320
7	mRNA metabolic process	4.6E-83	833	169
8	cellular metabolic process	1.7E-81	9716	602
9	RNA metabolic process	1.9E-77	2172	260
10	RNA processing	2.1E-76	1035	179
11	gene expression	5.0E-74	2676	285
12	ribonucleoprotein complex biogenesis	1.2E-73	561	133
13	organic substance metabolic process	4.4E-70	10026	593
14	metabolic process	5.7E-70	10751	617
15	nitrogen compound metabolic process	8.7E-70	8928	554
16	primary metabolic process	5.0E-69	9559	575
17	macromolecule metabolic process	2.5E-57	7955	494
18	RNA splicing	8.0E-52	465	101
19	cellular process	1.2E-50	19158	807
20	cellular component biogenesis	3.4E-48	3864	302

(iii) proteins with **increased** abundance in T_{EM} cells: ↑

#	GO Processes	Enrichment p-value	# proteins in category	# differentially expressed proteins
1	APAP of exogenous peptide antigen via MHC class I, TAP-ind.	3.8E-82	85	62
2	APAP of endogenous peptide antigen via MHC class I	1.9E-77	108	65
3	APAP of endogenous peptide antigen	4.6E-77	109	65
4	APAP of endogenous antigen	1.4E-74	121	66
5	APAP of end. peptide antigen via MHC class I via ER path., TAP-ind.	1.9E-74	97	61
6	APAP of peptide antigen via MHC class Ib	6.9E-74	103	62
7	APAP of endogenous peptide antigen via MHC class Ib	3.2E-73	100	61
8	APAP of endogenous peptide antigen via MHC class I via ER path.	3.2E-73	100	61
9	APAP via MHC class Ib	4.1E-73	115	64
10	immune system process	2.2E-72	4160	287
11	positive regulation of T cell mediated cytotoxicity	5.7E-72	135	67
12	regulation of T cell mediated cytotoxicity	2.5E-70	147	68
13	positive regulation of leukocyte mediated cytotoxicity	1.4E-68	188	73
14	vesicle-mediated transport	1.5E-68	2547	219
15	cell activation	4.2E-68	1595	174
16	APAP of exogenous peptide antigen via MHC class I, TAP-dep.	2.8E-67	173	70
17	positive regulation of cell killing	1.7E-65	204	73
18	APAP of peptide antigen via MHC class I	3.8E-65	230	76
19	regulation of T cell mediated immunity	5.9E-65	207	73
20	APAP of exogenous peptide antigen via MHC class I	8.2E-65	185	70

APAP, Antigen processing and presentation

Figure S1. Related to Figure 1. Silencing of PHGDH is a major metabolic restriction of memory CD8⁺ T cells.

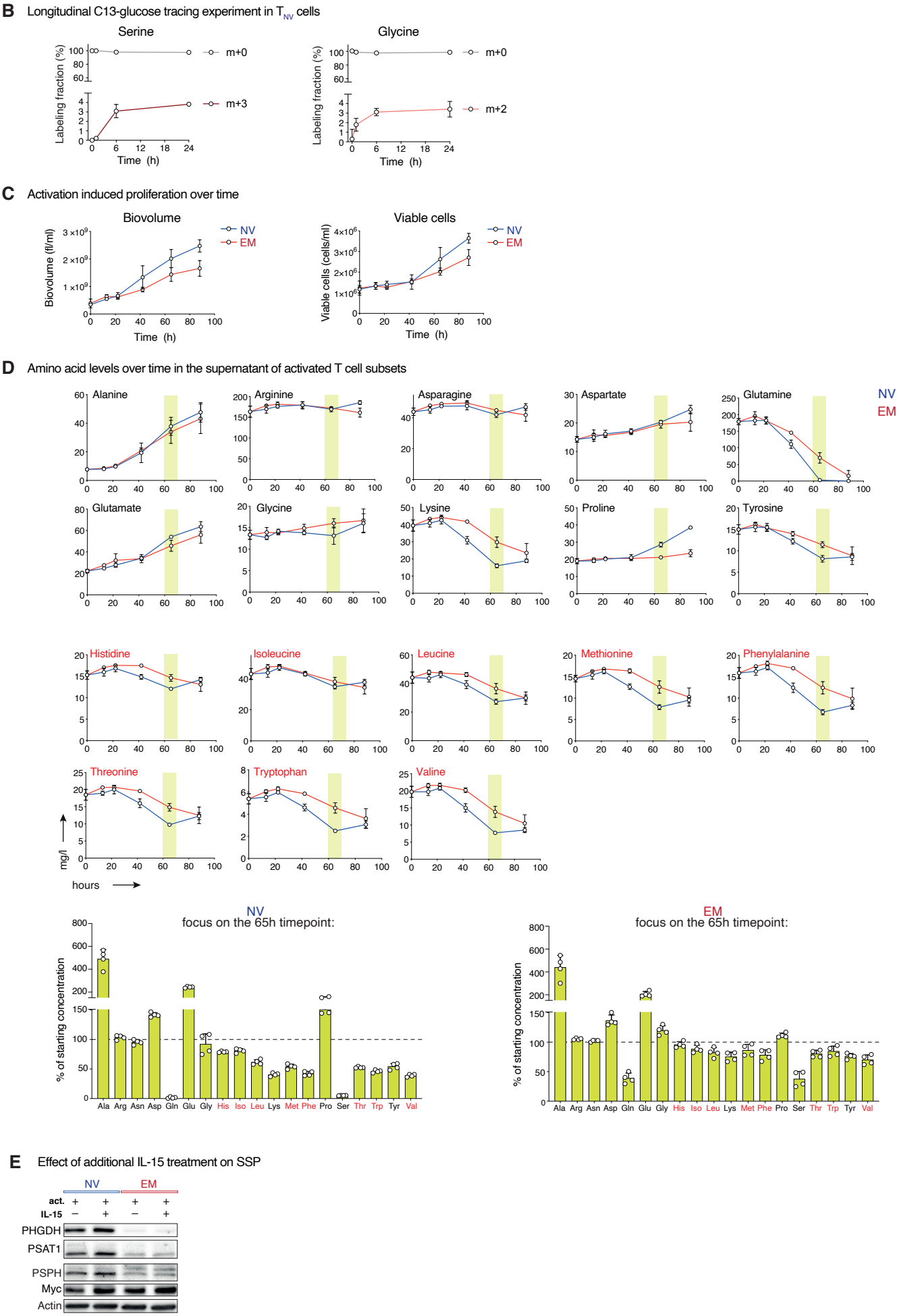

Figure S1. Related to Figure 1. Silencing of PHGDH is a major metabolic restriction of memory CD8⁺ T cells.

F Gene tracks for human CD8⁺ T cell subsets based on ChIPseq data

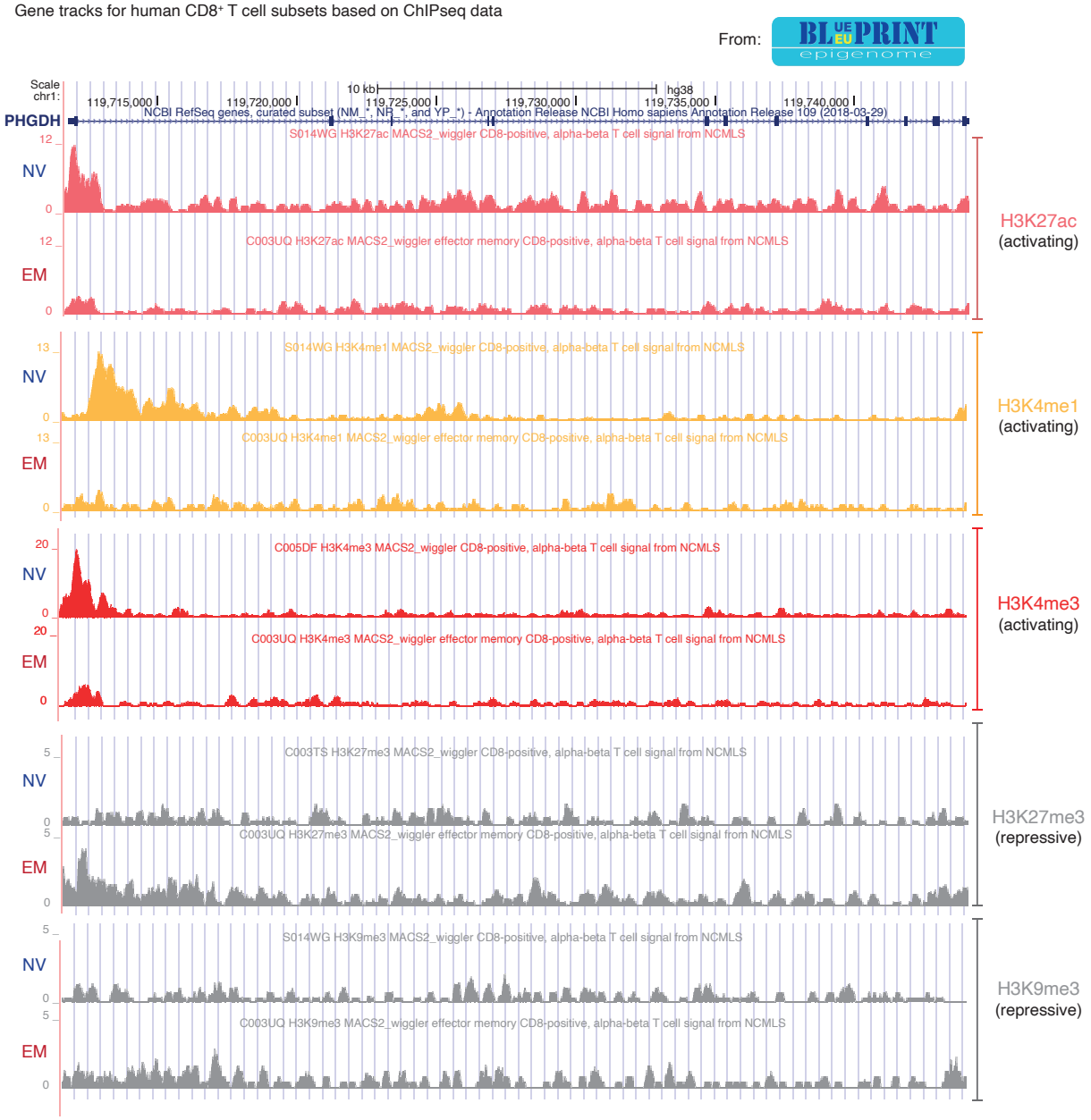

G

Figure S1. Related to Figure 1. Silencing of PHGDH is a major metabolic restriction of memory CD8⁺ T cells.

Figure S1. Related to Figure 1. Silencing of PHGDH is a major metabolic restriction of memory CD8+ T cells.

(**A**) Tables show biological processes overrepresented among differentially expressed transcripts/proteins between freshly sorted human T_{NV} and T_{EM} cells based on RNAseq (left side, red) and proteomics data (right side, violet). Specifically, GO term enrichment analysis was performed on (i) all differentially expressed transcripts/proteins, (ii) on transcripts/proteins with decreased abundance in T_{EM} cells compared to T_{NV} cells and (iii) on transcripts/proteins with increased abundance in T_{EM} cells compared to T_{NV} cells. From each analysis, the 20 biological processes with lowest p-values are shown in a ranked order. From MetaCore (Clarivate Analytics).

(**B**) Stable isotope tracing experiment in T_{NV} cells (n=2), where 13C-glucose was added 10min prior activation at the 0h time point. Fractional enrichment of intracellular m+3 serine (left) and m+2 glycine (right) isotoplogues are shown over time. Data are normalized to cell number and corrected for natural abundance of carbon 13.

(**C**) Proliferation of T_{NV} (blue) and T_{EM} (red) cells in media, where AA levels were measured (Figure 1G, S1D). Biovolume (left) and number of viable cells (right) were determined over time with a CASY-cell counter. Indicated T cell subsets were activated at the 0h time point by CD3/CD28 ligation (n=4).

(**D**) Top: Supernatant of activated T cell subsets (n=4) was collected at indicated time points post-activation. Media AA levels were measured by LC-MS/MS – reflecting consumption and excretion. Bottom: Bar graph shows AA levels at the 65h time point post-activation relative to the starting concentration. Classical non-essential AA are labeled in black, whereas classical essential AA are labeled in red.

(**E**) Western blot of enzymes involved in serine biosynthesis and Myc in T cell subsets activated by CD3/CD28 ligation for 24h in presence or absence of additional IL-15 (100ng/ml).

(**F**) Genome browser view showing the distribution of selected, epigenetically relevant histone 3 (H3) modifications across the *PHGDH* gene in human T_{NV} and T_{EM} cells. Gene tracks were obtained by importing ChIPseq data from the BLUEPRINT consortium (Adams et al., 2012) into the UCSC genome browser. Track Hub URL:
http://ftp.ebi.ac.uk/pub/databases/blueprint/releases/current_release/homo_sapiens/hub/hub.txt

(**G**) Top: Normalized plot of CpG methylation around the first intron of *PHGDH* (hg19: chr1:120,255,000-120,256,000) in human T cell subsets. Whole genome bisulfite sequencing data was accessed over the gene expression omnibus (GSE9887, Abdelsamed et al., 2017) and visualized with a Shiny script in R. Bottom: UCSC genome browser view of ENCODE transcription factor binding tracks (ChIPseq data) at the identical chromosomal coordinates (hg19: chr1:120,255,000-120,256,000).

All experiments were done with human primary cells. Data are represented as mean ± SD.

13C-glucose, uniformly labeled carbon 13 glucose; AA, amino acid; chr1, chromosome 1; ChIPseq, Chromatin immunoprecipitation-sequencing; CpG, cytosine-phosphate-guanine; GO, gene ontology; hg19, Human genome assembly GRCh37 from Genome Reference Consortium; H3, histone 3; LC-MS/MS, liquid chromatography with tandem mass spectrometry; RNAseq, RNA-sequencing; UCSC, University of California Santa Cruz; SSP, serine synthesis pathway; T_{NV}/NV, naïve CD8+ T cells; T_{EM}/EM, effector memory CD8+ T cells.

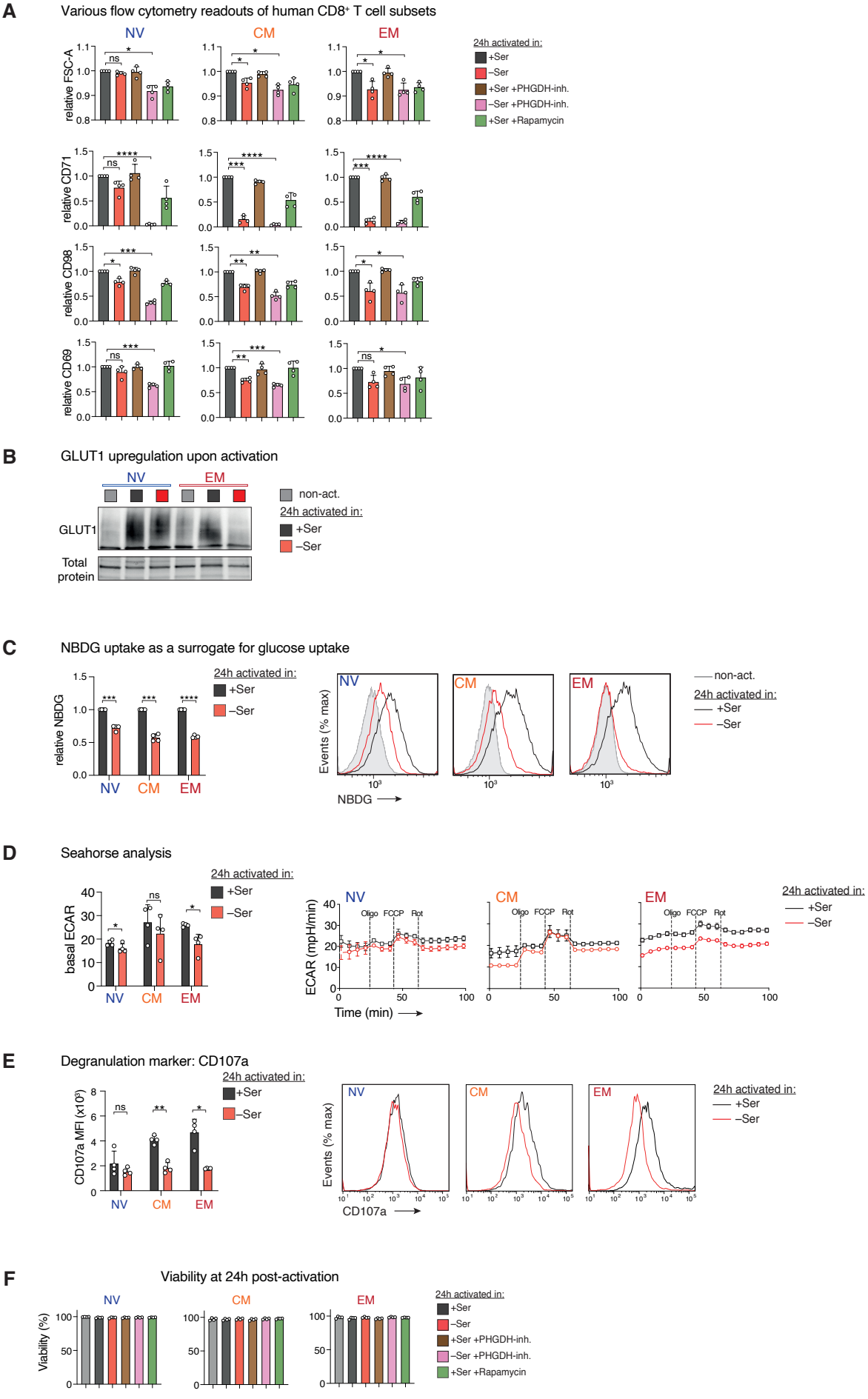

Figure S2. Related to Figure 2. Memory CD8⁺ T cells are serine auxotroph.

Figure S2. Related to Figure 2. Memory $CD8^+$ T cells are serine auxotroph.

(**A**) Flow cytometry measuring FSC-A as a surrogate marker for cell size and surface expression of various clusters of differentiation (CD71, CD98 and CD69) on T cell subsets activated under indicated conditions. Due to donor-donor variability values are presented as fold change of the +Ser condition (n=4).

(**B**) Western blot for GLUT1 under indicated conditions. Total protein staining was performed using stain free technology.

(**C**) Human T cell subsets were activated for 24h under indicated conditions and exposed to NBDG during the last 45min. Uptake of this glucose-analogue was assessed by flow cytometry and shown is a quantification (left) and representative histograms (right)(n=3).

(**D**) Basal extracellular acidification rate (ECAR) of T cell subsets activated as indicated (n=4). Quantification (left), representative metabolic flux experiment (right).

(**E**) Expression of CD107a on T cell subsets activated as indicated (n=3). Quantification (left), representative histograms (right).

(**F**) Viability of T cell subsets at 24h post-activation assessed by a flow cytometry based viability dye (n=4).

All experiments were done with human primary cells. Data are represented as mean ± SD. Statistical significance was assessed by one-way analysis of variance (ANOVA) (**A**), or two-sided paired Student's *t*-test (**C**–**E**). $*P < 0.05$, $**P < 0.01$, $***P < 0.001$, $****P < 0.0001$, ns, not significant.

ECAR, extracellular acidification rate; FSC-A, forward scatter area; GLUT1, glucose transporter 1; NBDG, [N-(7-nitrobenz-2-oxa-1,3-diazol-4-yl) amino]-2-deoxy-D-glucose; Ser, serine; T_{NV}/NV, naïve $CD8^+$ T cells; T_{CM}/CM, central memory $CD8^+$ T cells; T_{EM}/EM, effector memory $CD8^+$ T cells.

A GO term analysis of differentially expressed transcripts in T_{EM} cells activated in -Ser *vs.* +Ser

#	GO Processe Networks	Enrichment p-value	# transcripts in category	# differentially expressed transcripts
1	Cell cycle_S phase*	8.0E-29	148	124
2	Cell cycle_G2-M*	2.0E-18	206	143
3	Cell cycle_Mitosis*	9.9E-18	179	127
4	DNA damage_Checkpoint*	8.4E-16	124	93
5	Cell cycle_Core*	9.1E-15	118	88
6	Proteolysis_Ubiquitin-proteasomal proteolysis	2.1E-14	166	114
7	DNA damage_DBS repair*	3.3E-14	116	86
8	Apoptosis_Apoptotic nucleus	1.0E-13	161	110
9	Cell cycle_G1-S*	6.5E-13	162	109
10	Transcription_Chromatin modification	4.8E-12	126	88
11	Transcription_mRNA processing	6.1E-12	160	106
12	Cytoskeleton_Regulation of cytoskeleton rearrangement	1.7E-11	183	117
13	DNA damage_BER-NER repair*	5.9E-11	104	74
14	Protein folding_Folding in normal condition	7.7E-11	119	82
15	Translation_Translation initiation	3.1E-10	171	108
16	DNA damage_MMR repair*	3.6E-10	59	47
17	Immune response_Antigen presentation	8.8E-10	197	120
18	Cell cycle_Meiosis*	3.3E-09	108	73
19	Immune response_TCR signaling	3.4E-09	174	107
20	Cell cycle_G1-S Interleukin regulation*	5.9E-09	128	83

*= terms connected to cell cycle *= terms connected to DNA damage

B Cell cycle analysis in primary T cells:

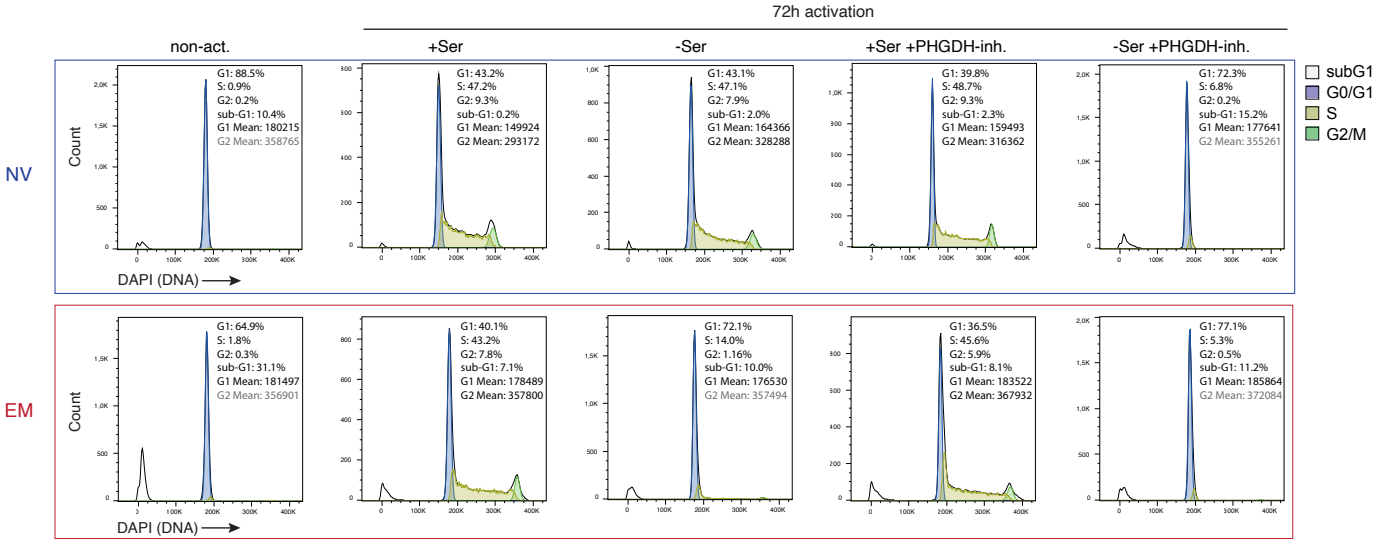

Summary of n=4:

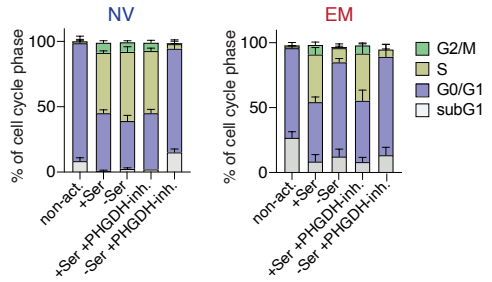

C

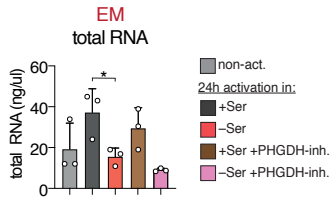

D

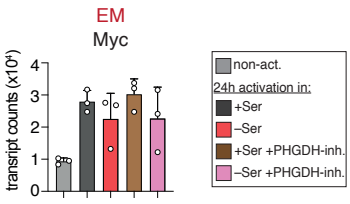

F

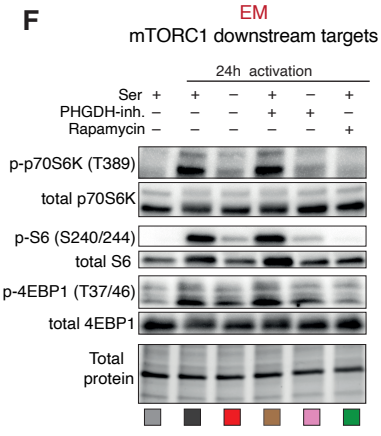

E

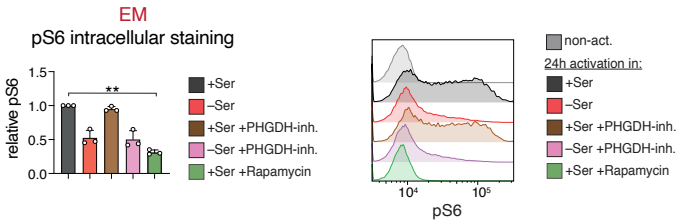

Figure S3. Related to Figure 3. Serine starvation induces a p53 centered stress response.

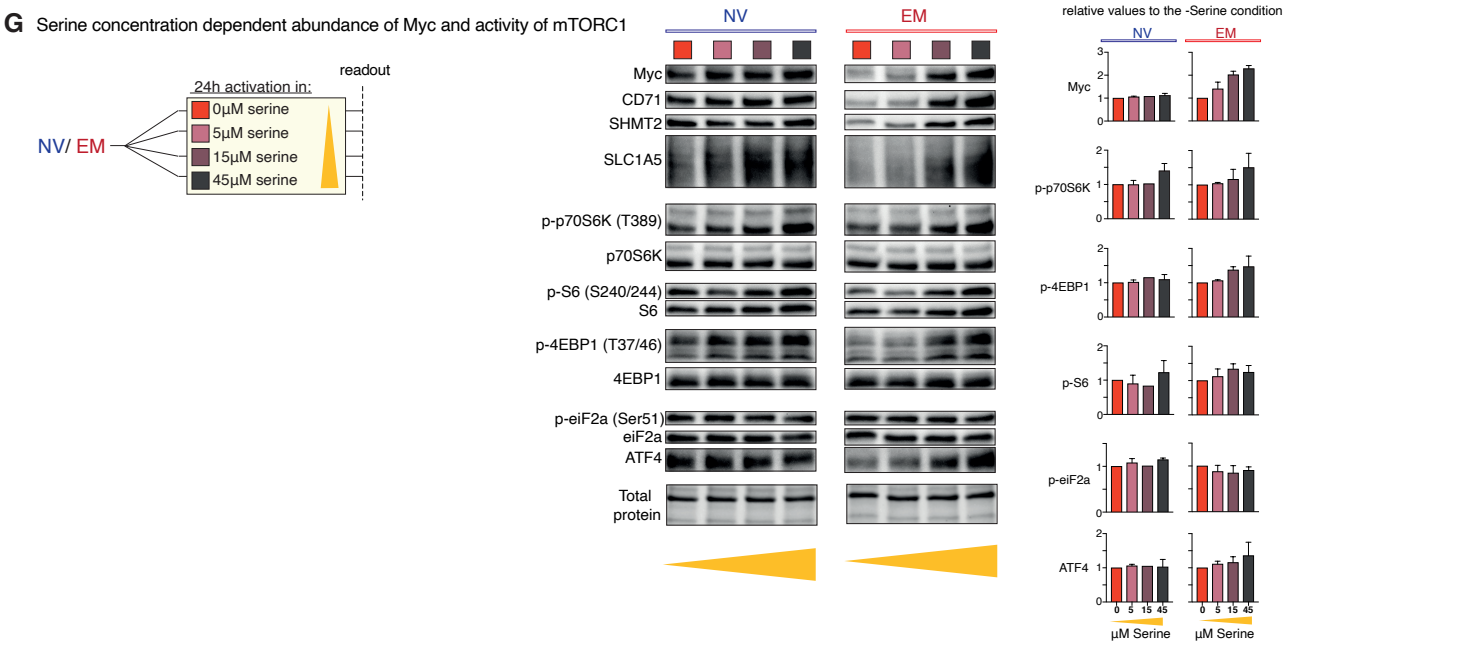

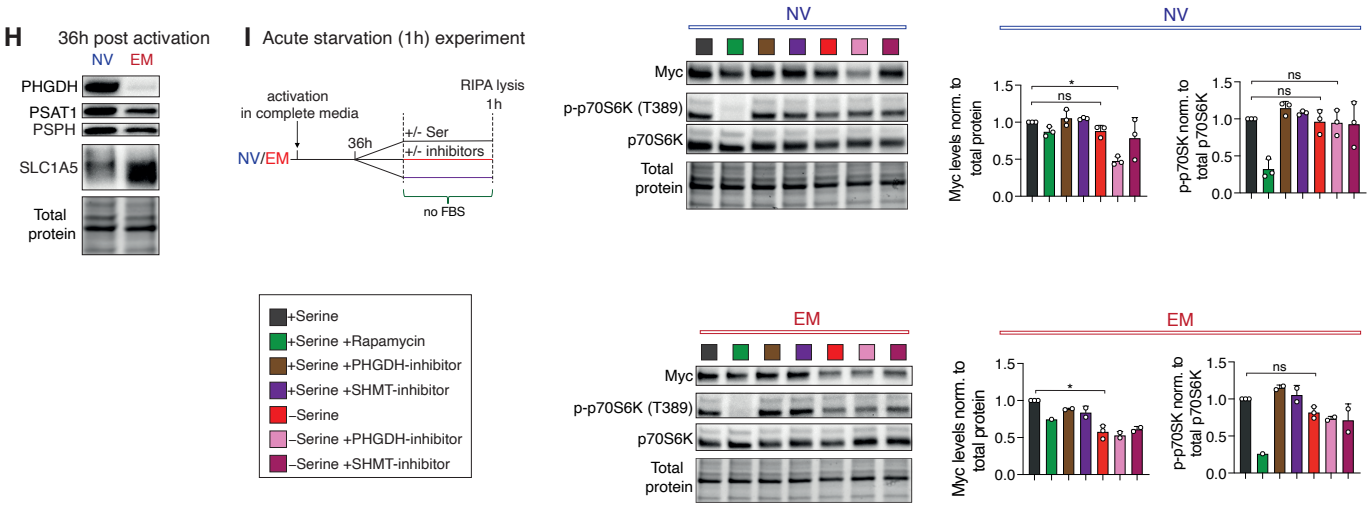

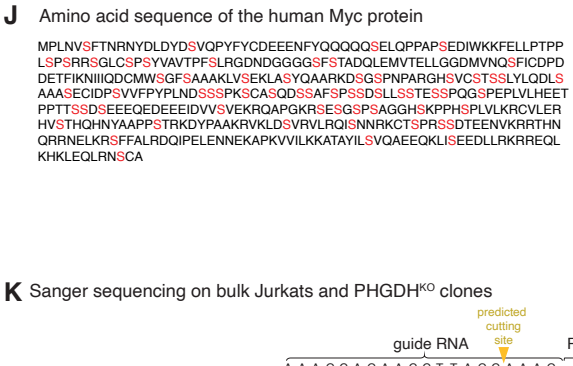

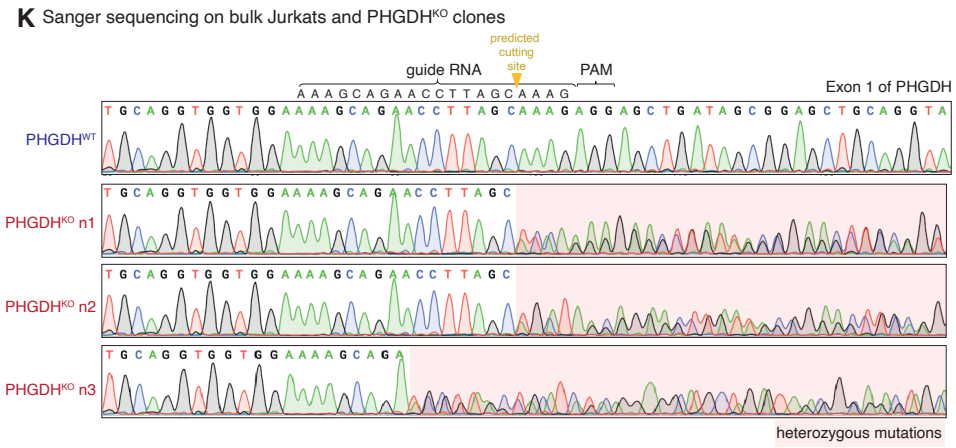

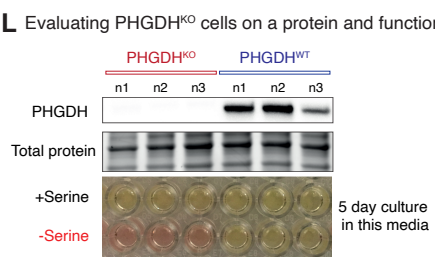

Figure S3. Related to Figure 3. Serine starvation induces a p53 centered stress response.

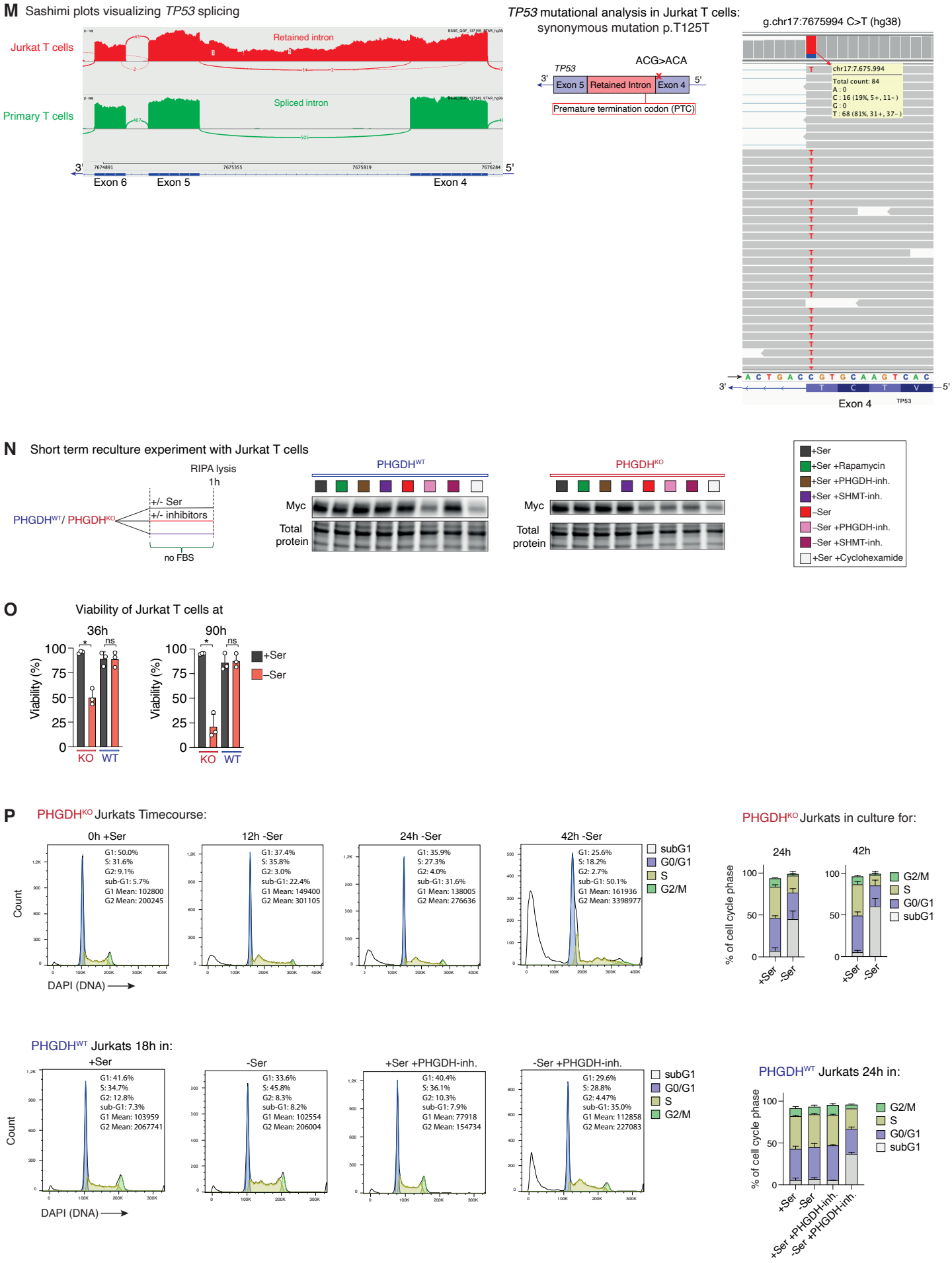

Figure S3. Related to Figure 3. Serine starvation induces a p53 centered stress response.

Figure S3. Related to Figure 3. Serine starvation induces a p53 centered stress response.

(**A**) GO term analysis on DEGs based on the RNAseq experiment among T_{EM} cells activated in absence *vs.* presence of serine (n=3). The 20 GO processes networks with lowest p-values are shown and terms linked to cell cycle/DNA-damage response are labeled with a yellow/red asterisk, respectively. From MetaCore (Clarivate Analytics).

(**B**) T cell subsets were left unstimulated or were activated for 72h in indicated conditions, subjected to DAPI staining and analyzed by flow cytometry. The curve fitting and the percentage of cells in G0/G1, S and G2/M phases of the cell cycle as well as in the sub-G1 area were determined by using the FlowJo 7.2 software (Tree Star Inc). These analyses were performed after exclusion of cell debris and activation beads, but without performing a pre-gating on viable cells. The upper part shows representative histograms of DNA content stained by DAPI in T_{NV} and T_{EM} cells cultured under indicated conditions. The summary bar graphs combine results obtained from cell cycle analyses of T cell subsets from four different human donors.

(**C**) Fluorometric measurement of total RNA levels of T_{EM} cells (n=3) cultured under indicated conditions, where the same amount of cells was plated at the beginning of the experiment.

(**D**) Myc transcript counts in T_{EM} cells cultured as indicated (extracted from RNAseq experiment described in **Figure 3**) (n=3).

(**E**) Quantification of intracellular flow cytometry staining for phosphor-S6 (pS6). MFIs are presented as fold change to values obtained in T_{EM} cells activated in presence of serine (same cells as in Figure 3G – pS6 assessed to quantify efficiency of rapamycin).

(**F**) Western blot probed for the phosphorylation and total abundance of mTORC1 downstream targets in T_{EM} cells cultured as indicated. Blots are representative of n=2 independent experiments.

(**G**) Left: Schematic of the experimental design. T cell subsets were cultured for 10min in media containing increasing serine concentrations before addition of activation beads. Middle: Western blot for Myc and proteins induced by Myc, as well as mTORC1 targets (each lysate was loaded four times). Right: Quantification of three experiments with cells from n=3 independent donors. Myc and ATF4 were normalized to total protein, phosphorylated proteins to their unphosphorylated forms and displayed relative to the 0µM serine condition.

(**H**) Western blot stained for SSP enzymes and SLC1A5 in activated (36h)of T cell subsets.

(**I**) Left: Schematic of the experimental design. T cell subsets were activated in full media for 36h and distributed into several tubes after a PBS wash. Subsequently, cells were resuspended in pre-warmed media containing serine and inhibitors as indicated (in absence of dFBS). After 1h at 37°C, cells were harvested by centrifugation and directly lysed in ice-cold RIPA buffer. Resulting Western blots of Myc and phosphor-p70S6K (p-p70S6K) (middle) and their quantification (right) normalized to total protein or total p70S6K, respectively (n=3 for T_{NV} cells). Due to limited numbers of T_{EM} cells certain donors, n=3 was only possible for the +Ser and -Ser condition, which lead to statistical testing by Student's *t*-test instead of one-way ANOVA.

(**J**) AA sequence of human Myc protein with serine labeled in red (from: https://www.uniprot.org/uniprot/P01106). The table lists the relative abundance of each AA in Myc ranked from high to low abundant.

(**K**) Chromatograms from Sanger sequencing of genomic DNA at the *PHGDH* Cas9 target loci in bulk Jurkat T cells ($PHGDH^{WT}$) and three CRISPR-Cas9 generated $PHGDH^{KO}$ clones. The presence of double peaks after Cas9 induced DNA double-strand breaks, indicates formation of different insertions and deletions (indels) on different alleles (heterozygous mutations). Double peaks also argue in favor of the single cell clonality of the generated cell lines.

(**L**) Upper panel: Western blot of PHGDH expression in $PHGDH^{KO}$- and $PHGDH^{WT}$ clones. Lower panel: Corresponding acidification of serine replete *vs.* deplete media by the respective clones after 5 days of culture.

(**M**) Left: RNAseq analysis of Jurkat T cells and primary T_{NV} cells presented as a 'sashimi plot' displaying read coverage and reads that map to exon-exon junctions (represented by the numbers in the arches). At the bottom, the chromosomal coordinates and exons of *TP53* are illustrated. Right: Screenshot from the IGV browser (Robinson et al., 2011) showing the last-base exonic mutation responsible for the intron retention. This synonymous mutation was found in the 5' splice site therefore likely interrupting recognition by the spliceosome as has been described for other cells (Jung et al., 2015). Of note, reads with the wild-type sequence were exon-exon spanning (normal splicing) whereas reads containing the mutation preferentially spanned the exon-intron junction (aberrant splicing). Similar results were obtained by two additional poly-A enriched mRNAseq experiments on Jurkat T cells.

(**N**) Western blot for Myc in $PHGDH^{WT}$ and $PHGDH^{KO}$ cells after 1h culture in indicated conditions (analogous to experiment with primary T cells in Figure S3I).

(**O**) Viability of $PHGDH^{WT}$ and $PHGDH^{KO}$ Jurkat T cells cultured in ±Ser for indicated timepoints. Percentage of viable cells was assessed by flow cytometry with a cell permeable dye (n=3).

(**P**) Top left: Representative histograms of DNA content assessed by DAPI staining of permeabilized $PHGDH^{KO}$ Jurkat T cells. Different time points after culturing the cells in absence of serine are shown. The curve fitting and the percentage of cells in G0/G1, S and G2/M phases of the cell cycle as well as in the sub-G1 area were determined by using the FlowJo 7.2 software (Tree Star Inc). Top right: Summary bar graph of percentage of cells in indicated cell cycle phases at two different time points obtained by using three different $PHGDH^{KO}$ clones. Bottom left: Representative histogram of DNA content assessed by DAPI staining of $PHGDH^{WT}$, serine de novo synthesis capable, Jurkat T cells cultured under indicated conditions for 18h. Bottom right: Summary bar graph of the percentage of cells in each cell-cycle phase of three independent experiments (n=3).

Data are represented as mean ± SD. Statistical significance was assessed by one-way analysis of variance (ANOVA) (**C,D, I** for T_{NV} cells), or two-sided paired Student's *t*-test (**I** for T_{EM} cells, **O**). $*P < 0.05$, $**P < 0.01$; ns, not significant.

AA, amino acid; Cas9, CRISPR associated protein 9; CRISPR, clustered regularly interspaced short palindromic repeats; DAPI, 4′,6-diamidino-2-phenylindole; DEGs, differentially expressed genes; FBS, fetal bovine serum; IGV, Integrative Genomics Viewer; Indel, insertion and deletions; MFI, mean fluorescence intensity; mTORC1, mammalian target of rapamycin complex 1; PAM, protospacer adjacent motif; PBS, phosphate buffered saline; RIPA buffer, radioimmunoprecipitation assay buffer; RNAseq, RNA sequencing; T_{NV}/NV, naïve $CD8^+$ T cells; T_{EM}/EM, effector memory $CD8^+$ T cells.

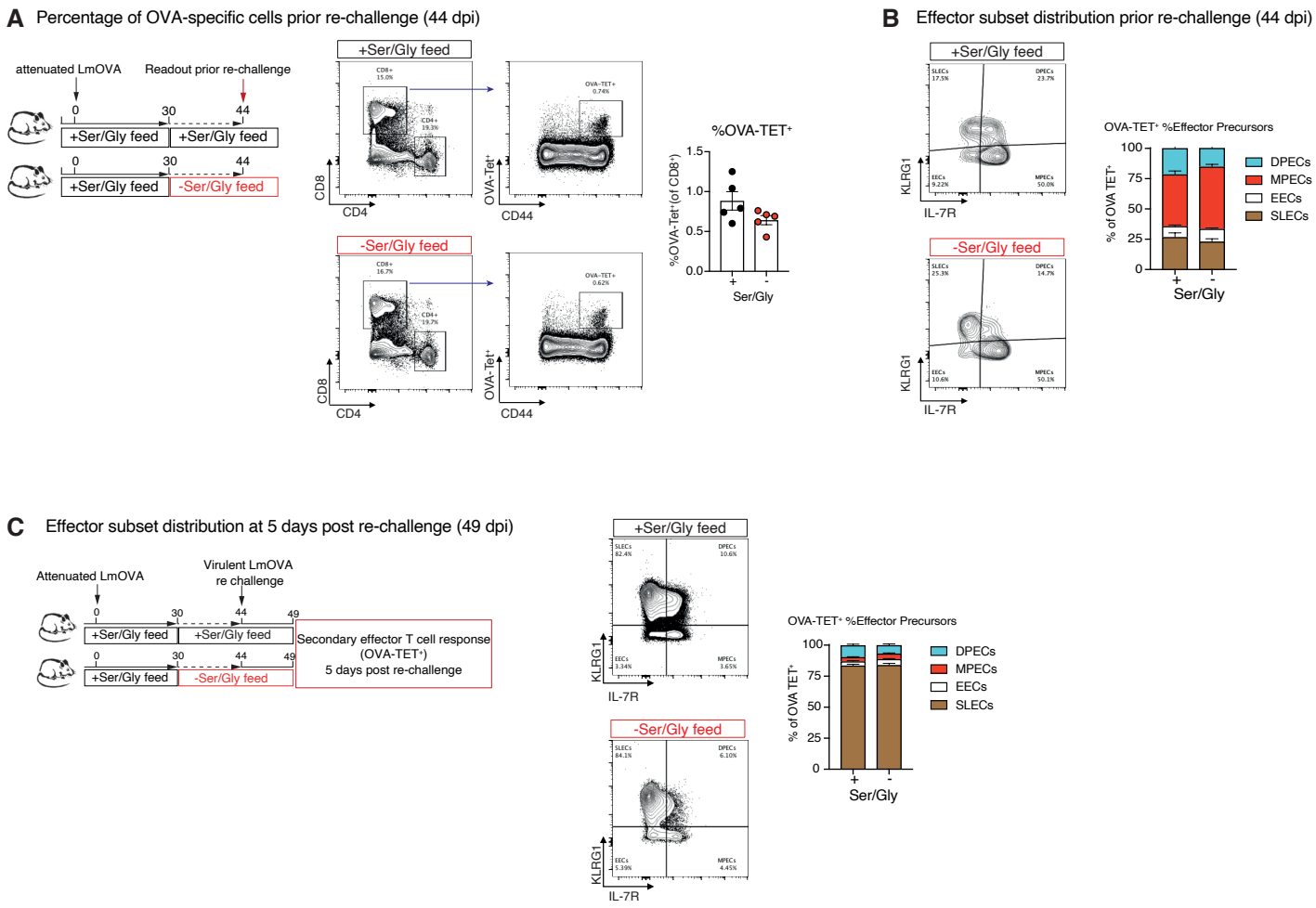

Figure S4. Related to Figure 4. Memory T cells depend on extracellular serine; effector T cell contraction requires silencing of PHGDH.

Figure S4. Related to Figure 4. Memory T cells depend on extracellular serine; effector T cell contraction requires silencing of PHGDH.

(**A**) Left: Experimental scheme of the flow cytometry readout of splenocytes from LmOVA-infected mice at 44 dpi, after being 2 weeks on the +/-Ser/Gly feed. Middle: Representative contour plots illustrating gating strategy on $CD8^+$ OVA-specific memory T cells based on CD44 expression and OVA-tetramer (OVA-Tet) positivity. Right: Summary bar graph of percentage of T cells which have a TCR recognizing OVA (=$OVA\text{-}Tet^+$) of all $CD8^+$ T cells (n=5).

(**B**) Related to Figure S4A. Left: Representative flow cytometry plots of IL-7R *vs.* KLRG1 expression on $OVA\text{-}Tet^+$ $CD8^+$ T cells at 44 dpi. Right: Summary bar graph showing the percentage of SLECs, MPECs, EECs and DPECs of OVA-specific $CD8^+$T cells in spleens of LmOVA infected mice prior to re-challenge.

(**C**) Related to Figure 4E. Left: Schematic illustrating the timepoint of readout, which is at 5 days post-secondary infection (re-challenge) and 49 days post-primary infection. Middle: Representative flow cytometry plots of IL-7R *vs.* KLRG1 expression at the peak of secondary effector T cell expansion. Right: Summary bar graph of percentage of the effector precursors SLECs, MPECs, EECs and DPECs of OVA-specific $CD8^+$ T cells.

(**D**) Splenocytes were isolated at 5 days post-re-challenge and activated *in vitro* with OVA-peptide in presence of monensin. Left: Representative flow cytometry plots of INFγ, TNF and GZMB *vs.* CD44 staining for $OVA\text{-}Tet^+$ $CD8^+$ T cells of mice under indicated diet. Right: Percentage of cells stained positive for indicated cytokines (top) and their absolute numbers (bottom).

(**E**) Related to Figure 4H,I. Intracellular INFγ staining on $Thy1.1^+$ $CD8^+$ OT-I T cells expressing EV or OE-PHGDH. These cells have been adoptively transferred into Thy1.2 mice and are at 7 dpi with LmOVA. Left: Summary bar graphs of percentage of $INF\gamma^+$ cells among all $Thy1.1^+$ cells, their absolute numbers and geometric Mean (gM) of their INFγ expression. Right: Representative flow cytometry plots of CD44 *vs.* INFγ staining of EV and OE-PHGDH cells (n=4). As a control, non-stimulated cells are shown as well.

Data are represented as mean ± SEM. Statistical significance was by two-sided unpaired Student's *t*-test. $*P < 0.05$, $**P < 0.01$; ns, not significant.

Dpi, days post infection; DPECs, double-positive effector cells; EECs, early effector cells; EV, empty vector; FSC-A, forward scatter area; GFP, green fluorescent protein; Gly, glycine; GZMB, Granzyme B; INFγ, Interferon γ; LmOVA, listeria monocytogenes strain expressing OVA; MPECs; memory-precursor effector cells; OE, overexpression (of PHGDH); OVA, ovalbumin; OVA-Tet, ovalbumin tetramer; Ser, Serine; SLECs, short-lived effector cells; TCR, T-cell receptor; TNF, Tumor necrosis factor.

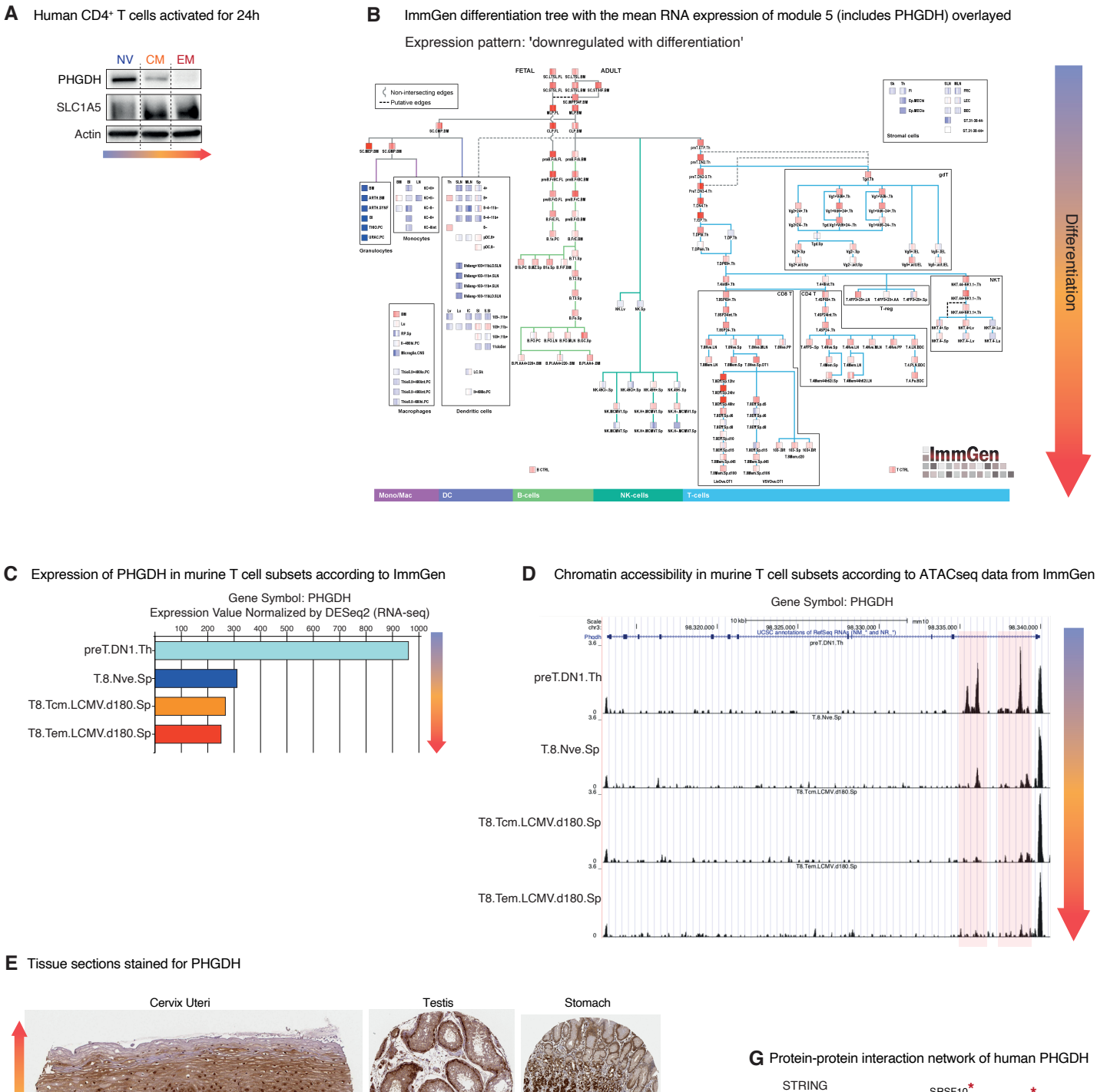

Figure S5. Related to Figure 5. PHGDH is downregulated in various differentiating cells and is an unappreciated RNA-binding protein – a potentially relevant role for the pathogenesis of the NLS.

Figure S5. Related to Figure 5. PHGDH is downregulated in various differentiating cells and is an unappreciated RNA-binding protein – a potentially relevant role for the pathogenesis of NLS.

(**A**) Western blot for PHGDH and SLC1A5 among 24h activated human $CD4^+$ T cell subsets. The juxtaposed lanes, separated by dashed lines, are from a single membrane which was equally processed in terms of brightness and contrast. Data are representative of two independent experiments.

(**B**) The ImmGen database is an RNAseq atlas of murine immune cells – sequenced at different stages during development. The interface allows determination of gene expression patterns over all displayed cell types (indicated at the lowest end of the figure), while differentiation stage increases from top to bottom. When investigating the expression pattern of PHGDH across all ImmGen cell-types, it appears in a module of co-regulated genes characterized as 'downregulated with differentiation' (coarse module 5, fine module 41). The mean expression of this module is projected on the ImmGen differentiation tree (red=high expression, blue = low expression).

(**C**) PHGDH mRNA expression among splenic (Sp) murine T cell subsets (identical to Figure 4A), with addition of thymic (Th) double-negative (DN) precursor T cells. Data was extracted from the ImmGen database and annotations were replicated from there.

(**D**) Gene tracks showing chromatin accessibility around *PHGDH* in indicated murine T cell subsets (increasing differentiation stage from top to bottom according to linear differentiation model). Differentially accessible regions are highlighted by a red box. Tracks were obtained by loading ATACseq data extracted from the ImmGen database into the USCS genome browser, while annotations were replicated from there.

(**E**) Images are reprinted from the human protein atlas (Uhlen et al., 2010) and represent different tissues stained immunohistochemically for PHGDH (brown color; antibody CAB068216). The three tissue sections consist of stratified epithelium, where cells differentiate from the basal to outer layers.

(**F**) Chromatograms from Sanger sequencing of lentiviral expression plasmids to verify missense mutations of *PHGDH* variants. These plasmids were used to generate lentivirus in order to re-introduced the following *PHGDH* variants into $PHGDH^{KO}$ Jurkat T cells: wildtype ($PHGDH^{WT}$), catalytic dead (R236E; $PHGDH^{dead}$) and a mutation known to cause NLS (R163Q; $PHGDH^{NLS}$).

(**G**) Protein-protein interaction network of human PHGDH based on the STRING database (Szklarczyk et al., 2017). Beside the SSP enzymes, various RNA-binding proteins (RBPs), labeled with an red asterisk, have been found to interact with PHGDH. BPGM, bisphosphoglycerate mutase; CDC5L, cell division cycle 5-like protein; IK, protein red; PGAM1/2/3, phosphoglycerate mutase 1/2/3; PHGDH, phosphoglycerate dehydrogenase; PSAT1, phosphoserine aminotransferase 1; PSPH, phosphoserine phosphatase; SAP18, Histone deacetylase complex subunit SAP18; SRSF10, Serine/arginine-rich splicing factor 10.

ATACseq, Assay for Transposase-Accessible Chromatin using sequencing; Cm, central memory murine T cells; DN, double negative; E, glutamate; Em, effector memory murine T cells; ImmGen, Immunological Genome Project; LCMV, lymphocytic choriomeningitis virus; NLS, Neu-Laxova syndrome; Nve; naive murine T cells; Q, glutamine; R, arginine; RBP, RNA-binding proteins; RNAseq, RNA sequencing; Sp, Splenic; Th, Thymic; T8, $CD8^+$ murine T cells; UCSC, University of California Santa Cruz; WT, Wildtype.

A IP-antibody testing on PHGDH^{WT} and PHGDH^{KO} lysates

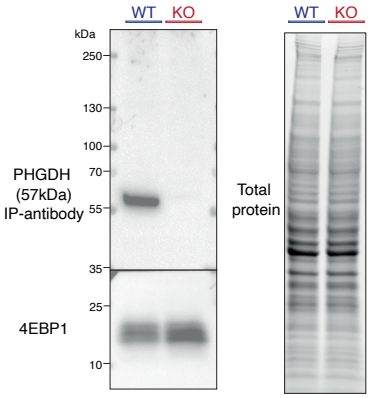

B Volcano plot representation of the RIPseq experiment

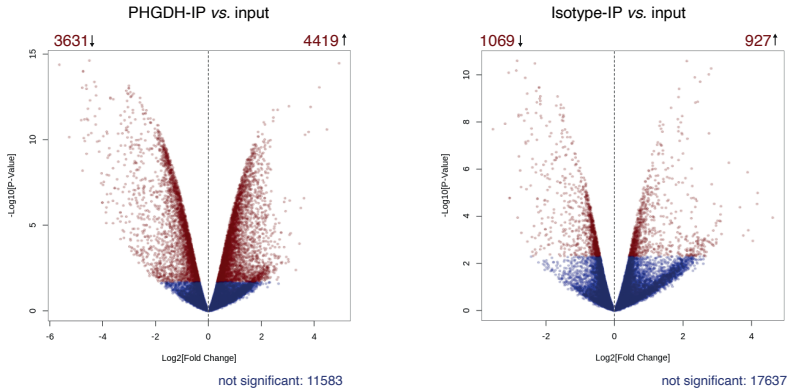

C GO term enrichement analysis on specifically pull-downed transcripts by PHGDH-IP

#	Pathway Maps	Enrichment p-value	# transcripts in category	# differentially expressed transcripts
1	Transcription_Epigenetic regulation of gene expression	2.1E-11	57	18
2	Immune response_IL-4 signaling pathway	2.4E-08	94	19
3	Signal transduction_Angiotensin II/AGTR1 signaling via Notch, Beta-catenin and NF-kB pathways	2.7E-08	76	17
4	Development_WNT/Beta-catenin signaling in the nucleus	5.8E-08	62	15
5	Development_TGF-beta receptor signaling	3.0E-07	52	13
6	Development_Negative feedback regulation of WNT/Beta-catenin signaling	3.6E-07	37	11
7	Development_WNT/Beta-catenin signaling in the cytoplasm	6.0E-07	55	13
8	Immune response_IL-3 signaling via JAK/STAT, p38, JNK and NF-kB	6.0E-07	93	17
9	Development_Negative regulation of WNT/Beta-catenin signaling in the nucleus	1.6E-06	89	16
10	Immune response_IL-6 signaling pathway via JAK/STAT	2.3E-06	71	14
11	Neuroprotective action of lithium	3.1E-06	63	13
12	Signal transduction_mTORC1 upstream signaling	3.9E-06	74	14
13	TNF-alpha-induced inflammatory signaling in normal and asthmatic airway epithelium	4.3E-06	38	10
14	Oxidative stress_ROS-induced cellular signaling	5.2E-06	108	17
15	Prolactin/ JAK2 signaling in breast cancer	5.7E-06	24	8
16	Development_NOTCH1-mediated pathway for NF-KB activity modulation	1.1E-05	26	8
17	Neurogenesis_NGF/ TrkA MAPK-mediated signaling	1.5E-05	105	16
18	Apoptosis and survival_Role of PKR in stress-induced apoptosis	1.7E-05	53	11
19	G-protein signaling_Regulation of p38 and JNK signaling mediated by G-proteins	2.6E-05	37	9
20	Immune response_IL-7 signaling in T lymphocytes	2.6E-05	37	9

D Investigating kinetics of the DNA double-strand break repair

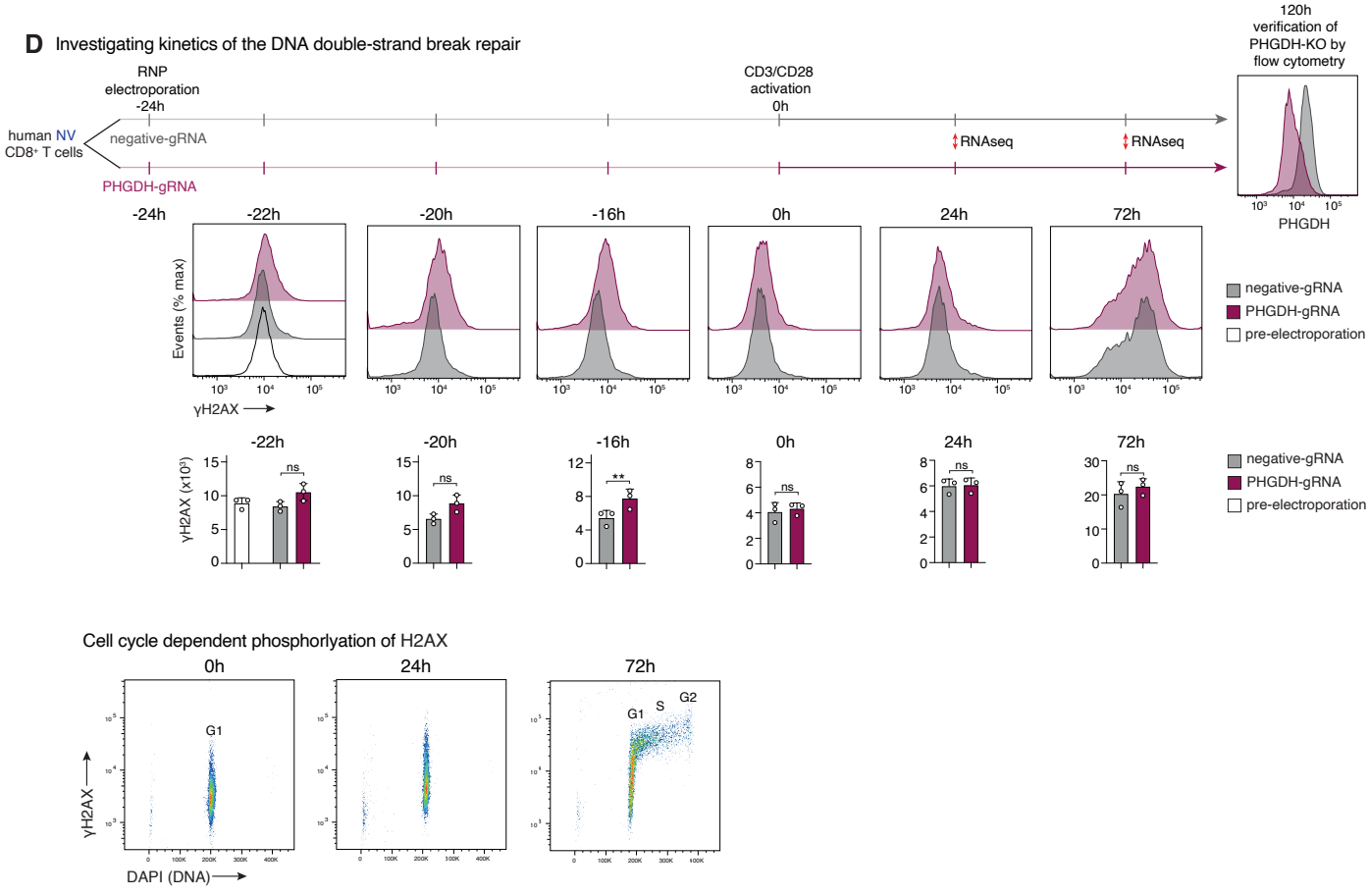

Figure S6. Related to Figure 6. PHGDH functions as an RNA-binding protein in primary T cells.

E RNAseq after CRIPSR:
24h post-activation readout

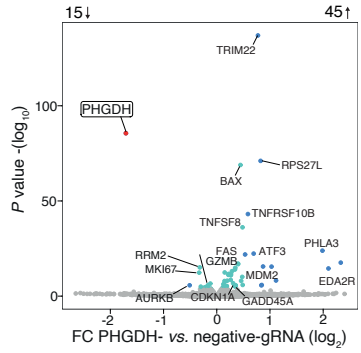

F GO term enrichement analysis on differentially expressed transcripts at the 24h post-activation timepoint

#	GO Networks	Enrichment p-value	# transcripts in category	# differentially expressed transcripts
1	Cell cycle_G2-M	9.4E-10	206	12
2	Cell cycle_G1-S	2.5E-07	162	9
3	DNA damage_Checkpoint	4.0E-07	124	8
4	Cell cycle_S phase	1.5E-06	148	8
5	Cell cycle_Core	5.3E-04	118	5
6	Apoptosis_Death Domain receptors & caspases in apoptosis	6.5E-04	123	5
7	Development_Regulation of angiogenesis	1.5E-03	221	6
8	Apoptosis_Apoptotic nucleus	2.2E-03	161	5
9	Muscle contraction	2.9E-03	173	5
10	Cell cycle_Mitosis	3.4E-03	179	5

G Establishing fluorescent polarisation assays with GAPDH:

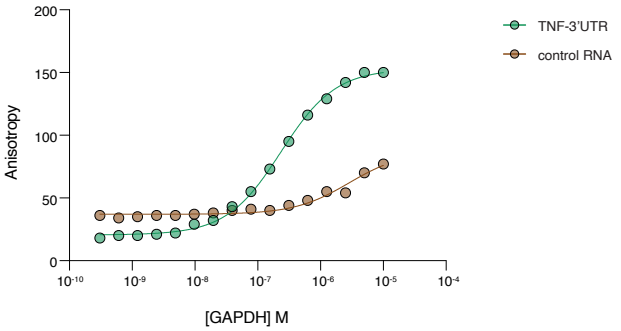

H Establishing RNA-EMSA assays with GAPDH:

Target RNA: Sequence from the TNF-3'UTR:
5'-FAM-GUGAUUAUUUAUUAUUUAUUUAUUAUUUAUUUAUUUAG-3'

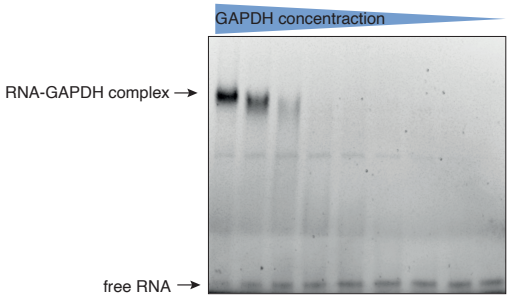

Control RNA: Sequence from rabbit β-globin:
5'-FAM-UGGCCAAUGCCCUGGCUCACAAAUACCACUG-3'

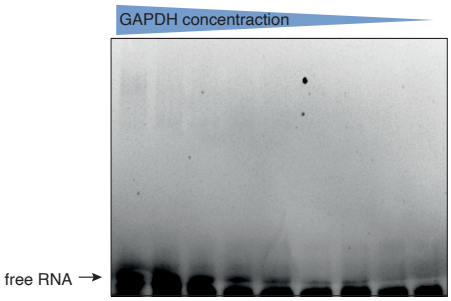

Figure S6. Related to Figure 6. PHGDH functions as an RNA-binding protein in primary T cells.

Figure S6. Related to Figure 6. PHGDH functions as an RNA-binding protein in primary T cells.

(**A**) Specificity of the PHGDH-antibody (#66350, D8F30, Cell Signaling), which was used for the RIPseq experiment, was tested on $PHGDH^{WT}$ (WT) and $PHGDH^{KO}$ (KO) Jurkat T cell lysates. Total protein stain was obtained by using stain free technology (Biorad).

(**B**) Volcano plot representation of transcript abundance in PHGDH-IP *vs.* input (left) and isotype-IP *vs.* input (right). Red dots indicated significantly differentially expressed transcripts with $p_{adj}<0.05$, whereas blue dots represent transcripts without significant enrichment after IP. From the 927 transcripts enriched in the isotype-IP, 637 were also enriched in the PHGDH-IP.

(**C**) GO term enrichment analysis on specifically enriched transcripts by PHGDH-IP as defined in Figure 6B.

(**D**) Time course experiment investigating the kinetics of PHGDH gene-editing and DNA-DSB repair based on γH2AX staining. The upper part of the figure shows a schematic of the experimental setup, followed by representative flow cytometry histograms and summary bar graphs of γH2AX stainings at different timepoints post-RNP electroporation (n=3). Phosphorylation of H2AX (γH2AX) was cell-cycle dependent, with increasing levels in S and G2 phase compared to the G1 phase (pseudo color plots at the bottom) – as described for other cells (Huang et al., 2006).Therefore, γH2AX staining increased, when cells left G1 phase at the 24h and 72h post-activation time point, without differing between PHGDH- and negative-gRNA treatment.

(**E**) Volcano plot comparing transcript abundance in PHGDH- *vs.* negative-gRNA treated primary effector T cells at the 24h post-activation time point.

(**F**) GO term enrichment analysis on DEGs between PHGDH- *vs.* negative-gRNA treated primary effector T cells at the 24h post-activation time point (48h post-RNP electroporation).

(**G**) Establishing fluorescent polarization (FP) assays for future testing of RNA-binding by PHGDH. Shown are anisotropy measurements of reactions containing the indicated FAM-labeled RNA species (10nM) and increasing concentrations of GAPDH. The assay was performed with an RNA-sequence binding GAPDH (green) and a non-binding control RNA (brown) (White et al., 2015).

(**H**) Establishing RNA-EMSA assays for future testing of RNA-binding by PHGDH. After FP measurements (Figure S6G), the binding reactions were loaded on a gel and separated based on size in order to visualize RNA-GAPDH complex and free RNA.

All experiments were done with human primary cells. Data are represented as mean ± SD. Statistical significance was assessed by two-sided unpaired Student's *t*-test (**D**). $*P < 0.05$, $**P < 0.01$; ns, not significant.

FAM, fluorescein amidites; FC, fold change; FP, fluorescent polarization; FSC-A, forward scatter area; DEGs, differentially expressed genes; DSB, double-strand break; EMSA, electrophoretic mobility shift assay; GO, gene ontology; gRNA, guide RNA; IP, immunoprecipitation; KO, knock-out; p_{adj}, adjusted p value; RIPseq, RNA immunoprecipitation followed by sequencing; RNAseq, RNA sequencing; RNP, ribonucleoprotein; T_{NV}/NV, naïve $CD8^+$ T cells; WT, wildtype.

7. MATRIALS AND METHODS

7.1. METHOD DETAILS – Experiments with human cells

7.1.13 Mass spectrometry

For proteomics

For amino acid measurements

For metabolic tracing

7.1.14 *In silico* comparison of GAPDH and PHGDH

7.2 METHODS DETAILS – Mouse experiments

7.2.1 Animals

7.2.2 Murine $CD8^+$ T cell isolation

7.2.3 Murine T cell activation

7.2.4 FACS sorting

7.2.5 *In vivo* infection model

7.2.6 Adoptive transfer experiments

7.3 QUANTIFICATION AND STATISTICAL ANALYSIS

7.1 METHODS DETAILS – Experiments with human cells

7.1.1 Healthy blood donors

Blood samples were obtained from healthy female and male donors (16-65 years old) as buffy coats after written consent (Blood donation center, University Hospital Basel).

7.1.2 Cell Lines

Jurkat T cells were initially purchased from ATCC and re-authenticated by short tandem repeat (STR) profiling (Microsynth) matching 100% over all 15 autosomal STRs to the DNA profile of Jurkat E6.1 (Cellosaurus, RRID:CVCL_0367) and found negative for mycoplasma by PCR. THP-1 cells were kindly provided by Bojana Müller and promyeloid HL-60 (ATCC CCL-260, DSMZ, Braunschweig, Germany) by Thorsten Schäfer (both from University of Basel).

7.1.3 Cell culture

Cells were cultured in a 5% CO_2 and ambient oxygen incubator in RPMI-1640 medium (Gibco) containing 10% fetal bovine serum (FBS)(Gibco), 50U/ml penicillin and 50 mg/ml streptomycin (PenStrep)(Gibco). This full media is from now on called R10FBS. For experiments lacking serine, custom RPMI (Wisent) was supplemented with PenStrep and 10% (v/v) heat-inactivated dialyzed FBS (dFBS)(Gibco). This media was filtered through a 0.2µm filter prior to use. The following compounds were added to this media as indicated: L-serine (285µM, Sigma), RZ-755 PHGDH inhibitor (5µM, RAZE Therapeutics, gift from Russell Jones), RZ-2994 SHMT1/2 inhibitor (1.25µM, RAZE Therapeutics, gift from Russell Jones), Rapamycin (20ng/ml, Merck) Cycloheximide (50µM, Sigma), ATRA (1µM , Sigma), PMA (50ng/ml, Tocris). For growth curves, cells were counted using an CASY cell counter (Innovatis, Roche Applied Science) or an EVE Cell Counter (Witec).

7.1.4 Human cell isolation

Peripheral blood mononuclear cells (PBMC) were isolated from female and male healthy donors by standard density-gradient centrifugation protocols (#1114547, Lymphoprep Fresenius Kabi). $CD8^+$ T cells were enriched by positive selection using magnetic $CD8^+$ beads (#130-045-201, Miltenyi Biotec) and rested overnight in R10FBS before FACS-sorting (see below).

7.1.5 Human T cell activation

Human $CD8^+$ T cell activation was performed using in house generated anti-CD3/anti-CD28 coated microbeads as previously described (Bantug et al., 2018; Fischer et al., 2018). All T cell activations were performed using a 2:1 bead to cell ratio unless otherwise indicated and occurred in flat bottom 96-well plates ($2.5x10^5$ cells/well; $5x10^5$ beads/well).

7.1.6 Flow cytometry

All flow data were acquired on a CytoFLEX flow cytometer (Beckman Coulter) and analyzed using Flowjo 10.3 (Tree Star) unless otherwise indicated.

For FACS-sorting

For fluorescence-activated cell sorting (FACS), $CD8^+$ T cells were stained with anti-CD62L-APC (#21279626, LT-TD180, ImmunoTools) or anti-CD62L-PeCy7 (#304821, DREG-56, BioLegend) and anti-CD45RA-PB (#A74765, J.33, Beckman Coulter) antibodies. T_{NV}, T_{CM} and T_{EM} $CD8^+$ T cells were identified as $CD62L^+$ $CD45RA^+$, $CD62L^+$ $CD45RA^-$ and $CD62L^-$ $CD45RA^-$ populations, respectively and sorted by using a BD influx cell sorter (BD Bioscience). Cells were rested in R10FBS for minimum of 4h at 37°C prior to further experiments.

For viability stainings

Before most of the flow cytometric readouts, a viability staining has been performed. To this end, cells were washed once with PBS and subsequently incubated for 10min at RT with a fixable viability dye (Zombie Green, #423111, BioLegend or Zombie Aqua, #423101, BioLegend) in PBS. After two washes with FACS buffer (PBS with 0.5% BSA and 5mM EDTA), further stainings were performed.

For surface stainings

After indicated timepoints and experimental culture conditions, cells were incubated with fluorescent antibodies for 30min on ice in order to stain surface proteins. The following surface antibodies were use: Anti-CD25-APC-H7 (#560225, M-A251, BD Bioscience), anti-CD71-Pe (#334107, CY1G4, BioLegend), anti-CD98-FITC (#315603, MEM-108, BioLegend), anti-CD69-FITC (#21620693, FN50, ImmunoTools) and anti-CD107a-APC (#328619, H4A3, BioLegend).

For intracellular stainings

After incubation with the fixable viability dye and two washes with FACS buffer, cells were prepared for intracellular staining using the intracellular Fixation and Permeabilization Buffer Set (#88-8824-00, eBioscience) and protocol. Subsequently, primary antibody staining was performed for 30min on ice. After two washes with perm-buffer, secondary antibody staining was performed for another 30min on ice. Cells were then washed with perm-buffer, resuspended in FACS buffer and analyzed. The following primary antibodies were used in perm-buffer: Rabbit anti-PHGDH (#66350, D8F30, Cell Signaling), rabbit anti-p-S6 (S240/244) (#5364, D68F8, Cell Signaling), anti-H2AX-phosphorylated (Ser139)-APC (#613415, 2F3, BioLegend). Unconjugated primary antibodies were stained with the following secondary antibody: Goat anti-rabbit IgG AF594 (#A32740, Thermo).

For NBDG uptake experiments

Sorted $CD8^+$ T cells were cultured under indicated conditions for 24h. To assay the uptake of this fluorescent glucose analogue, 20µM of 2-NBDG (#N13195, Thermo) were added to the media for 45min. After two washes with FACS-buffer, NBDG-uptake was measured by flow cytometric evaluation of the signal in the FITC channel.

For dye dilution experiments

Sorted $CD8^+$ T cells were loaded prior to activation with the cell-proliferation dye CFSE (#C34554, Thermo) according to manufacturer's instructions. Subsequently, cells were washed, resuspended in indicated media and stimulated using activation beads. Proliferation was assessed 5 days after activation. Due to GFP expression, Jurkat T cells were incubated with Cell Trace Violet (#C34571, Thermo) instead of CFSE.

For cell cycle analysis

Cells were cultured under indicated conditions. At designated timepoints, cells were incubated with a fixable viability dye and washed with FACS buffer. Subsequently, cells were prepared for intracellular staining using the intracellular Fixation and Permeabilization Buffer Set (#88-8824-00, eBioscience) and protocol. After permeabilization, cells were resuspended in a 3µM DAPI solution (#D1306, Thermo) and DNA content was assessed by flow cytometry. The curve fitting and the percentage of cells in G0/G1, S and G2/M phases of the cell cycle as well as in the sub-G1 area were determined by using the CellCycle interface of the FlowJo 7.2 software (Tree Star Inc).

For analysis of translation

Sorted T cells were cultured under indicated conditions. Puromycin (10µg/ml, #P8833, Sigma) was added to the cell culture media during the last 10min and incubated at 37°C, 5% CO_2. During incubation, puromycin is incorporated into newly nascent polypeptide chains by actively translating ribosomes, due to its structural analogy with the tyrosyl-tRNA and can be quantified with an anti-puromycin antibody (Schmidt et al., 2009). After incubation, cells were rinsed with PBS and prepared for intracellular staining using the intracellular Fixation and Permeabilization Buffer Set (#88-8824-00, eBioscience) and protocol. Puromycin-tagged polypeptides were then labeled with an anti-puromycin antibody (#MABE343-AF488, 12D10, Merck) for 30min on ice at a 1 to 3000 dilution and samples analyzed on a Cytoflex flow cytometer (Beckman Coulter). Cycloheximide (50µM, Sigma) treatment for 10min was used to broadly inhibit translation and served as a control (data not shown).

7.1.7 Metabolic flux analysis

Sorted T cells were cultured under indicated conditions. After 24h of activation, a Seahorse XF-96 extracellular flux analyzer (Seahorse Bioscience, Agilent) was used to assess oxygen consumption rate (OCR, pmol/min) and extracellular acidification rate (ECAR, mpH/min). Briefly, cells were harvested, resuspended in serum-free unbuffered RPMI 1640 (#R6504, Sigma) and plated onto Seahorse cell plates ($2x10^5$ cells/well) coated with Cell-Tak (BD Bioscience). Mitochondrial perturbation experiments were carried out by sequential addition of 1µM oligomycin (#75351, Sigma), 2µM FCCP (#C2920; Sigma) and 1µM rotenone (#R8875, Sigma).

7.1.8 Western blotting

Cells were washed two times with PBS and lysed in ice-cold RIPA buffer (#89900, Thermo) supplemented with protease- (#4693159001, Roche) and phosphatase inhibitors (#4906845001, Roche). The resulting lysate was cleared by centrifugation and the protein concentration of the supernatant assessed with the Pierce BCA Protein Assay Kit (#23227, Thermo). Equal amounts of protein were loaded on a precast mini-PROTEAN TGX gel (#4568095, Biorad) and SDS-PAGE fractionated. After electrophoresis, total protein was assessed by the stainfree-protocol from Biorad (5min UV activation followed by imaging with a GelDoc system). Then, proteins were transfer to nitrocellulose (#1704158, Biorad) and the membrane blocked for 1h at RT in 5% BSA or milk in TBST. Membranes were incubated at 4°C overnight with specific primary antibodies followed by horseradish peroxidase (HRP)-conjugated secondary antibodies (1h at RT). Enhanced chemiluminescence (ECL) was used

for developing, the Geldoc system for imaging and the ImageLab software for quantification (both from Biorad). Western blotting was performed with the following primary antibodies: Rabbit anti-PHGDH (#66350, D8F30, Cell Signaling), Mouse anti-PHGDH (ab57030, abcam, used after IP of PHGDH), rabbit anti-PSAT1 (ab154055, abcam), rabbit anti-PSPH (ab211418, abcam), rabbit anti-SLC1A4 (#8442, Cell Signaling), rabbit anti-SLC1A5 (ASCT2) (#8057, D7C12, Cell Signaling), rabbit anti-SHMT1 (#12612, Cell Signaling), rabbit anti-SHMT2 (ab155230, abcam), rabbit anti-beta-actin (#3700, 8H10D10, Cell Signaling), rabbit anti-CD71 (#13113, D7G9X, Cell Signaling), rabbit anti-Myc (#5605, D84C12, Cell Signaling), rabbit anti-GLUT1 (ERP3915, ab115730 abcam), rabbit anti-p-p70S6K (T389) (#9234, 108D2, Cell Signaling), rabbit anti-p70S6K (#9202, Cell Signaling), rabbit anti-p-S6 (S240/244) (#5364, D68F8, Cell Signaling), rabbit anti-S6 (#2217,5G10, Cell Signaling), rabbit anti-p-4EBP1 (T37/46) (#2855, 236B4, Cell Signaling), rabbit anti-4EBP1 (T389) (#9644, 53H11, Cell Signaling), rabbit anti-ATF4 (#11815, D4B8, Cell Signaling).
Subsequently, the following secondary antibodies were used: HRP goat anti-rabbit IgG (#111-035-144, Jackson ImmunoResearch) and HRP goat anti-mouse IgG (#115-035-003, Jackson ImmunoResearch).

7.1.9 PHGDH activity assay

Jurkat T cells expressing indicated PHGDH variants were washed once in ice cold PBS, snap frozen in liquid nitrogen and stored at -80°C until further use. At the day of the assay, cell-pellets were thawed, homogenized in lysis buffer (0.5M Tris pH 8.5, 1mM EDTA, 0.02% Triton-X, 10mM NAD) and cell debris was removed by centrifugation (16000xg for 10min at 4°C). Protein concentration of the cleared lysates was measured using Pierce BCA Protein Assay Kit (#23227, Thermo). Protein amounts were adjusted with assay buffer (50mM Tris pH 7.1, 10mM NAD) in order to have 50µg total protein in 150µl of buffer. PHGDH activity was measured in two wells for every sample, once in presence of the substrate 3-phospho-D-glycerate (3PG) (20mM, P8877, Sigma) and once in absence of it – always in a final volume of 200µl. NADH-formation by catalytic activity of PHGDH was measured with a Sinergy H1 microplate reader (Biotek) at 340nm at RT. PHGDH activity was then calculated by subtracting absorption values obtain in absence of 3PG from values obtained in presence of 3PG.

7.1.10 *In vitro* differentiation assays (THP-1 and HL-60 cell lines)

THP-1 cells were cultured in R10FBS in a 6-well plate at 0.5Mio per ml when differentiation was induced by adding 50ng/ml PMA (#1201, Tocris) (Chanput et al., 2014). After 24h incubation, PMA was washed away and fresh media added. With differentiation, cells became

adherent and started expressing CD36 (data not shown). At indicated timepoints, cells were processed for Western blotting.

HL-60 cells were propagated in DMEM (#61965-026, Gibco) supplemented with 10% FBS and PenStrep. Granulocytic cell differentiation was induced with 1µM all-trans retinoic acid (ATRA) (#R2625, Sigma) as described previously (Breitman et al., 1980; Tasseff et al., 2017). In brief: 1Mio cells were seeded into 25cm^2 flasks and incubated for 3 consecutive days with or without ATRA supplementation, by the end of which the medium was renewed and fresh medium containing ATRA or not was added. On indicated days post-treatment, cells were harvested for protein lysates and differentiation assessed by live cell microscopy (AX10, Zeiss, 40x objective, AxioVision LE software) to document induction of amoeboid cell morphology. Additionally, flow cytometry stainings have been performed, revealing upregulation of CD11b as a molecular determinant of neutrophil differentiation and downregulation of PHGDH, also when gating out dead cells, which became more prevalent at later timepoints (data not shown).

7.1.11 Genetic manipulation of PHGDH

Ribonucleoprotein (RNP) assembly

Delivery of Cas9 RNP-complexes, consisting of an Alt-R CRISPR RNA (crRNA, Integrated DNA Technologies (IDT)), trans-activating crRNA (tracrRNA) (#222427350, IDT) and Cas9 protein (QB3 MacroLab, University of California, Berkeley) was based on electroporation and a protocol provided by IDT (IDT Amaxa, 2018). The crRNA targeting PHGDH was selected based on a previous publication (Pacold et al., 2016) (AAAGCAGAACCTTAGCAAAG; PAM: AGG; target sequence genomic region: chr1:119712118; exon 1; + strand). The non-targeting crRNA used as a negative control guide RNA consisted of a sequence, which was not targeting to the human reference genome (#222427352, IDT, sequence: AAUUAUGGGGAUUACUAGGA). Upon delivery, crRNA and tracrRNA were resuspended in Nuclease-Free IDTE Buffer at a final concentration of 200µM each. Then, the two RNA oligos were mixed in equimolar concentrations and diluted with IDTE-buffer to a final concentration of 50µM each. For annealing of crRNA and tracrRNA, the oligos were heated to 95°C for 5min and then cooled to RT, resulting in 50µM single-guide RNA (gRNA). Cas9 protein (40µM) was gently mixed 1:1 with the gRNAs and incubated at RT for 15min resulting in 20µM RNP-complexes.

Gene-editing of primary human T cells prior RNAseq

After the sort, T_{NV} cells were rested for 4h. Then, two times 2Mio cells from each donor were harvested, washed once with PBS and resuspended in 20µl electroporation buffer from the P3 Primary Cell 96-well Nucleofector Kit (V4XP-3032, Lonza). 3µM RNPs were added and electroporated with the 4D-Nucleofector (Amaxa-Lonza) program EH115. Immediately after electroporation, pre-warmed R10FBS containing IL-2 (150U/ml, Proleukin) was added to the cells. Nuclease activity and DNA-repair processes were given time for 24h before activation.

Generation of PHGDH^{KO} Jurkat T cells

Jurkat cells were split the day before electroporation. After washing 2Mio cells with PBS, they were resuspended in 20µl electroporation buffer from the SE cell line 96-Nucleofector Kit (V4SC-1096, Lonza), mixed with 3µM PHGDH-RNPs and electroporated with the 4D-Nucleofector (Amaxa-Lonza) program X-001. Immediately after electroporation, pre-warmed R10FBS was added to the cells. For single cell cloning, one cell per well was sorted by flow cytometry into round-bottom 96-well plates one day after electroporation. After approximately 3 weeks in the incubator, wells containing visible cell pellets were screened for PHGDH expression by flow cytometry, promising clones further expanded and stocks frozen at -80°C.

Re-expression of PHGDH variants

cDNA encoding the human PHGDH (WT) protein or the variants R163Q and R236E thereof were PCR amplified from source vectors obtained from GenScript (GenEZ ORF Clone: PHGDH_OHu19607C_pcDNA3.1(+)) using primers (PHGDH-fwd: 5'- GCG ACA TCG ATA ACC ATG GCT TTT GCA AAT CTG CG -3' and PHGDH-rev: 5'- CTG ACG GAT CCT TAG AAG TGG AAC TGG AAG G -3') and sub-cloned into a lentiviral expression vector (pSFFV-IRES/GFP) involving ClaI and BamHI restriction sites. Sequence-verified plasmids were packed into lentiviral particles according to standardized procedures. In brief, HEK-293 cells (ATCC, CRL-1573) were propagated in DMEM (Gibco) and co-transfected with pCMV-dR8.9 and VSV-G viral packaging vectors (Addgene, #2221 and #14888, respectively) as well as pSFFV-expression plasmids using lipofectamine 2000 (#11668030, Thermo). 24h and 72h after transfection, the medium was harvested, cleared over a 0.45µm SteriTop filter units (Merck) and lentiviral particles enriched using Vivaspin 20ml centrifugal concentrators (Z614688-48EA Sartorius, Sigma) at 3000xg. Derived lentiviral concentrates were spotted onto Jurkat T cells according to standard procedures and positively selected for the expression of co-transduced (IRES)/GFP by FACS.

7.1.12 Sequencing

Sanger sequencing of genomic DNA

From various PHGDH^{KO} clones obtained by single cell cloning, 5Mio cells were harvested and DNA isolated according to the QIAamp DNA mini protocol (#51304, Qiagen). After DNA purification and quantification with a NanoDrop device (Witec), the region around the Cas9 cutting site was PCR-amplified with the following primers: PHGDH-fwd: 5'- CTA CTC ACA GCG GCC GAT TC-3' and PHGDH-rev: 5'- GCA TGC CAA CGT GAA AGA CG-3'. Amplicons were analyzed by gel electrophoresis, purified using the QIAquick PCR purification kit (#28104, Qiagen) and sequenced by Microsynth. Based on chromatograms and Western blots of the same cells (Figure S3K, L), three PHGDH^{KO} clones were chosen for further experiments.

RNA Sequencing of quiescent T_{NV} and T_{EM} cells

RNA extraction: Total RNA was isolated from 2.5Mio T_{NV} and T_{EM} cells from 4 healthy donors using TRIzol reagent (#15596026, Thermo) and cleaned up with RNeasy Mini Kit (#74106, Qiagen) according to the manufacturers' protocols. Residual genomic DNA was removed from RNA samples by DNAse treatment (#AM19077, Thermo) as recommended by the manufacturer.

Sample preparation and sequencing: Purity and integrity of isolated total RNA was assessed on a Fragment Analyzer System (Advanced Analytical Technologies). RNA concentration was determined with the Quant-iT RiboGreen RNA Assay Kit (Thermo). Purification of poly(A)-containing mRNA, mRNA fragmentation and cDNA library preparation for RNA-Seq were performed using the TruSeq Stranded mRNA LT Sample Preparation kit (Illumina) according to the manufacturer's protocol. Before sequencing, quality and quantity analysis of prepared cDNA libraries was done on a Fragment Analyzer System (Advanced Analytical Technologies). cDNA libraries were sequenced as single-end reads with 75 cycles on a NextSeq 500 sequencing system (Illumina) at the Genomics Facility Basel, Switzerland.

RNA sequencing data analysis: The quality of raw sequencing data was first examined with FastQC ((Andrews S. 2010). FastQC: a quality control tool for high throughput sequence data. Available online at: http://www.bioinformatics.babraham.ac.uk/projects/fastqc)). Next, sequencing reads were submitted to adapter and quality trimming by Trimmomatic to remove technical sequences like Illumina-specific sequencing adapters and low-quality bases (Bolger et al., 2014). The TopHat2 spliced alignment software and its underlying mapping engine Bowtie2 were used to align the reads to the human reference genome, thereby creating binary

alignment map (BAM) files (Kim et al., 2013). BAM files were sorted and indexed using SAMtools (Li et al., 2009) and then visualized in the UCSC Genome Browser (Kent et al., 2002). Counting of reads that map to each genomic feature was done with the summarizeOverlaps function from the GenomicAlignments package in R (Lawrence et al., 2013). Genes differentially expressed between T_{NV} and T_{EM} cells were identified with the R package DESeq2 (Love et al., 2014).

RNA sequencing after activation of T_{NV} and T_{EM} cells as well as after PHGDH-KO in T_{NV} cells

RNA extraction: For sorted T_{NV} and T_{EM} cells, which were activated in ±serine and ±PHGDH-inhibitor, total RNA was extracted from 1.5Mio cells from 3 human donors. For T_{NV} cells, which were electroporated with RNP-complexes, total RNA was extracted from 2Mio cells per condition from 5 human donors. For both experiments, RNA was extracted using the RNeasy Mini Kit (#74106, Qiagen) according to the manufacturers' protocols, including an on-column DNAse (#79254, Qiagen) treatment.

Sample preparation and sequencing: RNA integrity was checked on the TapeStation instrument (Agilent) using the RNA ScreenTape (#5067-5576, Agilent) and quantified by fluorometry using the QuantiFluor RNA System (#E3310, Promega). Library preparation was performed, starting from 200ng total RNA, using the TruSeq Stranded mRNA Library Kit (#20020595, Illumina), the TruSeq RNA UD Indexes (#20022371, Illumina) and the TruSeq RNA CD Index Plate (#20019792, Illumina). 15 cycles of PCR were performed. Resulting libraries were sequenced Paired-End 101 bases (in addition: 8 bases for index 1 and 8 bases for index 2) using the NovaSeq 6000 instrument (Illumina) and the S2 Flow-Cell loaded with a final concentration of 380pM per Flow-lane and including 1% PhiX. Primary data analysis was performed with the Illumina RTA version 3.4.4. On average per sample: 69.1±11.5 millions pass-filter reads were collected on one S2 Flow-Cell.

RNA sequencing data analysis: Reads were aligned to the human genome (UCSC version hg38 analysis set) with STAR (version 2.7.0c) (Dobin et al., 2013) with default parameters except for allowing up 10 hits to genome (outFilterMultimapNmax 10), reporting only one location for multimapping reads with equal score (outSAMmultNmax 1), and for filtering reads without evidence in spliced junction table (outFilterType "BySJout"). The output was sorted and indexed with samtools (v 1.9) (Li et al., 2009). Stand-specific coverage tracks per sample were generated by tiling the genome in 20bp windows and counting 5'end of reads per window

using the function bamCount from the Bioconductor package bamsignals (v1.18.0). These window counts were exported in bigWig format using the Bioconductor package rtracklayer (v1.46.0) (Lawrence et al., 2009). Read and alignment quality was evaluated using the qQCReport function of the Bioconductor package QuasR (v 1.26.0) (Gaidatzis et al., 2015). The featureCounts function from Bioconductor package subread (v 2.0.1) (Liao et al., 2019) was used to count the number of reads (5'ends) overlapping with the exons of each gene assuming an exon union model (with used gene model provided by ensembl v96).

Selection of genes used for heatmaps

High confidence p53- and DREAM target gene lists were obtained from the supplementary data of a 'meta-analysis', which is based on independent ChIPseq- as well as perturbation experiments performed on a variety of cell types (Fischer et al., 2016). These gene lists are ranked by a 'p53 expression score', where positive values represent p53 targets and negative values DREAM targets. These ranked lists where overlay with differentially expressed genes of T_{EM} cells activated in -Ser *vs.* +Ser having a p_{adj} smaller than 0.05 and a basemean expression bigger than 50. The 30 genes with highest/lowest 'p53 expression score' fulfilling these criteria are shown. The same lists were then taken for T_{NV} cells as well.

RNA immunoprecipitation sequencing experiment

Immunoprecipitation: PHGDH-RNA complexes were isolated using a Magna-RIP kit (#17-701, Millipore) according to manufacturer's instructions. Briefly, around 10-15Mio sorted T_{NV} cells from 3 different human donors were activated for 36h, washed once with PBS, resuspended in 210µl of the RIP lysis buffer provided in the kit and frozen at -80°C. After thawing, lysed cells were centrifuged at 14000rpm for 10min at 4°C to clear the lysate. The resulting supernatant was distributed equally into two tubes, after removing 10µl – representing the input sample. For the IP, 4µg of anti-PHGDH antibody (#66350, D8F30, Cell Signaling) or rabbit isotype matched IgG (ab172730, abcam) was used for 50µL of magnetic protein A/G beads. The beads bound PHGDH- and isotype control antibodies were added to one of the two tubes per donor and IP was performed overnight at 4°C. After several washes, an aliquot of each sample was taken to test the efficiency of the IP by Western blotting using the mouse anti-PHGDH (ab57030, abcam) antibody. From this timepoint on, the input RNA was equally processed again. After a proteinase K digestion, RNA was isolated using TRIzol reagent (#15596026, Thermo) and the Direct-zol RNA Microprep kit (#R2062, Zymo). RNAs were eluted in 6ul of RNase-free water.

RNA integrity and quantification: RNA molecules were quality-checked on the Bioanalyzer instrument (Agilent) using the RNA 6000 Pico Chip (#5067-1513, Agilent). Amount of RNAs was quantified by fluorometry using the QuantiFluor RNA System (#E3310, Promega). Library preparation was performed, starting from 1ng total RNA, using the SMART-Seq Stranded Kit (#634444, Takara Bio). Libraries were sequenced Paired-End 51 bases (in addition: 8 bases for index 1 and 8 bases for index 2) using the NovaSeq 6000 instrument (Illumina) and the SP Flow-Cell loaded at a final concentration in Flow-Lane of 400pM and including 1% PhiX. Primary data analysis was performed with the Illumina RTA version 3.4.4. On average per sample: 38.3±18.8 millions pass-filter reads were collected on 1 SP Flow-Cell.

RNA sequencing data analysis: Read alignments were performed and count tables were obtained as described above. The data were normalized by applying the TMM method from Bioconductor edgeR package (version 3.28.1) (Robinson et al., 2010). Only genes having log2 CPM counts bigger than 0 in at least 2 samples were kept for the further analyses. The principal component analysis was based on 25% of most variable genes in the dataset. The differentially expressed genes were identified using the quasi-likelihood (QL) method (Lund et al., 2012) Implemented in edgeR package (version 3.28.1) using replicate id as covariate.

7.2.13 Mass spectrometry

For proteomics

Sample preparation: After FACS-sorting, 5Mio T_{NV} and T_{EM} cells were washed three times with cold PBS before flash-freezing the samples in liquid nitrogen and shipping on dry ice to the proteomics facility (Functional Genomics Center, Zurich, Switzerland). The cell pellets were lysed by adding 30µl of SDS-buffer (4% SDS, 100mM Tris/HCL pH 8.2, 0.1M dithiothreitol) followed by two freeze/thaw cycles. Afterwards the samples were boiled at 95°C for 5min and 70µl of UT-buffer (8M Urea in 100mM Tris/HCL pH 8.2) were added. Protein concentrations were determined with the Qubit® Protein Assay Kit (Life Technologies, Zurich, Switzerland). For each sample, 75µg of proteins were used for on-filter digestion according to an adapted, filter-aided sample preparation (FASP) protocol. Briefly, proteins were diluted in 200µl of UT-buffer, loaded on Ultracel 30000 MWCO centrifugal unit (Amicon Ultra, Merck) and centrifuged at 14000xg. SDS-buffer was washed away by adding 200µl UT-buffer followed by centrifugation. By 5min incubation with 100µl UT-buffer containing 0.05M iodoacetamide, reduced proteins were alkylated followed by three 100µl washing steps with UT- and two 100µl washing steps with Triethylammonium bicarbonate buffer (50mM TEAB, pH 8). Lastly,

proteins were on-filter digested with 120µl of TEAB containing trypsin (Promega) at a ratio of 1:50 (w/w). Digestion was performed in a wet chamber at room temperature overnight. After elution, the peptides were acidified to a final 0.1% TFA and 3% acetonitrile concentration. Then, samples were dried and re-solubilized in 10µl of 3% acetonitrile, 0.1% formic acid for mass spectrometry (MS) analysis.

LC-MS analysis: MS analysis was performed on a QExactive mass spectrometer coupled to a nano EasyLC 1000 (Thermo). Solvent composition at the two channels was 0.1% formic acid for channel A and 0.1% formic acid, 99.9% acetonitrile for channel B. For each sample 4µL of peptides were loaded on a EasySpray column (75µm × 500mm, 2um, ES803A, Thermo) and eluted at a flow rate of 300nL/min by a gradient from 2 to 30% B in 85min, 47% B in 4min and 98% B in 4min. Samples were run in a randomized order. The mass spectrometer was operated in data-dependent mode (DDA), acquiring a full-scan MS spectra (300–1700m/z) at a resolution of 70000 at 200m/z after accumulation to a target value of 3000000, followed by HCD (higher-energy collision dissociation) fragmentation on the twelve most intense signals per cycle. HCD spectra were acquired at a resolution of 35000 using a normalized collision energy of 25 and a maximum injection time of 120ms. The automatic gain control (AGC) was set to 50000 ions. Charge state screening was enabled and singly and unassigned charge states were rejected. Only precursors with intensity above 8300 were selected for MS/MS (2% under fill ratio). Precursor masses previously selected for MS/MS measurement were excluded from further selection for 30s, and the exclusion window was set at 10ppm. The samples were acquired using internal lock mass calibration on m/z 371.1010 and 445.1200. The mass spectrometry proteomics data were handled using the local laboratory information management system (LIMS) (Türker et al., 2010).

Protein identification and quantification: The acquired raw MS data were processed by MaxQuant (version 1.4.1.2), followed by protein identification using the integrated Andromeda search engine (Cox and Mann, 2008). Spectra were searched against a Uniprot human reference proteome (taxonomy 9606, canonical version from 2015-09-15), concatenated to its reversed decoyed fasta database and common protein contaminants. Carbamidomethylation of cysteine was set as fixed modification, while methionine oxidation and N-terminal protein acetylation were set as variable. Enzyme specificity was set to trypsin/P allowing a minimal peptide length of seven amino acids and a maximum of two missed-cleavages. MaxQuant Orbitrap default search settings were used. The maximum false discovery rate (FDR) was set to 0.01 for peptides and 0.05 for proteins. Label free quantification was enabled and a 2min

window for match between runs was applied. In the MaxQuant experimental design template, each file is kept separate in the experimental design to obtain individual quantitative values. Protein fold changes were computed based on Intensity values reported in the proteinGroups.txt file.

For the two-group analysis, the statistical testing was performed using t-test on transformed protein intensities (hyperbolic arcsine transformation). Proteins were called significantly differentially expressed if linear fold-change exceeded 2-fold and the p-value from the t-test was below 0.01.

For amino acid measurements

LC-MS/MS instrumentation and settings: Amino acid measurements were performed on a ultra-high-pressure liquid chromatography (UHPLC) system (Shimadzu) connected to an API-4000 Qtrap triple quadrupole mass spectrometer (AB Sciex). A SeQuant ZIC-cHILIC column (3µm, 100Å 100 x 2.1mm PEEK, Merck) was used for amino acid separation applying the following stepwise gradient program: Mobile B at 80% from 0-1min; mobile B 80% to 20% from 1-4min; mobile B 20% from 4-5.5min; mobile B 80% from 5.5-6.5min. For the amino acids alanine, arginine, asparagine, glycine, histidine, isoleucine, leucine, lysine, methionine, phenylalanine, proline, serine, threonine, tryptophan and valine mobile phase A consisted of water supplemented with 0.1% acetic acid, while acetonitrile with 0.1% acetic acid was used as mobile phase B. For the amino acids aspartic acid, glutamate, glutamine and tyrosine mobile phase A consisted of 20mM ammonium acetate with 1% acetic acid, while acetonitrile was used as mobile phase B. All amino acids were analyzed by electrospray ionization in the positive mode and multiple reaction monitoring with a detection window of 30s. The mass transitions, retention times, and the specific potentials of the amino acids are given in Table 1. The LC-MS/MS system was operated and samples were quantitated with Analyst software 1.6.2 (AB Sciex). Amino acid dilution lines were prepared in self-made amino acid free RPMI. A calibration plot of the nominal analyte concentration (x) against peak area ratio of the analyte/IS (y) was applied to estimate the analyte concentration in unknown samples by linear regression. A weighting factor of $1/x^2$ was used.

Metabolite extraction: At indicated timepoints post-activation, 10µL of cell culture media was pipetted off and metabolites were extracted with 290µL internal standard solution containing 500ng/ml L-Serine-13C3,15N (Toronto Research Chemicals). Afterwards, samples were centrifuged (3220xg, 30min, 10°C) and 2.5µL were injected into the LC-MS/MS system.

Table 1. Settings used for the detection and quantification of the investigated analytes.

Analyte	Q1 Mass (Da)	Q3 Mass (Da)	RT (min)	DP (V)	CE (V)	CXP (V)
Alanine	90.0	44.2	3.56	41	19	8
Arginine	175.0	70.2	4.67	56	18	12
Asparagine	133.0	74.0	3.59	36	23	12
Aspartic acid	133.9	74.0	3.71	36	19	14
Glutamic acid	148.0	84.2	3.64	36	23	16
Glutamine	147.0	84.0	3.41	41	14	14
Glycine	75.9	48.0	3.68	46	9	8
Histidine	156.0	110.1	4.63	41	21	20
Isoleucine	132.0	86.1	2.91	46	33	16
Leucine	132.0	86.2	2.78	46	30	14
Lysine	147.0	84.1	4.55	41	19	14
Methionine	150.0	104.1	2.94	36	15	18
Phenylalanine	166.0	120.2	2.66	41	30	22
Proline	116.0	70.1	3.09	41	15	12
Serine	105.7	60.0	3.72	31	17	10
Serine C13 N15	110.0	63.0	3.72	41	17	10
Threonine	120.0	74.0	3.52	41	15	14
Tryptophan	205.0	188.1	2.86	41	27	34
Tyrosin	182.0	136.2	3.13	26	19	12
Valine	118.0	72.0	3.07	36	25	12

For metabolic tracing

For stable isotope tracing experiments, 3-5Mio sorted T cell subsets were plated onto 48-well plates in glucose-free RPMI containing 10% dFBS and 11mM uniformly labeled ^{13}C-glucose (Cambridge Isotope Laboratories). T cells were then activated with anti-CD3/CD28 coated beads for indicated timepoints. Metabolites were extracted using ice cold 80% MeOH, followed by sonication and centrifugation at 4°C to remove cellular debris. Uniformly deuterated myristic acid (750ng per sample) was added as an internal standard. Subsequently, samples were dried with a speedvac, re-solubilized and derivatized as tert-butyldimethylsilyl esters (TBDMS) and analyzed via gas chromatography mass spectrometry (GC-MS) at McGill University, Canada. Metabolite abundance was expressed relative to the internal standard and normalized to cell number. Mass isotopomer distribution (MID) was determined with a custom algorithm developed at McGill University, Canada (McGuirk et al., 2013).

7.1.14 *In silico* comparison of GAPDH and PHGDH

1) Rossman fold: The Rossman folds were highlighted based on existing literature. For GAPDH, this super secondary structure is formed by residues 1-150 and 317-335 (White and Garcin, 2015). For PHGDH, the contiguous residues 102 to 288 adopt a classical Rossman fold comprising a six stranded, parallel β-sheets flanked on both sides by α-helices. Crystal structure of human 3-phosphoglycerate dehydrogenase is online available at: https://www.thesgc.org/sites/default/files/activeISee/PHGDHA_2g76_v5_351m/PHGDHA_2g76_v5_351m_Annotation.html Deposition Authors: Turnbull AP, Salah E, Savitsky P, Gileadi O, von Delft F, Edwards A, Arrowsmith C, Weigelt J, Sundstrom M, Oppermann (2006).

The electrostatic potential: The Adaptive Poisson-Boltzmann Solver plugin (Baker et al., 2001) was installed on Visual Molecular Dynamics (VMD) (Humphrey et al., 1996) to compute the electrostatic potentials.

The dimer interface: The GAPDH dimer interface was defined in (White and Garcin, 2015) as 'antiparallel five stranded β-sheets from adjacent subunits'. For PHGDH, a consensual definition of the dimer interface in terms of residues or secondary structures was not found in the literature. Importantly, the tetrameric form of PHGDH arranges in different ways in different organisms, *i.e.* they form either a type I, II or III complex (Grant, 2018). The human PHGDH undergoes a complex type I structure, in which three different dimer interfaces can be defined. Here, we defined the interface as residues located within less 2.5 Å of a neighboring subunit in the I—R area as defined by (Grant, 2018), and residues forming secondary structures including these interacting residues are highlighted.

7.2 METHODS DETAILS – Mouse experiments

7.2.1 Animals

C57BL/6 (CD45.1 and CD45.2 as well as Thy1.1 and Thy1.2) were purchased from Charles River Laboratories. OT-I mice were purchased from The Jackson Laboratory (Bar Harbor, ME). Mice were housed under specific pathogen-free conditions at McGill University (Canada), the Van Andel Institute (USA) and the University of Basel (Switzerland) according approved protocols. Experiments were performed at 6 to 20 weeks of age.

7.2.2 Murine T cell isolation

Following euthanasia in a CO_2 chamber, spleens were harvested and pushed through a 70µm cell strainer (#431751, Corning). Red blood cells (RBC) were then removed from the single cell suspension with an RBC-lysis buffer (154mM NH_4CL, 10mM $KHCO_3$ and 0.1mM EDTA) and $CD8^+$ T cells MACS-isolated with CD8a-MicroBeads (#130-117-004, Miltenyi Biotec) when mentioned.

7.2.3 FACS sorting of T cell subsets

MACS-enriched $CD8^+$ T cells from 5 mice were stained with the following antibodies for 30min at on ice: anti-CD8a-BV510, anti-CD44-AF647 and CD62L-BV421. After two washes with FACS buffer, cells were sorted on a BD FACS-Aria into T_{NV} ($CD8^+CD62L^+CD44^-$) and T_{EM} cells ($CD8^+CD62L^-CD44^+$).

7.2.4 *In vitro* murine T cell activation

MACS-enriched $CD8^+$ T cells were stimulated with plate-bound anti-CD3 (2ug/ml, #100238, 17A2, BioLegend) and anti-CD28 (5ug/ml, #102116, 37.51, BioLegend) in indicated media.

7.2.5 *In vivo* infection model

For memory re-challenge experiments, mice were immunized with a sublethal dose of recombinant attenuated *Listeria monocytogenes* (Lm) expressing OVA (attLmOVA, $2x10^6$ CFU). After two weeks on a normal diet and resolution of the primary infection, animals were fed either Baker Purified Amino Acid Diet containing all essential amino acids plus serine, glycine, glutamine, arginine, cysteine, and tyrosine, or a test diet lacking serine and glycine, as previously published (Maddocks et al., 2013). Animals were fed each diet for 2 weeks prior to re-infection with a lethal dose of recombinant virulent LmOVA (virLmOVA, $1x10^6$ CFU) and maintained on their respective diets until experimental endpoint. Splenocytes were isolated

prior to re-challenge (44 days post primary infection) and at 5 days post re-challenge. OVA-specific $CD8^+$ memory T cells were stained with an MHC class I tetramer ($K^b/OVA_{257-265}$ MHC Tetramer Production facility, Baylor College of Medicine) as well as fluorescently labeled antibodies against CD8, CD44, KLRG1 and IL7R. Furthermore intracellular cytokine stainings (ICS) for IFNγ, TNF and GZMB were performed following peptide re-stimulation (OVA_{257}) for 4h *ex-vivo* with monensin added for the final 2h of stimulation. Flow cytometry was performed on LSR Fortessa (BD Biosciences) flow cytometer.

7.2.6 Adoptive transfer experiments

Plasmid constructs MigR1-PHGDH-IRES-EGFP (OE-PHGDH) and control vector MigR1-IRES-EGFP (EV) were used to transfect 293T cells together with pCMV-VSVG (Addgene). Retrovirus-containing supernatants were cleared by 0.45µm filtration and mixed with polybrene. Naive $CD8^+$ $Thy1.1^+$ OT-I T cells were stimulated with plate bound anti-CD3 (2ug/ml) and anti-CD28 (1ug/ml) for one day. Activated T cells were spin transduced with the EV or OE-PHGDH retroviral particles. After 24h incubation, cell culture media containing 50U/ml IL-2 was replaced and cells expanded for additional 24h before GFP-FACS-sorting. Cells were rested for 24h and then adoptively transferred into C57BL/6 mice (5000 cells/mouse in 200ul). One day later, mice were intravenously infected with attenuated LmOVA. Splenocytes were isolated from mice 7 dpi, and analyzed for the presence Thy1.1- and GFP^+ cells, for effector subset distribution based and KLRG1-and IL7R-positivity and for presence of intracellular cytokines. Furthermore, blood was sampled at indicated timepoints after infection to analyze percentage of adoptively transferred $Thy1.1^+$ GFP^+ cells of all $CD8^+$ T cells

7.3 QUANTIFICATION AND STATISTICAL ANALYSIS

All plots, curve fitting, and statistical analysis were carried out with GraphPad Prism. *P* values of less than 0.05 were considered statistically significant.

8. ACKNOWLEDGMENTS

This work would not have been possible without the support and contribution of many collaborators and friends. Therefore, I would like to express my gratitude and give credit to all the persons who helped me on this journey and took their time to teach me something along the way.

First and foremost, I would like to express my sincere gratitude to my supervisor and mentor Christoph Hess. In June 2014 I first stepped into his office and applied for a master thesis – this represented the start of an intensive 6 year long journey. During all this time, I received guidance and ongoing support from him also when the lab evolved and he became responsible of a second research group in Cambridge. He has given me the freedom and trust to tackle the research questions I thought to be interesting and had faith in me, even when I did not. Furthermore, I highly appreciate his mutual learning/teaching mentality. He taught me to have the courage to propose an idea and stand up for it even when others had their doubts. He shared his valuable knowledge about writing, reviewing and storytelling with me and reminded me that it is a privilege to do science when I forgot it. On the other hand, he was also a good listener. One of the first things he told me was that I should teach him things as well, which I hope I did achieve along the way. I have rarely seen a science enthusiast as him and he showed me how passion precedes hard work. Taken together, his huge enthusiasm for science, endless time for discussions and guidance over the years combined with trust in myself made me become the scientist I am today. I could not have asked for a better supervisor and feel very lucky to have gotten this opportunity to work with him and I hope we will continue some projects in the future.

My first steps in the lab as a master student were supervised by Sarah Dimeloe, who was a post-doc in the lab at that time. Beside teaching me how to pipet and isolate T cells from buffy coats, she showed me that having a life beside the lab is possible with good organizational skills and planning. I'm very grateful for everything she has done for me and always happy if we can catch up, discussing research and life in general.

When starting as a PhD student in the lab, I got trained by Glenn Bantug. Initially, we were discussing mainly technical aspects of experiments whereas with the years our discussions moved on to concepts and ideas while there was always time for some jokes as well. He represented a bottomless reservoir of great ideas and visions, where I had the privilege to decide on what to follow up on. Furthermore, he took his time to go through every report and

grant application I wrote leaving me with the choice of a hard or soft edit. I would like to express my deepest gratitude for everything he showed and taught me and believe me, it is a lot!

Especially during the last period of my PhD I received tremendous support from Marco Geigges, the most exact bio-informatician I know. Every RNA-sequencing experiment in this thesis went through his hands and computer. He mapped the reads to the reference genome, did statistical analysis and provided my with innumerable count tables. During a myriad of zoom talks, we discussed the seemingly never ending amount of data. Thank you very much for all your important contributions, this would not have been possible without you.

After one year into my PhD, I got the opportunity to widen my horizon and to get training in 'stable isotope tracing' in the lab of Russell Jones in Montreal. There, Eric Ma introduced me into this technique and kindly showed me around. Furthermore, Eric has performed all the *in vivo* experiments described in this thesis, which represents a huge amount of work. The adoptive transfer experiment took at least three attempts, but with his incredible persistence and endurance he revealed a very interesting phenotype. I enjoyed his visit to Basel a lot and I am very grateful for all the hard work he put into this project. Hopefully I can give him back something one day.

I have been very luck to work with exceptional lab-colleagues which surrounded me on a daily basis. During the lockdown and the writing period I realized what these daily interactions actually meant for me.
Beside all the social aspects, I want to thank:

- Rebekah Steiner for tirelessly working on keeping the lab tidy, taking care of the ordering and activation-beads production. Beside her invaluable organizational help, she was always a source of positive energy - just don’t forget your lab duty...
- Gunhild Unterstab for being the best imaginable desk partner, for all the coffees, chats, expertise and for being the most trustworthy captain of the Immunobiology-ship steering us through the biggest storms.
- Nadine Assmann for showing me how exact our inexact biological experiments at best can be and for always telling me what she was thinking (at least I guess she did...). This included the sharing of daily tips and trick as well as pointing out no-go's in the lab. I am very grateful to be aware of them by now!

- Jasmin Grählert for all the vocal entertainment in the cell-culture hood, for being around since the beginning, for all the unforgettable evenings and for taking care that it never got boring.
- Philippe Dehio for all the stimulating scientific discussions, jokes, rhymes, beats and lyrics as well as the tea times.
- Jonas Lötscher for being my lab-brother from another mother. Besides having the same abbreviation names, many people confused us, even some which knew us for years, which somehow indicates our resemblance. As we studied medicine together and started in the lab at around the same time, it felt like we always sat in the same boat, having similar issues at different stages of the PhD. I highly appreciate his company during this journey and hope it will continue beyond. Thank you very much for the friendship, runs, advice and always fair and healthy competition.
- Sophia Wiedemann for being a key constant during these 6 years at the DBM. Already as a master student I got a desk next to her and during all these years, we attended many events together. Furthermore, I want to thank her for the great collaboration during my first project, which in the end became my MD-thesis. I highly appreciated working with her and I was always impressed by her organizational skills, efficiency and multitasking abilities.
- Furthermore I want to acknowledge the former lab members Anne-Valérie Burgener, Marco Fischer, Bojana Durovic-Müller, Maria Balmer and Patrick Gubser and wish all the master-students I good start in their future positions.

As an open space lab, we were very fortunate with our neighbors - for the most part at least (luckily noise cancelling headphones were invented early during my PhD). From the Guzmann-group, I want to especially acknowledge Nilabh Gosh, for being the most reliable weekend company in the lab and taking me at the hand during my first Western blot. From the Heim-group, I want to give special credit to Alexsei Suslow for persistent good advice and organizing the Sola-runs and Chen Qian, a very experienced scientist, who always knew an answer to my questions.

Special thanks go also to Thorsten Schäfer for introducing me to molecular biology including cloning and lentivirus production. I'm very grateful for everything he taught me, all the interest he had for my project, the discussions, critical advice, bad jokes and contagious enthusiasm for research.

In the early days of my PhD, I also spent a lot of time in the fourth floor of the DBM. Special thanks go to Urs Duthaler for introducing me to mass-spectrometry, for giving me the trust to use his holy machines on my own and for being a friend. Without the generosity of Prof. Stephan Krähenbühl all the amino acid measurements would not have been possible and over the years the whole Immunobiology-lab benefited from the possibility to finally measure metabolites in-house. Furthermore, it was great to have a connection to a pharmacology lab that existed since many, many years since they had nearly every imaginable compound. Ahh and I nearly forgot, I still have one of your keys.

The flow cytometry facility is also located on the fourth floor, where I spent many hours. For every experiment with primary cells, I needed to FACS-sort my beloved subsets. Without the support of the flow team, including Telma Lopes, Emmanuel Traunecker, Lorenzo Raeli and Danni Labes this would not have been possible. I am very thankful for all their help, the chats during the sorts and general assistance with flow cytometry. Only their flexibility and willingness to sort T cell subsets from 6 human donors during one morning at three machines in parallel made some of the experiments feasible.

Additionally, I want to give credit to Robert Ivanek, the head of the bio-informatics facility at the DBM. Numerous discussions with him taught me, that sometimes thinking instead of speaking makes a lot of sense. Furthermore, I highly appreciated his critical input and advice. Also, I would like to thank Olivier Bignucolo for sharing his knowledge about *in silico* modeling with me and for the beautiful structural models of PHGDH and GAPDH.

Notably, I would like to give credit to Lukas Jeker, Romina Marone and Marcel Trefny for their help during the first CRISPR-experiments and subsequently for providing the whole lab with Cas9 protein. Furthermore, I always enjoyed 'joint labmeetings' and company of members from the Recher-, Berger-, Caveliti-, Mehling-, King-, Zippelius-, Donath- and Bentires-groups.

Due to the development of my project and the proximity, I also spent quite some time at the Biozentrum in Basel where many great scientist sheared their knowledge with me. First, I want to thank the various members of the Hall-group for sharing their insight and expertise about mTOR signaling. Special thanks go to Mitsugu Shimobayashi for inviting me to their seminar and giving me the opportunity to present my work to TOR-experts. When transitioning into the RNA-binding world, I got very helpful inputs from Nitish Mittal, who always had an open door and took his time to discuss my experiments. By chance I also encountered Dietmar Schreiner with whom I could philosophize about the pros and cons of irCliP, PAR-CliP, RIP, RIC, 2C-

capture, OOPS, RICK and all the other emerging RNA-interactome capture techniques. From time to time I also passed by the proteomics facility, where I want to acknowledge Alexander Schmidt, who helped me with proteomics-, OOPS- and pulldown experiments, which unfortunately did not make it into this thesis. Last but not least, I want to thank the team of the Genomics facility: Christian Beisel for helping me with the design of the sequencing experiments and Philippe Demougin for preparing cDNA libraries and organizing the sequencing in spite of a worldwide pandemic.

Further, I want to thank all the blood donors and the staff of the blood donation center in Basel for providing me with cells.

Beside all this help on mainly a scientific level, I want to acknowledge my family and friends for continues support. Most importantly, I would like to express my gratitude to my girlfriend Kathrin Bausch. She stood at my side during all of these years and listened to me when I was excited about something but also when I was struggling. Her love and patience were the best imaginable support I could get and she definitely would deserve to be listed as a co-author on my paper. Further, I am very grateful to my parents Michaela Neuwirth and Christian Löliger, my siblings Sabine, David and Rahel as well as my grandparents Helene und Josef Neuwirth as well as Lucile and Hans Löliger. Thank you all for being such a great family! I want also thank my longstanding friends Lorenz Hofer, Joel Pregger und Marius Elkuch for being one of the biggest constants of my life and for all the time and adventures, where science was not important at all.

Last but not least, I want to thank my PhD-Comitee consisting of Prof. Christoph Hess, Prof. Stephan Krähenbühl, Prof. Markus Rüegg and Prof. Olivier Mühlemann. Thank you very much for your time and guidance during my PhD. Furthermore, I am very happy and grateful that Prof. Daniel Ricklin accepted to be the chair of my PhD Defence.

9. REFERENCES

Abdelfattah, F., Kariminejad, A., Kahlert, A.K., Morrison, P.J., Gumus, E., Mathews, K.D., Darbro, B.W., Amor, D.J., Walsh, M., Sznajer, Y., et al. (2020). Expanding the genotypic and phenotypic spectrum of severe serine biosynthesis disorders. Hum. Mutat.

Abdelsamed, H.A., Moustaki, A., Fan, Y., Dogra, P., Ghoneim, H.E., Zebley, C.C., Triplett, B.M., Sekaly, R.-P., and Youngblood, B. (2017). Human memory CD8 T cell effector potential is epigenetically preserved during in vivo homeostasis. J. Exp. Med. *214*, 1593–1606.

Acuna-Hidalgo, R., Schanze, D., Kariminejad, A., Nordgren, A., Kariminejad, M.H., Conner, P., Grigelioniene, G., Nilsson, D., Nordenskjöld, M., Wedell, A., et al. (2014). Neu-Laxova syndrome is a heterogeneous metabolic disorder caused by defects in enzymes of the L-serine biosynthesis pathway. Am. J. Hum. Genet. *95*, 285–293.

Adams, D., Altucci, L., Antonarakis, S.E., Ballesteros, J., Beck, S., Bird, A., Bock, C., Boehm, B., Campo, E., Caricasole, A., et al. (2012). BLUEPRINT to decode the epigenetic signature written in blood. Nat. Biotechnol. *30*, 224–226.

Araki, Y., Wang, Z., Zang, C., Wood, W.H., Schones, D., Cui, K., Roh, T.-Y., Lhotsky, B., Wersto, R.P., Peng, W., et al. (2009). Genome-wide analysis of histone methylation reveals chromatin state-based regulation of gene transcription and function of memory CD8+ T cells. Immunity *30*, 912–925.

Arstila, T.P., Casrouge, A., Baron, V., Even, J., Kanellopoulos, J., and Kourilsky, P. (1999). A direct estimate of the human alphabeta T cell receptor diversity. Science *286*, 958–961.

Baker, N.A., Sept, D., Joseph, S., Holst, M.J., and McCammon, J.A. (2001). Electrostatics of nanosystems: application to microtubules and the ribosome. Proceedings of the National Academy of Sciences *98*, 10037–10041.

Baltz, A.G., Munschauer, M., Schwanhäusser, B., Vasile, A., Murakawa, Y., Schueler, M., Youngs, N., Penfold-Brown, D., Drew, K., Milek, M., et al. (2012). The mRNA-Bound Proteome and Its Global Occupancy Profile on Protein-Coding Transcripts. Mol. Cell *46*, 674–690.

Bantug, G.R., Fischer, M., Grählert, J., Balmer, M.L., Unterstab, G., Develioglu, L., Steiner, R., Zhang, L., Costa, A.S.H., Gubser, P.M., et al. (2018). Mitochondria-Endoplasmic Reticulum Contact Sites Function as Immunometabolic Hubs that Orchestrate the Rapid Recall Response of Memory CD8+ T Cells. Immunity *48*, 1–35.

Bao, X., Guo, X., Yin, M., Tariq, M., Lai, Y., Kanwal, S., Zhou, J., Li, N., Lv, Y., Pulido-Quetglas, C., et al. (2018). Capturing the interactome of newly transcribed RNA. Nature Publishing Group *15*, 213–220.

Bolger, A.M., Lohse, M., and Usadel, B. (2014). Trimmomatic: a flexible trimmer for Illumina sequence data. Bioinformatics *30*, 2114–2120.

Brannan, K.W., Jin, W., Huelga, S.C., Banks, C.A.S., Gilmore, J.M., Florens, L., Washburn, M.P., Van Nostrand, E.L., Pratt, G.A., Schwinn, M.K., et al. (2016). SONAR Discovers RNA-Binding Proteins from Analysis of Large-Scale Protein-Protein Interactomes. Mol. Cell *64*, 282–293.

Breitman, T.R., Selonick, S.E., and Collins, S.J. (1980). Induction of differentiation of the human promyelocytic leukemia cell line (HL-60) by retinoic acid. Proceedings of the National Academy of Sciences *77*, 2936–2940.

Buccitelli, C., and Selbach, M. (2020). mRNAs, proteins and the emerging principles of gene expression control. Nature Reviews Genetics *204*, 1–15.

Buck, M.D., O'Sullivan, D., Klein Geltink, R.I., Curtis, J.D., Chang, C.-H., Sanin, D.E., Qiu, J., Kretz, O., Braas, D., van der Windt, G.J.W., et al. (2016). Mitochondrial Dynamics Controls T Cell Fate through Metabolic Programming. Cell *166*, 63–76.

Castello, A., Fischer, B., Eichelbaum, K., Horos, R., Beckmann, B.M., Strein, C., Davey, N.E., Humphreys, D.T., Preiss, T., Steinmetz, L.M., et al. (2012). Insights into RNA biology from an atlas of mammalian mRNA-binding proteins. Cell *149*, 1393–1406.

Castello, A., Fischer, B., Frese, C.K., Horos, R., Alleaume, A.-M., Foehr, S., Curk, T., Krijgsveld, J., and Hentze, M.W. (2016). Comprehensive Identification of RNA-Binding Domains in Human Cells. Mol. Cell *63*, 696–710.

Castello, A., Hentze, M.W., and Preiss, T. (2015). Metabolic Enzymes Enjoying New Partnerships as RNA-Binding Proteins. Trends in Endocrinology & Metabolism *26*, 746–757.

Chang, C.-H., Curtis, J.D., Maggi, L.B., Faubert, B., Villarino, A.V., O'Sullivan, D., Huang, S.C.-C., van der Windt, G.J.W., Blagih, J., Qiu, J., et al. (2013). Posttranscriptional control of T cell effector function by aerobic glycolysis. Cell *153*, 1239–1251.

Chang, J.T., Wherry, E.J., and Goldrath, A.W. (2014). Molecular regulation of effector and memory T cell differentiation. Nature Immunology *15*, 1104–1115.

Chanput, W., Mes, J.J., and Wichers, H.J. (2014). THP-1 cell line: An in vitro cell model for immune modulation approach. International Immunopharmacology *23*, 37–45.

Chapman, N.M., Boothby, M.R., and Chi, H. (2019). Metabolic coordination of T cell quiescence and activation. Nat. Rev. Immunol. *12*, 1–16.

Corley, M., Burns, M.C., and Yeo, G.W. (2020). How RNA-Binding Proteins Interact with RNA: Molecules and Mechanisms. Mol. Cell *78*, 9–29.

Cox, J., and Mann, M. (2008). MaxQuant enables high peptide identification rates, individualized p.p.b.-range mass accuracies and proteome-wide protein quantification. Nature Publishing Group *26*, 1367–1372.

de Koning, T.J. (2017). Amino acid synthesis deficiencies. J Inherit Metab Dis *40*, 609–620.

Diehl, F.F., Lewis, C.A., Fiske, B.P., and Vander Heiden, M.G. (2019). Cellular redox state constrains serine synthesis and nucleotide production to impact cell proliferation. Nature Metabolism *1*, 861–867.

Díaz-Muñoz, M.D., and Turner, M. (2018). Uncovering the Role of RNA-Binding Proteins in Gene Expression in the Immune System. Front Immunol *9*, 1–16.

Díaz-Muñoz, M.D., Bell, S.E., Fairfax, K., Monzón-Casanova, E., Cunningham, A.F., Gonzalez-Porta, M., Andrews, S.R., Bunik, V.I., Zarnack, K., Curk, T., et al. (2015). The RNA-

binding protein HuR is essential for the B cell antibody response. Nature Immunology *16*, 415–425.

Dobin, A., Davis, C.A., Schlesinger, F., Drenkow, J., Zaleski, C., Jha, S., Batut, P., Chaisson, M., and Gingeras, T.R. (2013). STAR: ultrafast universal RNA-seq aligner. Bioinformatics *29*, 15–21.

Dotti, I., Mora-Buch, R., Ferrer-Picón, E., Planell, N., Jung, P., Masamunt, M.C., Leal, R.F., Martín de Carpi, J., Llach, J., Ordás, I., et al. (2017). Alterations in the epithelial stem cell compartment could contribute to permanent changes in the mucosa of patients with ulcerative colitis. Gut *66*, 2069–2079.

Farber, D.L., Yudanin, N.A., and Restifo, N.P. (2014). Human memory T cells: generation, compartmentalization and homeostasis. Nature Publishing Group *14*, 24–35.

Fischer, M., Bantug, G.R., Dimeloe, S., Gubser, P.M., Burgener, A.-V., Grählert, J., Balmer, M.L., Develioglu, L., Steiner, R., Unterstab, G., et al. (2018). Early effector maturation of naïve human CD8 +T cells requires mitochondrial biogenesis. Eur. J. Immunol. *48*, 1632–1643.

Fischer, M., Grossmann, P., Padi, M., and DeCaprio, J.A. (2016). Integration of TP53, DREAM, MMB-FOXM1 and RB-E2F target gene analyses identifies cell cycle gene regulatory networks. Nucleic Acids Res *44*, 6070–6086.

Fu, X.-D., and Ares, M. (2014). Context-dependent control of alternative splicing by RNA-binding proteins. Nature Reviews Genetics *15*, 689–701.

Gaidatzis, D., Lerch, A., Hahne, F., and Stadler, M.B. (2015). QuasR: quantification and annotation of short reads in R. Bioinformatics *31*, 1130–1132.

Garcin, E.D. (2019). GAPDH as a model non-canonical AU-rich RNA binding protein. Seminars in Cell & Developmental Biology *86*, 162–173.

García-Mauriño, S.M., Rivero-Rodríguez, F., Velázquez-Cruz, A., Hernández-Vellisca, M., Díaz-Quintana, A., la Rosa, De, M.A., and Díaz-Moreno, I. (2017). RNA Binding Protein Regulation and Cross-Talk in the Control of AU-rich mRNA Fate. Front. Mol. Biosci. *4*, 1271–1279.

Ghosh, M., Aguila, H.L., Michaud, J., Ai, Y., Wu, M.-T., Hemmes, A., Ristimaki, A., Guo, C., Furneaux, H., and Hla, T. (2009). Essential role of the RNA-binding protein HuR in progenitor cell survival in mice. J. Clin. Invest. *119*, 3530–3543.

Gioia, L., Siddique, A., Head, S.R., Salomon, D.R., and Su, A.I. (2018). A genome-wide survey of mutations in the Jurkat cell line. BMC Genomics *19*, 334.

Goberdhan, D.C.I., Wilson, C., and Harris, A.L. (2016). Amino Acid Sensing by mTORC1: Intracellular Transporters Mark the Spot. Cell Metabolism *23*, 580–589.

Grant, G.A. (2018). D-3-Phosphoglycerate Dehydrogenase. Front. Mol. Biosci. *5*, 1928–18.

Gromova, I., Gromov, P., Honma, N., Kumar, S., Rimm, D., Talman, M.-L.M., Wielenga, V.T., and Moreira, J.M.A. (2015). High level PHGDH expression in breast is predominantly associated with keratin 5-positive cell lineage independently of malignancy. Molecular Oncology *9*, 1636–1654.

Gubser, P.M., Bantug, G.R., Razik, L., Fischer, M., Dimeloe, S., Hoenger, G., Durovic, B., Jauch, A., and Hess, C. (2013). Rapid effector function of memory CD8+ T cells requires an immediate-early glycolytic switch. Nature Immunology *14*, 1064–1072.

Harty, J.T., and Badovinac, V.P. (2008). Shaping and reshaping CD8+ T-cell memory. Nature Publishing Group *8*, 107–119.

Hentze, M.W., and Preiss, T. (2010). The REM phase of gene regulation. Trends Biochem. Sci. *35*, 423–426.

Hentze, M.W., Castello, A., Schwarzl, T., and Preiss, T. (2018). A brave new world of RNA-binding proteins. Nat. Rev. Mol. Cell Biol. *19*, 327–341.

Hitti, E., Bakheet, T., Al-Souhibani, N., Moghrabi, W., Al-Yahya, S., Al-Ghamdi, M., Al-Saif, M., Shoukri, M.M., Lánczky, A., Grépin, R., et al. (2016). Systematic Analysis of AU-Rich Element Expression in Cancer Reveals Common Functional Clusters Regulated by Key RNA-Binding Proteins. Cancer Res. *76*, 4068–4080.

Hosios, A.M., Hecht, V.C., Danai, L.V., Johnson, M.O., Rathmell, J.C., Steinhauser, M.L., Manalis, S.R., and Vander Heiden, M.G. (2016). Amino Acids Rather than Glucose Account for the Majority of Cell Mass in Proliferating Mammalian Cells. Developmental Cell *36*, 540–549.

Huang, X., Tanaka, T., Kurose, A., Traganos, F., and Darzynkiewicz, Z. (2006). Constitutive histone H2AX phosphorylation on Ser-139 in cells untreated by genotoxic agents is cell-cycle phase specific and attenuated by scavenging reactive oxygen species. Int. J. Oncol. *29*, 495–501.

Humphrey, W., Dalke, A., and Schulten, K. (1996). VMD: visual molecular dynamics. J Mol Graph *14*, 33–8–27–8.

IDT Amaxa, I.D.T. (2018). Alt-R CRISPR-Cas9 System protocol: Delivery of RNP complexes into HEK-293 cells using the Amaxa® Nucleofector® System (CRS-10055-PR, v3). 1–10.

Jameson, S.C., and Masopust, D. (2018). Understanding Subset Diversity in T Cell Memory. Immunity *48*, 214–226.

Jones, R.G., Plas, D.R., Kubek, S., Buzzai, M., Mu, J., Xu, Y., Birnbaum, M.J., and Thompson, C.B. (2005). AMP-Activated Protein Kinase Induces a p53-Dependent Metabolic Checkpoint. Mol. Cell *18*, 283–293.

Jung, H., Lee, D., Lee, J., Park, D., Kim, Y.J., Park, W.-Y., Hong, D., Park, P.J., and Lee, E. (2015). Intron retention is a widespread mechanism of tumor-suppressor inactivation. Nature Publishing Group *47*, 1–10.

Jung, J., Zeng, H., and Horng, T. (2019). Metabolism as a guiding force for immunity. Nat Cell Biol *21*, 85–93.

Katsanou, V., Milatos, S., Yiakouvaki, A., Sgantzis, N., Kotsoni, A., Alexiou, M., Harokopos, V., Aidinis, V., Hemberger, M., and Kontoyiannis, D.L. (2009). The RNA-binding protein Elavl1/HuR is essential for placental branching morphogenesis and embryonic development. Mol. Cell. Biol. *29*, 2762–2776.

Keene, J.D. (2007). RNA regulons: coordination of post-transcriptional events. Nature Reviews Genetics *8*, 533–543.

Kent, W.J., Sugnet, C.W., Furey, T.S., Roskin, K.M., Pringle, T.H., Zahler, A.M., and Haussler, D. (2002). The human genome browser at UCSC. Genome Res. *12*, 996–1006.

Kilchert, C., Sträßer, K., Kunetsky, V., and Anko, M.-L. (2019). From parts lists to functional significance—RNA–protein interactions in gene regulation. WIREs RNA *2014*, 52230–20.

Kim, D., Pertea, G., Trapnell, C., Pimentel, H., Kelley, R., and Salzberg, S.L. (2013). TopHat2: accurate alignment of transcriptomes in the presence of insertions, deletions and gene fusions. Genome Biol. *14*, R36–13.

Kinoshita, M.O., Shinoda, Y., Sakai, K., Hashikawa, T., Watanabe, M., Machida, T., Hirabayashi, Y., and Furuya, S. (2009). Selective upregulation of 3-phosphoglycerate dehydrogenase (Phgdh) expression in adult subventricular zone neurogenic niche. Neurosci. Lett. *453*, 21–26.

Lawrence, M., Gentleman, R., and Carey, V. (2009). rtracklayer: an R package for interfacing with genome browsers. Bioinformatics *25*, 1841–1842.

Lawrence, M., Huber, W., Pagès, H., Aboyoun, P., Carlson, M., Gentleman, R., Morgan, M.T., and Carey, V.J. (2013). Software for computing and annotating genomic ranges. PLoS Comput Biol *9*, e1003118.

Laxova, R., OHARA, P.T., and Timothy, J.A. (1972). A further example of a lethal autosomal recessive condition in sibs. J Ment Defic Res *16*, 139–143.

Li, H., Handsaker, B., Wysoker, A., Fennell, T., Ruan, J., Homer, N., Marth, G., Abecasis, G., Durbin, R., 1000 Genome Project Data Processing Subgroup (2009). The Sequence Alignment/Map format and SAMtools. Bioinformatics *25*, 2078–2079.

Liao, Y., Castello, A., Fischer, B., Leicht, S., Foehr, S., Frese, C.K., Ragan, C., Kurscheid, S., Pagler, E., Yang, H., et al. (2016). The Cardiomyocyte RNA-Binding Proteome: Links to Intermediary Metabolism and Heart Disease. Cell Rep *16*, 1456–1469.

Liao, Y., Smyth, G.K., and Shi, W. (2019). The R package Rsubread is easier, faster, cheaper and better for alignment and quantification of RNA sequencing reads. Nucleic Acids Res *47*, e47.

Liu, J., Guo, S., Li, Q., Yang, L., Xia, Z., Zhang, L., Huang, Z., and Zhang, N. (2013). Phosphoglycerate dehydrogenase induces glioma cells proliferation and invasion by stabilizing forkhead box M1. J Neurooncol *111*, 245–255.

Locasale, J.W., Grassian, A.R., Melman, T., Lyssiotis, C.A., Mattaini, K.R., Bass, A.J., Heffron, G., Metallo, C.M., Muranen, T., Sharfi, H., et al. (2011). Phosphoglycerate dehydrogenase diverts glycolytic flux and contributes to oncogenesis. Nat. Genet. *43*, 869–874.

Love, M.I., Huber, W., and Anders, S. (2014). Moderated estimation of fold change and dispersion for RNA-seq data with DESeq2. Genome Biol. *15*, 550.

Lowman, X.H., Hanse, E.A., Yang, Y., Gabra, M.B.I., Tran, T.Q., Li, H., and Kong, M. (2019). p53 Promotes Cancer Cell Adaptation to Glutamine Deprivation by Upregulating Slc7a3 to Increase Arginine Uptake. Cell Rep *26*, 3051–3060.e3054.

Lu, Y.-C., Chang, S.-H., Hafner, M., Li, X., Tuschl, T., Elemento, O., and Hla, T. (2014). ELAVL1 Modulates Transcriptome-wide miRNA Binding in Murine Macrophages. Cell Rep *9*, 2330–2343.

Lugli, E., Ji, Y., Pos, Z., Paulos, C.M., Quigley, M.A.I.F., Almeida, J.R., Gostick, E., Yu, Z., Carpenito, C., Wang, E., et al. (2011). A human memory T cell subset with stem cell-like properties. Nat. Med. *17*, 1290–1297.

Lund, S.P., Nettleton, D., McCarthy, D.J., and Smyth, G.K. (2012). Detecting differential expression in RNA-sequence data using quasi-likelihood with shrunken dispersion estimates. Stat Appl Genet Mol Biol *11*.

Ma, E.H., Bantug, G., Griss, T., Condotta, S., Johnson, R.M., Samborska, B., Mainolfi, N., Suri, V., Guak, H., Balmer, M.L., et al. (2017). Serine Is an Essential Metabolite for Effector T Cell Expansion. Cell Metabolism *25*, 1–14.

Ma, E.H., Verway, M.J., Johnson, R.M., Roy, D.G., Steadman, M., Hayes, S., Williams, K.S., Sheldon, R.D., Samborska, B., Kosinski, P.A., et al. (2019a). Metabolic Profiling Using Stable Isotope Tracing Reveals Distinct Patterns of Glucose Utilization by Physiologically Activated CD8+ T Cells. Immunity *51*, 856–870.e5.

Ma, X., Li, B., Liu, J., Fu, Y., and Luo, Y. (2019b). Phosphoglycerate dehydrogenase promotes pancreatic cancer development by interacting with eIF4A1 and eIF4E. J Exp Clin Cancer Res *38*, 1–15.

Maciver, N.J., Michalek, R.D., and Rathmell, J.C. (2013). Metabolic regulation of T lymphocytes. Annu. Rev. Immunol. *31*, 259–283.

Maddocks, O.D.K., Berkers, C.R., Mason, S.M., Zheng, L., Blyth, K., Gottlieb, E., and Vousden, K.H. (2013). Serine starvation induces stress and p53-dependent metabolic remodelling in cancer cells. Nature *493*, 542–546.

Mah, L.-J., El-Osta, A., and Karagiannis, T.C. (2010). gammaH2AX: a sensitive molecular marker of DNA damage and repair. Leukemia *24*, 679–686.

Man, K., and Kallies, A. (2015). Synchronizing transcriptional control of T cell metabolism and function. Nat. Rev. Immunol. *15*, 574–584.

Mattaini, K.R., Brignole, E.J., Kini, M., Davidson, S.M., Fiske, B.P., Drennan, C.L., and Vander Heiden, M.G. (2015). An epitope tag alters phosphoglycerate dehydrogenase structure and impairs ability to support cell proliferation. Cancer Metab *3*, 5.

McGuirk, S., Gravel, S.-P., Deblois, G., Papadopoli, D.J., Faubert, B., Wegner, A., Hiller, K., Avizonis, D., Akavia, U.D., Jones, R.G., et al. (2013). PGC-1α supports glutamine metabolism in breast cancer. Cancer Metab *1*, 22–11.

Monzón-Casanova, E., Matheson, L.S., Tabbada, K., Zarnack, K., Smith, C.W., and Turner, M. (2020). Polypyrimidine tract-binding proteins are essential for B cell development. eLife *9*, 613–628.

Nagy, E., Henics, T., Eckert, M., Miseta, A., Lightowlers, R.N., and Kellermayer, M. (2000). Identification of the NAD(+)-binding fold of glyceraldehyde-3-phosphate dehydrogenase as a novel RNA-binding domain. Biochemical and Biophysical Research Communications *275*, 253–260.

Neu, R.L., Kajii, T., Gardner, L.I., and Nagyfy, S.F. (1971). A lethal syndrome of microcephaly with multiple congenital anomalies in three siblings. Pediatrics *47*, 610–612.

Newman, A.C., and Maddocks, O.D.K. (2017). Serine and Functional Metabolites in Cancer. Trends Cell Biol. *27*, 1–13.

Ngo, B., Kim, E., Osorio-Vasquez, V., Doll, S., Bustraan, S., Luengo, A., Davidson, S.M., Ali, A., Ferraro, G.D., Kang, D., et al. (2020). Limited Environmental Serine Confers Sensitivity to PHGDH Inhibition in Brain Metastasis. bioRxiv *376*, 2109–2127.

Nostrand, E.L., Freese, P., Pratt, G.A., Wang, X., Wei, X., Xiao, R., Blue, S.M., Chen, J.-Y., Cody, N.A.L., Dominguez, D., et al. (2020). A large-scale binding and functional map of human RNA-binding proteins. Nature *583*, 1–39.

O'Sullivan, D., van der Windt, G.J.W., Huang, S.C.-C., Curtis, J.D., Chang, C.-H., Buck, M.D., Qiu, J., Smith, A.M., Lam, W.Y., DiPlato, L.M., et al. (2014). Memory CD8(+) T cells use cell-intrinsic lipolysis to support the metabolic programming necessary for development. Immunity *41*, 75–88.

Obar, J.J., and Lefrançois, L. (2010). Memory CD8+ T cell differentiation. Ann. N.Y. Acad. Sci. *1183*, 251–266.

Olenchock, B.A., Rathmell, J.C., and Vander Heiden, M.G. (2017). Biochemical Underpinnings of Immune Cell Metabolic Phenotypes. Immunity *46*, 703–713.

Pacold, M.E., Brimacombe, K.R., Chan, S.H., Rohde, J.M., Lewis, C.A., Swier, L.J.Y.M., Possemato, R., Chen, W.W., Sullivan, L.B., Fiske, B.P., et al. (2016). A PHGDH inhibitor reveals coordination of serine synthesis and one-carbon unit fate. Nat. Chem. Biol. *12*, 452–458.

Pakos Zebrucka, K., Koryga, I., Mnich, K., Ljujic, M., Samali, A., and Gorman, A.M. (2016). The integrated stress response. EMBO Rep. *17*, 1374–1395.

Papadaki, O., Milatos, S., Grammenoudi, S., Mukherjee, N., Keene, J.D., and Kontoyiannis, D.L. (2009). Control of Thymic T Cell Maturation, Deletion and Egress by the RNA-Binding Protein HuR. The Journal of Immunology *182*, 6779–6788.

Pelletier, J., Riaño Canalias, F., Almacellas, E., Mauvezin, C., Samino, S., Feu, S., Menoyo, S., Domostegui, A., Garcia Cajide, M., Salazar, R., et al. (2020). Nucleotide depletion reveals the impaired ribosome biogenesis checkpoint as a barrier against DNA damage. The EMBO Journal *39*, e103838.

Phan, A.T., Goldrath, A.W., and Glass, C.K. (2017). Metabolic and Epigenetic Coordination of T Cell and Macrophage Immunity. Immunity *46*, 714–729.

Porter, J.R., Fisher, B.E., Baranello, L., Liu, J.C., Kambach, D.M., Nie, Z., Koh, W.S., Luo, J., Stommel, J.M., Levens, D., et al. (2017). Global Inhibition with Specific Activation: How p53 and MYC Redistribute the Transcriptome in the DNA Double-Strand Break Response. Mol. Cell *67*, 1013–1025.e1019.

Possemato, R., Marks, K.M., Shaul, Y.D., Pacold, M.E., Kim, D., Birsoy, K., Sethumadhavan, S., Woo, H.K., Jang, H.G., Jha, A.K., et al. (2011). Functional genomics reveal that the serine synthesis pathway is essential in breast cancer. Nature *476*, 346–350.

Preston, G.C., Sinclair, L.V., Kaskar, A., Hukelmann, J.L., Navarro, M.N., Ferrero, I., MacDonald, H.R., Cowling, V.H., and Cantrell, D.A. (2015). Single cell tuning of Myc expression by antigen receptor signal strength and interleukin-2 in T lymphocytes. The EMBO Journal *34*, 2008–2024.

Qi, Q., Liu, Y., Cheng, Y., Glanville, J., Zhang, D., Lee, J.-Y., Olshen, R.A., Weyand, C.M., Boyd, S.D., and Goronzy, J.J. (2014). Diversity and clonal selection in the human T-cell repertoire. Proc. Natl. Acad. Sci. U.S.a. *111*, 13139–13144.

Queiroz, R.M.L., Smith, T., Villanueva, E., Marti-Solano, M., Monti, M., Pizzinga, M., Mirea, D.-M., Ramakrishna, M., Harvey, R.F., Dezi, V., et al. (2019). Comprehensive identification of RNA–protein interactions in any organism using orthogonal organic phase separation (OOPS). Nat. Biotechnol. *37*, 1–18.

Robinson, J.T., Thorvaldsdóttir, H., Winckler, W., Guttman, M., Lander, E.S., Getz, G., and Mesirov, J.P. (2011). Integrative genomics viewer. Nat. Biotechnol. *29*, 24–26.

Robinson, M.D., McCarthy, D.J., and Smyth, G.K. (2010). edgeR: a Bioconductor package for differential expression analysis of digital gene expression data. Bioinformatics *26*, 139–140.

Ron-Harel, N., Santos, D., Ghergurovich, J.M., Sage, P.T., Reddy, A., Lovitch, S.B., Dephoure, N., Satterstrom, F.K., Sheffer, M., Spinelli, J.B., et al. (2016). Mitochondrial Biogenesis and Proteome Remodeling Promote One-Carbon Metabolism for T Cell Activation. Cell Metabolism *24*, 104–117.

Roretz, von, C., Di Marco, S., Mazroui, R., and Gallouzi, I.-E. (2011). Turnover of AU-rich-containing mRNAs during stress: a matter of survival. Wiley Interdiscip Rev RNA *2*, 336–347.

Rotondo, J.C., Bosi, S., Bassi, C., Ferracin, M., Lanza, G., Gafà, R., Magri, E., Selvatici, R., Torresani, S., Marci, R., et al. (2014). Gene Expression Changes in Progression of Cervical Neoplasia Revealed by Microarray Analysis of Cervical Neoplastic Keratinocytes. J. Cell. Physiol. *230*, 806–812.

Salerno, F., Engels, S., van den Biggelaar, M., van Alphen, F.P.J., Guislain, A., Zhao, W., Hodge, D.L., Bell, S.E., Medema, J.P., Lindern, von, M., et al. (2018). Translational repression of pre-formed cytokine-encoding mRNA prevents chronic activation of memory T cells. Nat. Immunol. *19*, 828–837.

Salerno, F., Turner, M., and Wolkers, M.C. (2020). Dynamic Post-Transcriptional Events Governing CD8+ T Cell Homeostasis and Effector Function. Trends in Immunology *41*, 240–254.

Sallusto, F., Lanzavecchia, A., Araki, K., and Ahmed, R. (2010). From vaccines to memory and back. Immunity *33*, 451–463.

Schmidt, E.K., Clavarino, G., Ceppi, M., and Pierre, P. (2009). SUnSET, a nonradioactive method to monitor protein synthesis. Nat. Methods *6*, 275–277.

Shaheen, R., Rahbeeni, Z., Alhashem, A., Faqeih, E., Zhao, Q., Xiong, Y., Almoisheer, A., Al-Qattan, S.M., Almadani, H.A., Al-Onazi, N., et al. (2014). REPOR T Neu-Laxova Syndrome, an Inborn Error of Serine Metabolism, Is Caused by Mutations in PHGDH. The American Journal of Human Genetics *94*, 898–904.

Sharif, T., Martell, E., Dai, C., Ghassemi-Rad, M.S., Lee, K., Singh, S.K., Weaver, I.C.G., and Gujar, S. (2018). Phosphoglycerate dehydrogenase inhibition induces p-mTOR-independent autophagy and promotes multilineage differentiation in embryonal carcinoma stem-like cells. Cell Death and Disease *9*, 1–17.

Sun, L., Song, L., Wan, Q., Wu, G., Li, X., Wang, Y., Wang, J., Liu, Z., Zhong, X., He, X., et al. (2015). cMyc-mediated activation of serine biosynthesis pathway is critical for cancer progression under nutrient deprivation conditions. Cell Res. *25*, 429–444.

Szklarczyk, D., Morris, J.H., Cook, H., Kuhn, M., Wyder, S., Simonovic, M., Santos, A., Doncheva, N.T., Roth, A., Bork, P., et al. (2017). The STRING database in 2017: quality-controlled protein-protein association networks, made broadly accessible. Nucleic Acids Res *45*, D362–D368.

Tabatabaie, L., de Koning, T.J., Geboers, A.J.J.M., van den Berg, I.E.T., Berger, R., and Klomp, L.W.J. (2009). Novel mutations in 3-phosphoglycerate dehydrogenase (PHGDH) are distributed throughout the protein and result in altered enzyme kinetics. Hum. Mutat. *30*, 749–756.

Takada, K., and Jameson, S.C. (2009). Naive T cell homeostasis: from awareness of space to a sense of place. Nat. Rev. Immunol. *9*, 823–832.

Tan, F.E., and Elowitz, M.B. (2014). Brf1 posttranscriptionally regulates pluripotency and differentiation responses downstream of Erk MAP kinase. Proc. Natl. Acad. Sci. U.S.a. *111*, E1740–E1748.

Tasseff, R., Jensen, H.A., Congleton, J., Dai, D., Rogers, K.V., Sagar, A., Bunaciu, R.P., Yen, A., and Varner, J.D. (2017). An Effective Model of the Retinoic Acid Induced HL-60 Differentiation Program. Sci Rep *7*, 1–21.

Trendel, J., Schwarzl, T., Horos, R., Prakash, A., Bateman, A., Hentze, M.W., and Krijgsveld, J. (2019). The Human RNA-Binding Proteome and Its Dynamics during Translational Arrest. Cell *176*, 391–403.e19.

Türker, C., Akal, F., Joho, D., Panse, C., Barkow-Oesterreicher, S., Rehrauer, H., and Schlapbach, R. (2010). B-Fabric: The Swiss Army Knife for life sciences. (New York, New York, USA: ACM Press), pp. 717–5.

Uhlen, M., Oksvold, P., Fagerberg, L., Lundberg, E., Jonasson, K., Forsberg, M., Zwahlen, M., Kampf, C., Wester, K., Hober, S., et al. (2010). Towards a knowledge-based Human Protein Atlas. Nature Publishing Group 1–3.

Unterlass, J.E., Wood, R.J., Baslé, A., Tucker, J., Cano, C., Noble, M.M.E., and Curtin, N.J. (2017). Structural insights into the enzymatic activity and potential substrate promiscuity of human 3-phosphoglycerate dehydrogenase (PHGDH). Oncotarget *8*, 104478–104491.

Urdaneta, E.C., Vieira-Vieira, C.H., Hick, T., Wessels, H.-H., Figini, D., Moschall, R., Medenbach, J., Ohler, U., Granneman, S., Selbach, M., et al. (2019). Purification of cross-linked RNA-protein complexes by phenol-toluol extraction. Nat Commun *10*, 1–17.

van Aalderen, M.C., van den Biggelaar, M., Remmerswaal, E.B.M., van Alphen, F.P.J., Meijer, A.B., Berge, ten, I.J.M., and van Lier, R.A.W. (2017). Label-free Analysis of CD8+ T Cell

Subset Proteomes Supports a Progressive Differentiation Model of Human-Virus-Specific T Cells. Cell Rep *19*, 1068–1079.

van der Windt, G.J.W., Everts, B., Chang, C.-H., Curtis, J.D., Freitas, T.C., Amiel, E., Pearce, E.J., and Pearce, E.L. (2012). Mitochondrial respiratory capacity is a critical regulator of CD8+ T cell memory development. Immunity *36*, 68–78.

Vlasova-St Louis, I., and Bohjanen, P.R. (2017). Post-transcriptional regulation of cytokine and growth factor signaling in cancer. Cytokine and Growth Factor Reviews *33*, 83–93.

Wang, H., Nakamura, M., Abbott, T.R., Zhao, D., Luo, K., Yu, C., Nguyen, C.M., Lo, A., Daley, T.P., La Russa, M., et al. (2019). CRISPR-mediated live imaging of genome editing and transcription. Science *365*, 1301–1305.

Weng, N.-P., Araki, Y., and Subedi, K. (2012). The molecular basis of the memory T cell response: differential gene expression and its epigenetic regulation. Nat. Rev. Immunol. *12*, 306–315.

White, M.R., and Garcin, E.D. (2015). The sweet side of RNA regulation: glyceraldehyde-3-phosphate dehydrogenase as a noncanonical RNA-binding protein. Wiley Interdiscip Rev RNA *7*, 53–70.

White, M.R., Khan, M.M., Deredge, D., Ross, C.R., Quintyn, R., Zucconi, B.E., Wysocki, V.H., Wintrode, P.L., Wilson, G.M., and Garcin, E.D. (2015). A dimer interface mutation in glyceraldehyde-3-phosphate dehydrogenase regulates its binding to AU-rich RNA. J. Biol. Chem. *290*, 1770–1785.

Wolf, T., Jin, W., Zoppi, G., Vogel, I.A., Akhmedov, M., Bleck, C.K.E., Beltraminelli, T., Rieckmann, J.C., Ramirez, N.J., Benevento, M., et al. (2020). Dynamics in protein translation sustaining T cell preparedness. Nat. Immunol. *243*, 1–23.

Yang, C., Khanniche, A., DiSpirito, J.R., Ji, P., Wang, S., Wang, Y., and Shen, H. (2016). Transcriptome Signatures Reveal Rapid Induction of Immune-Responsive Genes in Human Memory CD8+ T Cells. Sci Rep *6*, 1–8.

Yang, M., and Vousden, K.H. (2016). Serine and one-carbon metabolism in cancer. Nat. Rev. Cancer *16*, 650–662.

Ye, J., and Blelloch, R. (2014). Regulation of pluripotency by RNA binding proteins. Cell Stem Cell *15*, 271–280.

Yoshida, K., Furuya, S., Osuka, S., Mitoma, J., Shinoda, Y., Watanabe, M., Azuma, N., Tanaka, H., Hashikawa, T., Itohara, S., et al. (2004). Targeted Disruption of the Mouse 3-Phosphoglycerate Dehydrogenase Gene Causes Severe Neurodevelopmental Defects and Results in Embryonic Lethality. J. Biol. Chem. *279*, 3573–3577.

Zhang, B., Zheng, A., Hydbring, P., Ambroise, G., Ouchida, A.T., Goiny, M., Vakifahmetoglu-Norberg, H., and Norberg, E. (2017). PHGDH Defines a Metabolic Subtype in Lung Adenocarcinomas with Poor Prognosis. Cell Rep *19*, 2289–2303.

Zhang, N., and Bevan, M.J. (2011). CD8(+) T cells: foot soldiers of the immune system. Immunity *35*, 161–168.

10. APPENDIX

Inventory of the appendix:

Appendix A1. Additional Western blots.

Appendix A2. Additional heatmaps based on the RNAseq experiment from Figure 3.

Appendix A3. Additional data on Jurkat T cells.

Appendix A4. Additional data from the public domain.

Appendix A5. CRISPR-Cas9 induced gene-editing in human T_{NV} cells.

Appendix A1. Additional Western blots.

A PHGDH-inhibitor treatment in presence of extracellular serine

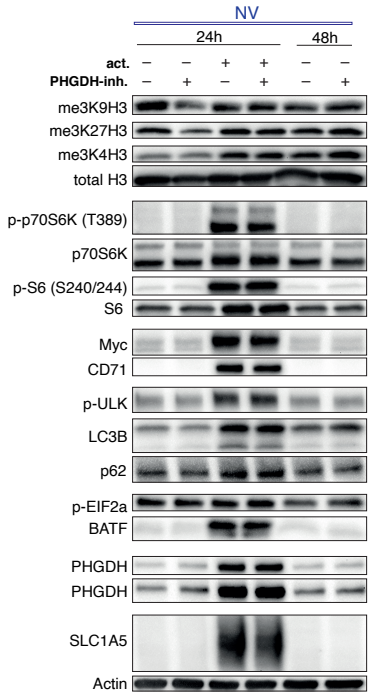

B Timcourse experiment with human CD4⁺ T cell subsets

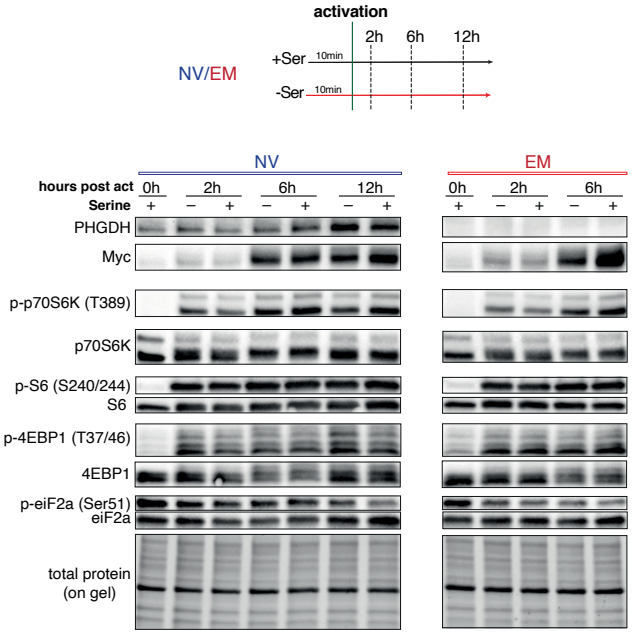

C Actue starvation experimet - a timecourse

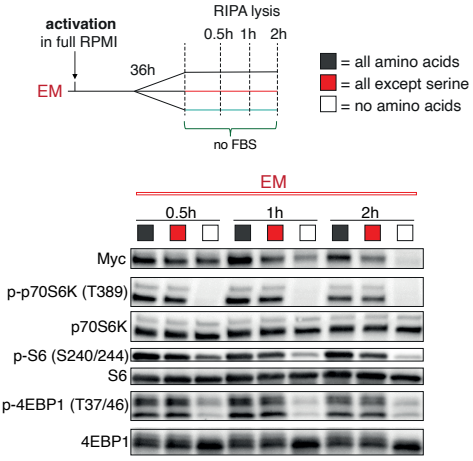

D mTORC1 amino acid sensing

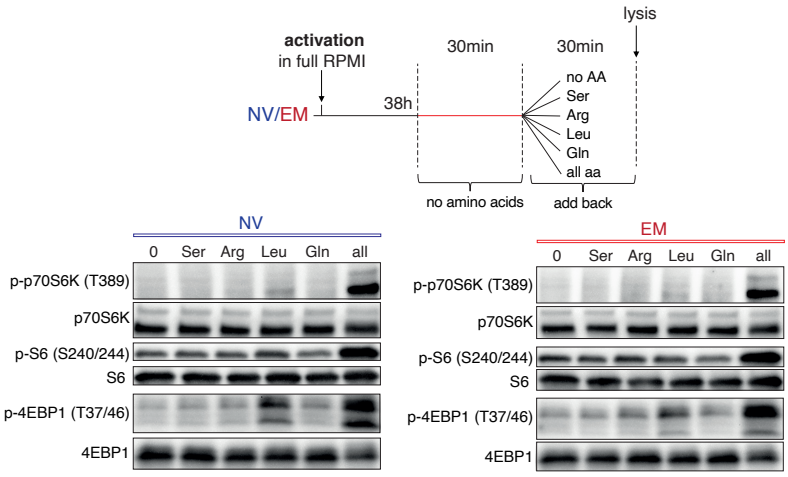

E Intracellular localisation of PHGDH in T_{NV} cells

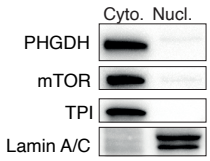

Appendix A1. Additional Western blots.

(**A**) Western blot probed for indicated proteins and phosphoproteins. Human CD8+ T_{NV} cells were left unstimulated or were activated for indicated timepoints in presence or absence of PHGDH-inhibitor (5µM) in serine replete media. The absence of any effect on the assessed proteins or phosphoproteins argues in favor of the idea that T_{NV} cells do not depend on or engage in serine *de novo* synthesis, as long as extracellular serine is present.

(**B**) Western blot for PHGDH, Myc and downstream targets of mTORC1. Human CD4+ T cell subsets were cultured for 10min in presence or absence of extracellular serine followed by anti-CD3/CD28 activation. At indicated timepoints, cells were harvested and processed for Western blotting. Due limited cell numbers, the 12h timepoint is lacking for T_{EM} cells.

(**C**) Western blot for Myc and downstream targets of mTORC1. Human CD8+ T_{EM} cells at 36h post-activation were starved of serine or all AA for indicated timepoints. Based on these findings, the 1h timepoint was chosen for further acute starvation experiments (Figure S3I).

(**D**) Western blot probed for downstream targets of mTORC1, the prototypic AA sensor. Sorted human CD8+ T cell subsets at 36h post-activation were starved for 30min of all AA, followed by a 30min incubation with indicated individual AA or all AA. In this experiment, mainly Leucine (Leu) was found to induced mTORC1 activity on its own (especially visible for p-4EBP1).

(**E**) Sorted human CD8+ T_{NV} cells were activated for 36h and fractionated into cytoplasmic (Cyto.) and nuclear (Nucl.) components. Fractions were then analyzed by Western blotting, which revealed a cytoplasmic localization of PHGDH. mTOR and TPI (Triose-phosphate isomerase) were used as cytoplasmic markers, while Lamin A/C served as a nuclear marker.

Appendix A2. Additional heatmaps based on the RNAseq experiment of Figure 3.

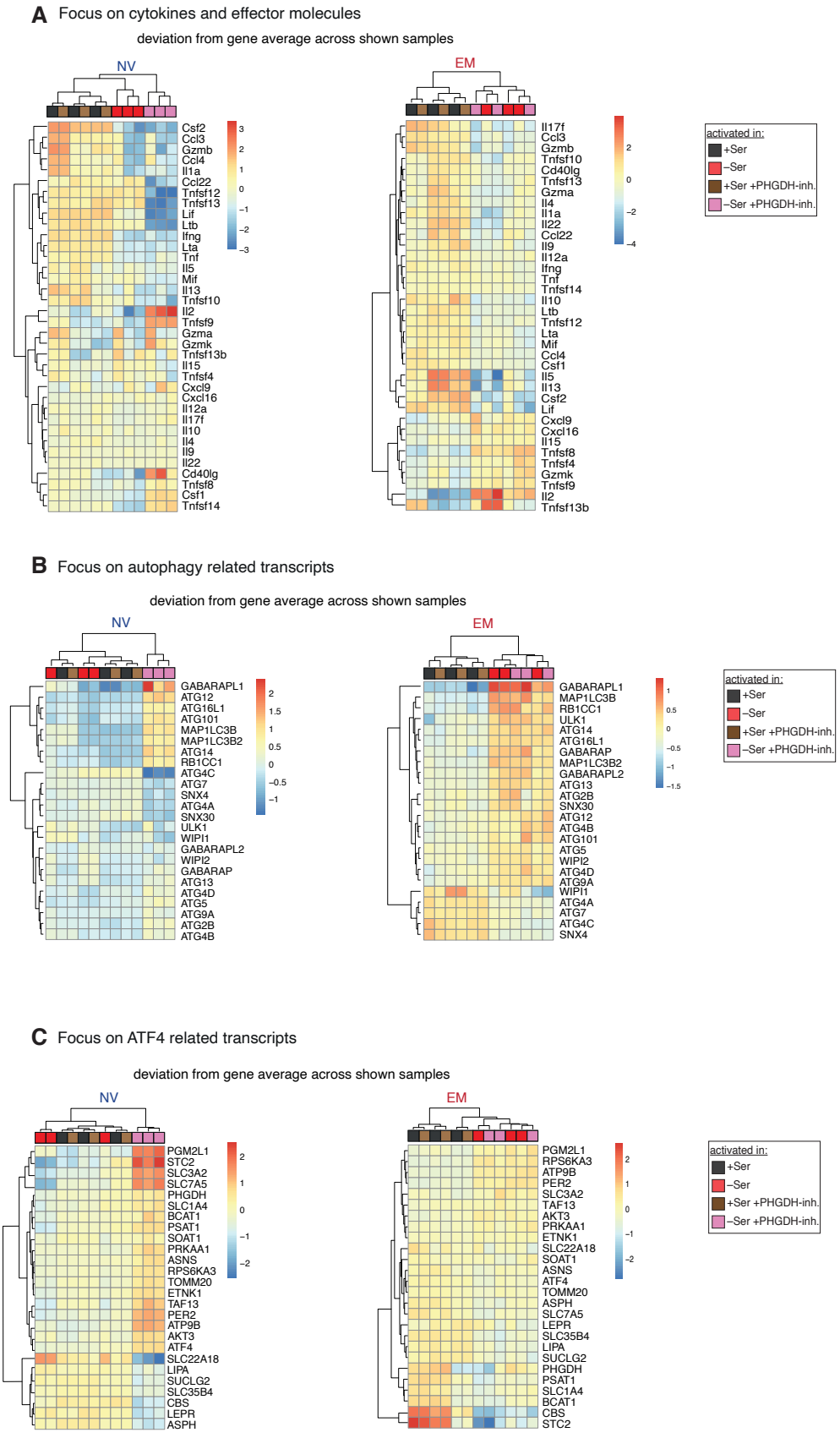

Appendix A2. Additional heatmaps based on the RNAseq experiment from Figure 3.

These heatmaps were generated based on the RNAseq experiment of $CD8^+$ T_{NV} and T_{EM} cells activated under conditions illustrated in the box on the right side. Shown are gene lists containing transcripts of cytokines and effector molecules (**A**), transcripts related to autophagy (**B**) and transcripts know to be targets of ATF4 (**C**). The color in the heatmap indicates the deviation from gene average across shown samples. The genes lists are based on corresponding GO terms, which are online available at: http://www.informatics.jax.org/go/term

Appendix A3. Additional data on Jurkat T cells.

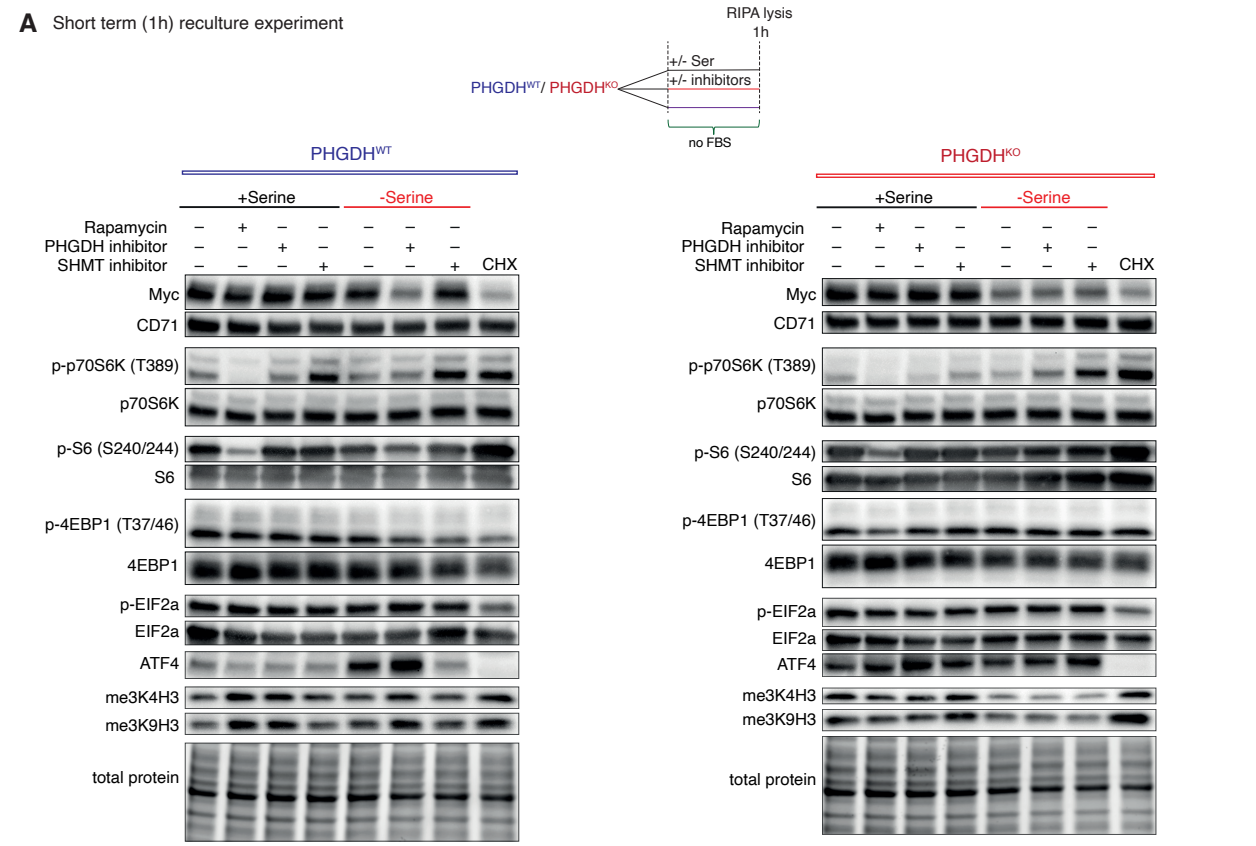

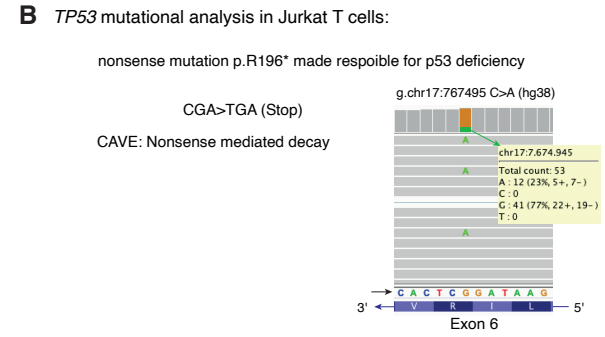

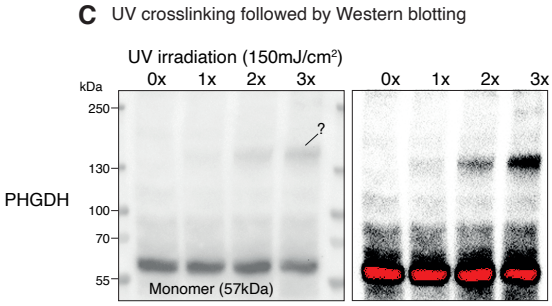

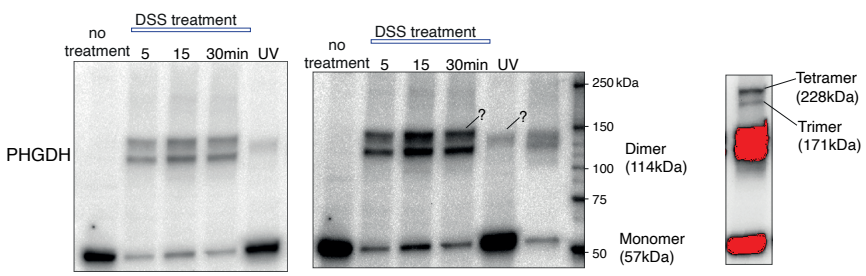

Appendix A3. Additional data on Jurkat T cells.

E Investigating the oligomerisation state of PHGDH variants with different crosslinking techniques

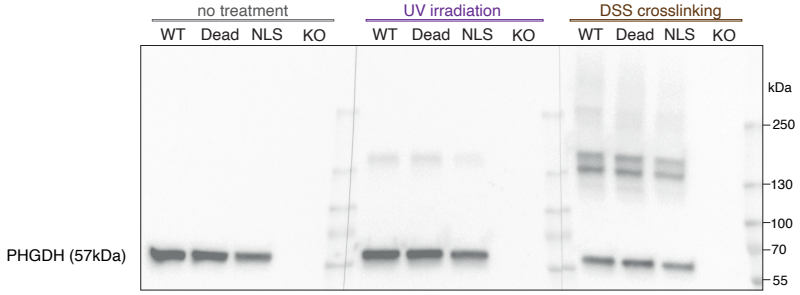

F Experimental setup: RNAseq after PHGDH-KO in Jurkat T cells

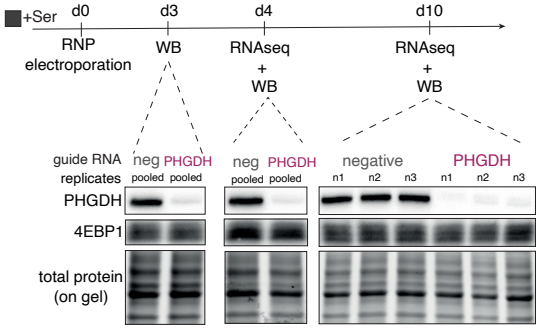

G Day 4 post-electroporation readout

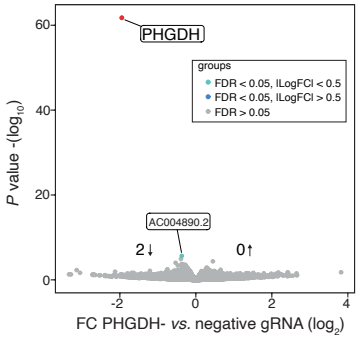

H Day 10 post-electroporation readout

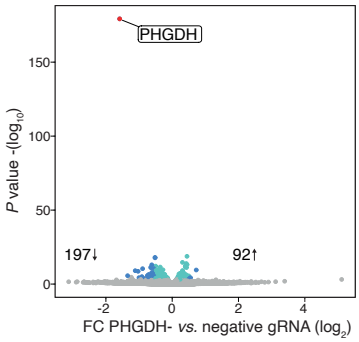

I Bulk Jurkat cells: Poliferation assay upon PHGDH-KO

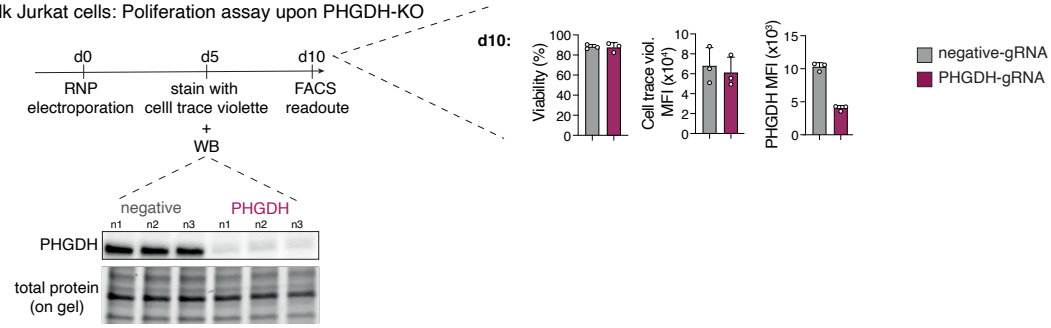

Appendix A3. Additional data on Jurkat T cells.

(**A**) Related to Figure S3N (same lysates). Western blot for indicated proteins and phosphoproteins of $PHGDH^{WT}$ and $PHGDH^{KO}$ Jurkat T cells after 1h culture under indicated conditions. PHGDH inhibitor (5µM), SHMT1/2 inhibitor (1.25µM), Rapamycin (20ng/ml), Cycloheximide (CHX, 50µM).

(**B**) Related to Figure S3M. Mutational analysis of *TP53* in Jurkat T cells based on RNAseq data. The print screen form the IGV browser shows the nonsense mutation, which is thought to be responsible for PHGDH deficiency of Jurkat T cells (Gioia et al., 2018). While nonsense mediated mRNA decay could be responsible, we only found a low frequency of this mutation and suggest that the mutation described in Figure S3M is responsible for p53 deficiency of Jurkat T cells.

(**C**) Bulk Jurkat T cells were irradiated for indicated times with ultra violet (UV) light (150mJ/cm^2) on ice with a Stratalinker 2000. Cells were then harvested, lysed and analyzed by Western blotting. UV-irradiation induced a higher running form of PHGDH at around 140kDa, which might be due to UV-induced formation of covalent bonds between PHGDH and target RNA, PHGDH-monomers or PHGDH and other proteins. On the right side, an overexposed image of the same blot is shown

(**D**) Jurkat T cells were treated with DSS (disuccinimidyl suberate, 2mM, #2655, Thermo) or UV (2x150mJ/cm^2) while viable, then harvested and processed for Western blotting. While DSS is thought to crosslink proteins to other proteins, UV is thought to crosslink proteins to RNA, if interaction partners are close enough. These two crosslinking techniques induced different higher running bands of PHGDH. While we assume that one of them is the PHGDH dimer, theoretically running at around 114kDa, we do not know the composition of the other bands.

(**E**) $PHGDH^{KO}$ Jurkat T cells re-expressing indicated PHGDH variants were crosslinked with DSS or UV as described in Appendix A3D. Since the R163Q mutation of $PHGDH^{NLS}$ is located at the dimer interface, we hypothesized, that it might impaired dimerization of PHGDH. However, we did not find a major impact on the higher running bands induced by DSS or UV crosslinking (one of them likely being the dimer).

(**F**) Schematic of the experimental design of PHGDH gene-editing in bulk Jurkat T cells followed by RNAseq. Ribonucleoproteins (RNPs) containing negative-guide RNA (gRNA) or PHGDH-gRNA were delivered by electroporation. After CRISPR-Cas9 induced gene-editing, several days were required for PHGDH protein levels to decrease. This depends on the expression level, which is high in Jurkat T cells, and on the half-life of the PHGDH protein. At day 3 post-electroporation, PHGDH was found to be depleted and at day 4 and day 10 RNAseq was performed (n=3).

(**G**) Volcano plot representation of differentially expressed genes (DEGs) at day 4 post-electroporation. Beside PHGDH, only one additional transcript was found to be differentially expressed at this timepoint.

(**H**) Volcano plot representation of DEGs at day 10 post-electroporation. At this timepoint, an upregulation of ATF4 target genes was observed, indicating that at one point during culture, these cells were starved of serine. Therefore, we were not able to dissect effects induced by of loss of PHGDH RNA-binding function from effects induced by of loss PHGDH catalytic activity.

(**I**) Schematic of the experimental design of the proliferation assay on bulk Jurkat T cells electroporated with Cas9 loaded negative-gRNA or PHGDH-gRNA at day 0. At day 5 post-electroporation, Western blotting confirmed successful gene-editing and cells were stained with the proliferation dye cell trace violet. At day 10 post-electroporation, viability and proliferation was assessed by flow cytometry, which revealed no impact of PHGDH depletion on these readouts.

Appendix A4. Additional data from the public domain.

A Protein-protein interaction network of murine PHGDH

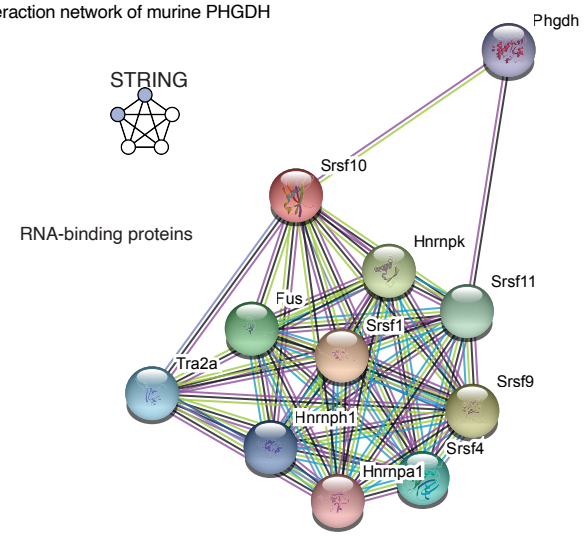

B Detection of GAPDH and PHGDH in published RNA interactome capture studies

GAPDH	PHGDH	Autor	cells	organism	technique	# of RBPs	year	Journal
no	no	Baltz et al	HEK293	Homo sapiens	polyA Interactome Capture	797	2012	Molecular cell
no	no	Castello et al	HeLa	Homo sapiens	polyA Interactome Capture	860	2012	Cell
no	no	Kwon et al	mESC	Mus musculus	polyA Interactome Capture	555	2013	Nature Structural & Molecular Biology
no	no	Kramer et al	HeLa	Homo sapiens	polyA Interactome Capture	35	2014	Nature methods
no	no	Beckmann et al	HuH7	Homo sapiens	polyA Interactome Capture	729	2015	Nature communications
no	no	Boucas et al	MEF	Mus musculus	polyA Interactome Capture	335	2015	PLOS one
no	no	Conrad et al	K562	Homo sapiens	polyA Interactome Capture from chromatin	279	2016	Nature communications
no	no				polyA Interactome Capture from nuclei	343		
no	no	He et al	mESC	Mus musculus	total RNA from nuclei labeld with 4-SU	803	2016	Molecular cell
no	no	Liepelt et al	RAW264.7	Mus musculus	polyA Interactome Capture	762	2016	Molecular and cellular proteomics
no	yes	Castello et al	HeLa	Homo sapiens	polyA RBDmap	529	2016	Molecular cell
yes	no	Liao et al	HL-1	Mus musculus	polyA Interactome Capture	963	2016	Cell reports
no	yes				polyA RBDmap	368		
yes	yes	Bao et al	HeLa	Homo sapiens	RNA interactome using click chemistry (RICK)	720	2018	Nature methods
no	no				polyA Interactome Capture	554		
yes	yes		mESC		RNA interactome using click chemistry (RICK)	518		
yes	yes	Huang et al	HeLa	Homo sapiens	click chemistry-assisted RNA-interactome capture (CARIC)	?	2018	J. Vis.Exp (Jove)
yes	yes	Trendel et al	MCF7	Homo sapiens	protein-crosslinked RNA extraction with TRIZOL (XRNAX)	858 in common	2019	Cell (resource)
			HeLa					
			HEK293					
yes	yes	Urdaneta et al	HEK293	Homo sapiens	phenol-toluol extraction (PTEX)	3037	2019	Nature communications
yes	yes	Rayner et al	HEK293	Homo sapiens	orthogonal organic phase separation (OOPS) with TRIZOL	759 in common	2019	Nature Biotechology
			MCF10A					
			U2OS					

C PHGDH in pubmed: number of publications per year

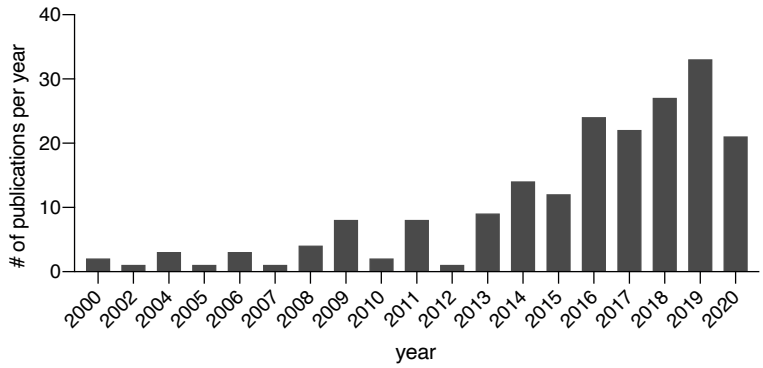

Appendix A4. Additional data from the public domain.

(**A**) Protein-protein interaction network of murine PHGDH based on the STRING database. Also murine PHGDH was experimentally found to interact with RNA-binding proteins. SRSF10/11, Serine And Arginine Rich Splicing Factor 10/11.

(**B**) Summary table of published RNA-interactome capture studies sorted chronologically, highlighting first author of the publication, cells and technique used, number of RNA-binding proteins detected (RBPs) and journal of the publication. On the left side, yes or no indicates whether GAPDH or PHGDH were found binding RNA in these studies. Please note, that PHGDH was found in more screens than GAPDH, which has a well described RNA-binding activity. Furthermore it is interesting to note, that newer techniques, which are not based on poly-A enrichment, found PHGDH with higher frequency to interact with RNA.

(**C**) Bar graph showing the number of publications per year containing the word 'PHGDH' according to Pubmed. Please note the rising interest in this enzyme, which is mainly driven by the cancer-field.

Appendix A5. CRISPR-Cas9 induced gene editing in human T_{NV} cells.

A IGV printscreen illustrating Indel formation by non-homologous end joining

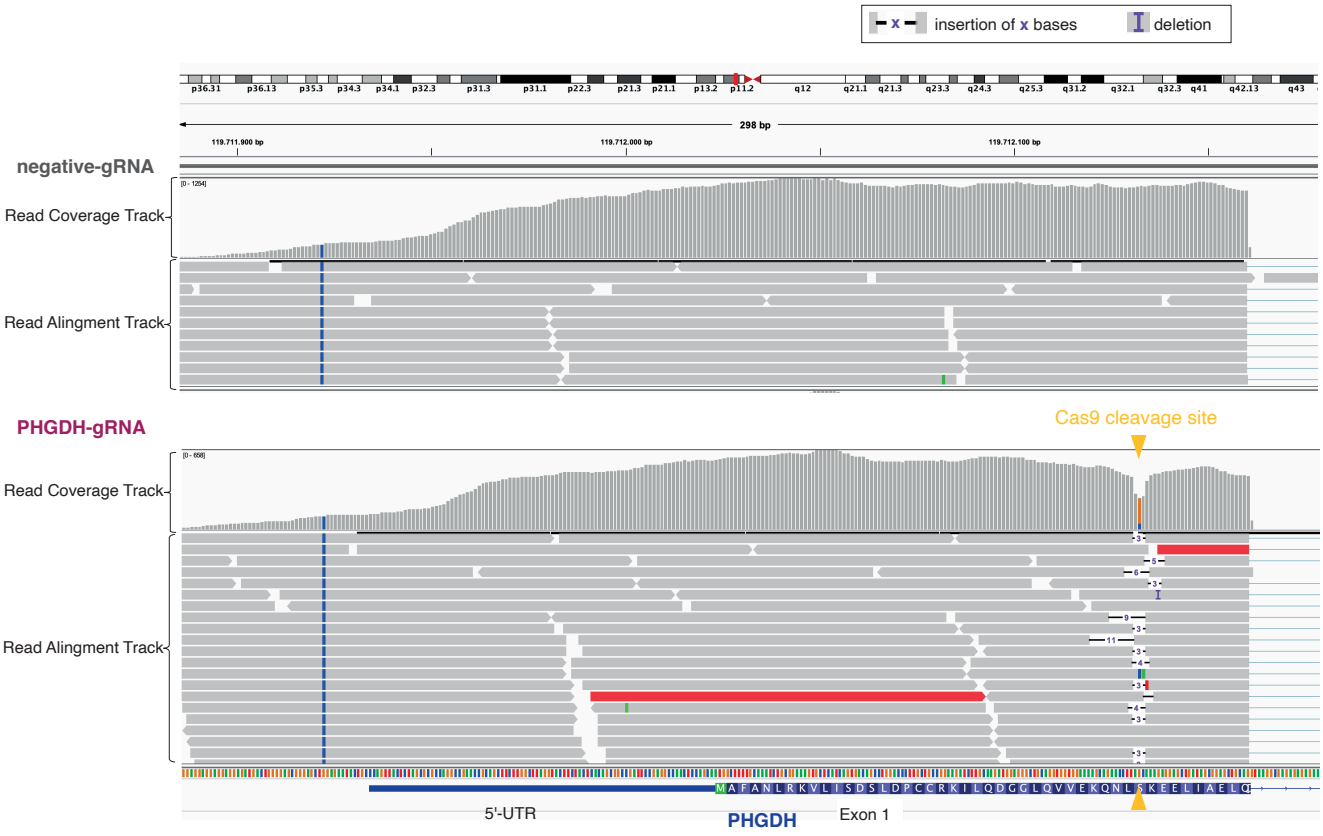

B Proliferation assay: negative- *vs.* PHGDH-gRNA treated primary effector T cells

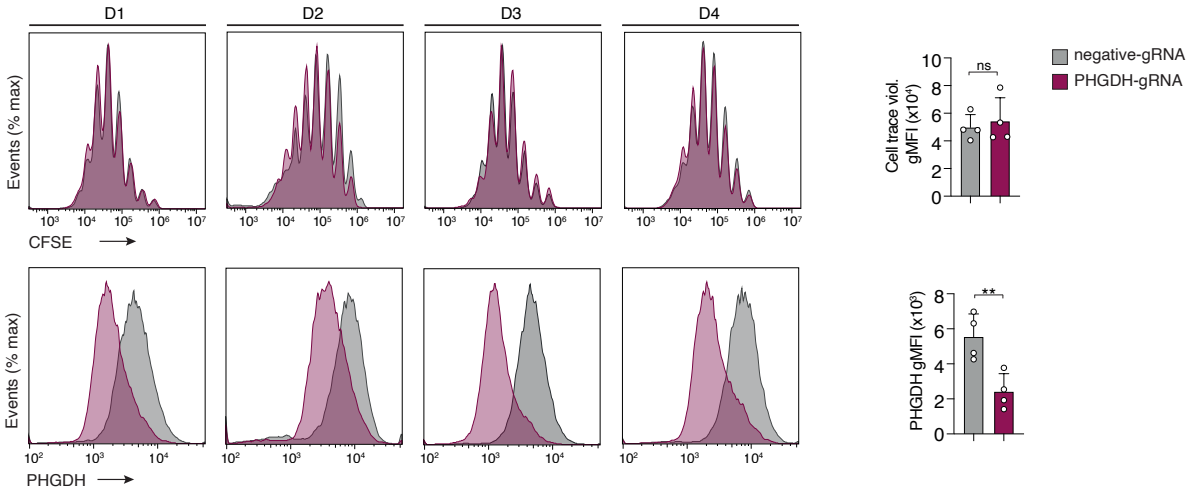

Appendix A5. CRISPR-Cas9 induced gene-editing in human T_{NV} cells.

(**A**) Related to Figure 6. This print screen from the IGV browser is showing the alignment of individual reads to the reference genome at the start of the *PHGDH* gene. These reads represent the raw data obtain by the RNAseq experiment of negative-gRNA (top) or PHGDH-gRNA (bottom) treated T_{NV} cells from one human donor at the 72h post-activation timepoint. The PHGDH-gRNA guides Cas9 to the end of exon 1, where the cutting site is highlighted by yellow arrows. DNA double-strand breaks were repaired by non-homologous end joining, which is reflected by the fact that reads contain different amounts of insertions and deletions (indels) of nucleobases. This highlights the randomness of the repair process and shows, that mRNA is still present after gene-editing, albeit often, but not always, leading to a frameshift and subsequently nonsense-mediate RNA decay.

(**B**) CFSE-based cell proliferation assay in presence of extracellular serine. After electroporation of negative- or PHGDH-gRNA loaded Cas9 and a resting period of 24h, T_{NV} cells were stained with the cell proliferation dye CFSE and activated by anti-CD3/CD28 activation. At 5 days post-electroporation, proliferation and PHGDH expression were assessed by flow cytometry, which revealed that PHGDH depletion had no impact on primary effector T cell expansion (n=4). Data are represented as mean ± SD. Statistical significance was assessed by two-sided paired Student's *t*-test. $^{**}P < 0.01$; ns, not significant.